

https://dspace.org/

Magnetic enhancement of a high entropy spinel oxide electrocatalyst for rechargeable zinc-air batteries

Hechter, Ernst Heznz

2024

University of the Witwatersrand, Johannesburg

https://hdl.handle.net/10539/42142

Hechter, Ernst Heznz . (2024). Magnetic enhancement of a high entropy spinel oxide electrocatalyst for rechargeable zinc-air batteries [Master's dissertation, University of the Witwatersrand, Johannesburg]. WIReDSpace.

Downloaded from a DSpace repository. https://dspace.org/



UNIVERSITY OF THE
WITWATERSRAND,
JOHANNESBURG

Magnetic enhancement of a high entropy spinel oxide electrocatalyst for rechargeable zinc-air batteries

Ernst Heznz Hechter

Dissertation

submitted to the Faculty of Science, University of the Witwatersrand, Johannesburg, in fulfilment of the requirements for the degree of Master of Science (Chemistry)

Supervised by

Dr Dean Barrett

Professor Kenneth Ozoemena

Dr Aderemi Haruna

June 2024

Declaration

I declare that this Research Report is my own work. It is being submitted for the Degree of Master of Science (Chemistry) at the University of the Witwatersrand, Johannesburg. It has not been submitted before for any degree or examination at any other Institution.

Signed: Ernst Heznz Hechter



On this 6th day of June in the year 2024

Abstract

The exploration of high entropy materials (HEMs) as electrocatalyst materials has only recently begun to accelerate. Similarly, the effect of magnetic fields on the oxygen evolution and reduction reactions has recently begun to attract great interest. In this work nanoparticles of the high entropy oxide $(CuCoFeMnNi)_3O_4$ were synthesized and supported on Vulcan carbon for use as a bifunctional OER/ORR catalyst in a rechargeable zinc-air battery (RZAB). The products were characterized to confirm and investigate the solid solution high entropy phase, and the electrochemistry was investigated with and without an external magnetic field. The HEMs demonstrated moderate intrinsic electrochemical properties, with overpotentials and current densities comparable to commercial platinum on carbon catalysts even at low loadings. Here is reported the most significant magnetic enhancement in RZAB power profile in literature at the time of writing, as well as improved RZAB stability and areal energy. This work offers insight into the mechanism of magnetic enhancement in the case of high entropy materials, and pioneers the use of combined strategies to achieve stable, cost-efficient and effective bifunctional OER/ORR electrocatalysis.

Dedicated to my mother,

to my friends,

to Leonie,

and our dreams for this world.

Acknowledgement

I extend my heartfelt gratitude to my supervisors, Professor Kenneth Ozoemena, Dr Dean Barrett and Dr Aderemi Haruna for their unwavering guidance, invaluable insights, and continuous encouragement throughout the course of my research. Their expertise and commitment have been instrumental in shaping this project.

I would also like to express my appreciation to the members of the CATMAT and MEET research groups. The collaborative environment fostered by these remarkable groups has provided diverse perspectives, expertise, and a supportive community that has enhanced the quality of my work.

A special thanks goes to Wits University and the National Research Foundation for their financial support, which has been crucial in facilitating this research project (SRUG2204041774). Their investment in academic pursuits plays a pivotal role in advancing scientific knowledge and fostering innovation.

I am indebted to the teams at Wuhan University of Technology, European Synchrotron Radiation Facility, Canadian Light Source, Council for Scientific and Industrial Research, University of South Africa, and Cornell University for their collaboration and assistance in conducting technically and materially demanding experiments. The access to their facilities and expertise has been invaluable in gathering essential data for this study.

Additionally, I extend my gratitude to Maxwell Terban at Max Planck Institute for his expertise in the analysis and refinement of diffraction and total scattering PDF data. High entropy materials cannot be elucidated without help from such a master of the art.

This journey would not have been possible without the support and encouragement from my family and friends. You listened to my ramblings, provided insights that made me think you're

all secretly electrochemists, and helped me to keep going when the research seemed not to be going anywhere.

In conclusion, I am grateful to everyone who has played a role in making this research a reality. Your support has been indispensable, and I am truly thankful for the collaborative spirit that has defined my MSc.

Contents

Declaration 2
Abstract 3
Acknowledgement 5
List of Figures 9
List of Tables 10
List of Terms and Symbols 11
Research Output and Conferences 12
Chapter 1: Introduction 13
1.1 Problem, Hypothesis and Aim 13
1.2 Background and Justification 13
Chapter 2: Literature Review 22
2.1 History 22
2.2 The Current Situation 24
2.2.1 The Limits of Lithium 24
2.2.2 Climate Concerns 25
2.2.3 Renewable Renaissance 26
2.2.4 Zinc for Net Zero? 27
2.3 Anode 28
2.4 Electrolyte 29
2.5 Cathode 30
2.5.1 The Hidden Spintronics 30
2.5.2 Lorentz Force Transport 32
2.5.3 Magnetophoretic Transport 33
2.5.4 Electron transfer in a Field 34
2.5.5 Practical Advances in the Field 35
2.6 Material design 38
2.6.1 Bifunctionality 38
2.6.2 High Entropy Materials 39
2.6.3 High Entropy Spinels 41
2.6.4 Bifunctional OER/ORR HEM Catalysts 43
2.6.5 $(CuCoFeMnNi)_3O_4$ 44
Chapter 3: Materials and Methods 45
3.1 Reagents 45

3.2 Syntheses 45
3.3 Characterisation 47
3.3.1 Powder X-Ray Diffraction (PXRD) 47
3.3.2 Total Scattering – Pair Distribution Function (PDF) analysis 48
3.3.2 Raman 50
3.3.3 Microscopy 51
3.3.4 X-ray Photoelectron Spectroscopy (XPS) 52
3.3.5 Electron Paramagnetic Resonance (EPR) 53
3.3.6 Ultraviolet and Visible light Spectroscopy (UV-VIS) 54
3.3.7 Ultraviolet Photoelectron Spectroscopy (UPS) 55
3.3.8 Thermogravimetry 56
3.3.9 Surface nitrogen adsorption/desorption 56
3.4 Electrochemistry 56
3.4.1 Cathode testing 56
3.4.2 RZAB testing 61
Chapter 4: Results and Discussion 63
4.1 Powder X-Ray Diffraction (PXRD) 63
4.2 Pair Diffraction Function (PDF) 65
..... 67
4.3 Raman Spectroscopy 67
4.4 Microscopy 70
4.5 X-ray Photoelectron Spectroscopy (XPS) 73
4.6 Electron paramagnetic resonance (EPR) 76
4.7 Ultraviolet Photoelectron Spectroscopy (UPS) and UV-VIS Spectroscopy 78
4.8 Thermogravimetric Analysis 80
4.9 Surface Area and Pore Analysis 81
4.10 Three Electrode Electrochemistry 83
4.11 Two-electrode tests on a zinc-air test cell 90
Chapter 5: Conclusion 97
5.2 Recommendations 98
References 100
Appendix 109
A1 Rietveld Refinement parameters 109
A2 Simulated Crystal planes and D-spacings for HESO 111
A3 Table of A_{1g} Raman signals in partially inverted spinels 114

List of Figures

Figure 1: Diagram of a RZAB discharging, with permission from Haruna & Ozoemena, 2020[9] 15
Figure 2: Representation of the high entropy spinel oxide $(CuCoFeMnNi)_3O_4$ 17
Figure 3: Visual summary of the electron spin effect of magnetic enhancement 20
Figure 4: The molecular orbital (MO) diagrams of species involved in the ORR/OER reactions. 30
Figure 5: Synthesis schemes of HESO and HESO/C 46
Figure 6: High resolution PXRD of the HESO and composites 63
Figure 7: Rietveld Refinement of HESO 64
Figure 8: HESO PDF data with cubic and triclinic refinements. 65
Figure 9: PDF of the metal-oxygen and metal-metal bond distances 65
Figure 10: Comparison of PDF refinements of HESO using various crystal systems 67
Figure 11: A1g vibration of an MO4 unit 68
Figure 12: a) Raman Spectra of lattice vibrations. b) Full Raman spectra of 10 and 20 % HESO/C 69
Figure 13: SEM micrographs of (a1) 20% HESO/C and (a2) Pristine HESO. (b) EDS elemental maps of each of the five metals. TEM micrographs of (c1) pristine HESO and (c2, c3) 20% HESO/C 70
Figure 14: TEM micrographs (a1) Pristine $(CuCoFeMnNi)_3O_4$ (a2) lattice fringes of the pristine HESO (a3) d spacings determined for the (111) plane (a4) d spacings determined for 202 plane (a5) Visualisation of the visible lattice planes. (a6) Micrograph of a particle at a different angle. (a7) FFT and (a8) d-spacing determined. (a9) 311 lattice plane (b1) 20% HESO/C (b2) lattice fringes of composite (b3) d spacings determined for 202 plane in composite (b4) visualistion of the HESO (202) plane 71
Figure 15: O1s XPS spectra of a) pristine HESO and b) 20% HESO/C 74
Figure 16: Deconvoluted XPS spectra 75
Figure 17: EPR spectra of the HESO and composites 76
Figure 18: Normalised EPR Spectra of the HESO and composites 77
Figure 19: UPS spectra of HESO and composites 78
Figure 20: UV-VIS and Tauc plots of the HESO and composites 79
Figure 21: TGA of 10 and 20% HESO/C under a) nitrogen and b) air 80
Figure 22: Pore size distribution (a) and BET adsorption-desorption curves (b) for Vulcan carbon, pristine HESO and 20% HESO/C composite 81
Figure 23: Cyclic voltammetry of (a) pristine HESO, (b) 10% HESO/C, and (c) 20% HESO/C. Only the 5^{th} cycles are shown. (d) ORR and (e) OER polarisation curve for the intrinsic catalyst at various loadings,

at 1600 RPM in 1 M KOH. (f) ORR and (g) OER polarisation curves for the 20% HESO/C in 1 M KOH at 1600 RPM, with and without an applied field. (h) ORR polarisation curves for the 20% HESO/C in 0.1 M KOH at 1600 RPM, with and without an external field applied. (i) Koutêcky-Levich plots for the 20% HESO/C compared to theoretical electron numbers. CV of 20% HESO/C with and without the field, under nitrogen (j) and oxygen (k) atmospheres. 84
Figure 24: Tafel plots for 20% HESO/C with and without an applied field under a) ORR and b) OER conditions. EIS for 20% HESO/C at c) 0.85 V and d) 1.6 V 88
Figure 25: a) The assembled zinc-air battery. b) Power profiles of the standard 20% Pt/C + IrO2 cathode and the 20% HESO/C cathode, with and without an applied field 90
Figure 27: Rate capability tests for RZABs with (a) and without (b) a magnetic field 94
Figure 28: (a) deep discharge profiles of the standard and 20% HESO/C, 2 mA.cm^{-2} and 36 h cycles (b) Shallow discharge profiles of the standards and HESO/C 0.5 mA.cm^{-2} and 1 h cycles(c) ΔE of the 20% HESO/C around 50 hours (d) ΔE of the 20% HESO/C around 200 hours of operation (e) EIS at the OCV of the HESO/C RZAB with and without a magnetic field (f) End of life EIS at the OCV of the HESO/C RZAB before and after deep discharge cycling for 150 hours 96

List of Tables

Table 1: Summary of research in oxygen catalysis with magnetic fields 37
Table 2: A selection of recent publications on HEM bifunctional OER/ORR catalysts 43
Table 3: UPS parameters for HESO and composites 78
Table 4: BET derived values. 82
Table 5: Comparison of ORR and OER magnetic enhancement with previous studies 89
Table 6: Previous achievements in magnetic enhancement of RZABs 91
Table 7: EIS parameters of RZAB with 20% HESO/C cathode 93

List of Terms and Symbols

BET	Brunauer-Emmett-Teller, a model used for finding surface area and pore volume from N_2 adsorption experiments
EIS	Electronic Impedance Spectroscopy
EPR	Electron Paramagnetic Resonance, also called ESR (Electron Spin Resonance)
HEM	High Entropy Material, any solid with a conformational entropy >1.5R
HESO	High Entropy Spinel Oxide
OER	Oxygen evolution reaction
ORR	Oxygen reduction reaction
PDF	Pair Distribution Function, a total scattering technique to find relative frequency of interatomic spacings
RZAB	Rechargeable Zinc-Air Battery
SEM	Scanning Electron Microscopy
Spin-Orbit Coupling	The interaction between the angular momentum of an electron around a nucleus and the electron's own intrinsic angular momentum
TEM	Transmission Electron Microscopy
TGA	Thermo-gravimetric analysis
UPS	Ultra-violet Photoelectron Spectroscopy
UV-Vis	Ultra-violet and visible light spectroscopy
Vulcan carbon	Brand name for carbon black XC72
XPS	X-ray photoelectron Spectroscopy
XRD	X-ray Diffraction

Å	Ångstrom, a distance of 10^{-10} m
A	Ampere, measure of electric current
B or $\vec{B}$	Magnetic field
CP	Chronopotentiometry
CV	Cyclic Voltammetry
ECSA	Electrochemical Surface Area
eV	Electron-Volt, measure of energy equal to $1.6*10^{-19}$ J
LSV	Linear Sweep Voltammetry
T	Tesla, measure of magnetic field strength
V	Volt, measure of electrochemical potential
ΔE	Difference in potential between an oxidation and reduction process, in this document referring to the difference between OER and ORR potentials
ΔV	The difference between charge and discharge potentials of a RZAB
η	Overpotential
Ω	Ohm, measure of electric resistance

Research Output and Conferences

Oral Presentation at CATSA 2022

Flash Talk and Poster Presentation at ElectroChemSA 2023

Oral Presentation at CATSA 2023

Research paper submitted to Angewandte Chemie for publication

Chapter 1: Introduction

1.1 Problem, Hypothesis and Aim

Battery based energy storage requires extensive improvement in capacity, cost, and safety to meet the demands of the global renewable energy transition. Rechargeable Zinc-Air Batteries offer low cost, safe components, and high energy density, but are limited by the slow kinetics and high overpotentials of the oxygen reduction and evolution reactions at the cathode. By combining two recent approaches to electrocatalysis, namely high entropy spinel oxide ceramic nanoparticles and magnetic enhancement, a more efficient bifunctional catalysis approach could be demonstrated. The aim of this research is the synthesis and complete characterisation of $(CuCoFeMnNi)_{3/5}O_4$ high entropy spinel oxide (HESO), and the demonstration and investigation of the effect of a magnetic field on its catalytic activity. HESO synthesis by the Pechini method is untested, and full characterisation of this HESO is incomplete in the literature.

1.2 Background and Justification

Historically, the ever-increasing demand for energy has been met through the utilization of fossil fuels such as coal, oil, and natural gas. However, this pattern cannot continue indefinitely. While new fossil fuel reserves may yet be discovered, they are by their nature a limited resource, and supplies are likely to diminish, driving prices higher and ultimately restricting energy utilization.[1] Additionally, fossil fuels must generally be transported between their point of extraction and point of use.[2] These supply chains are fragile and prone to disruption, as has been seen in recent armed conflicts.[2]

Furthermore, fossil fuel use has been firmly linked to the degradation of the environment and human health. Emission of toxic particulate matter, volatile organic compounds, and NO_x and SO_x gasses from vehicles, power plants and factories pose a serious threat, leading to an

estimated 1.3 million yearly excess deaths worldwide[2,3]. Combined with the direct effect of emissions, climate change resulting from the greenhouse effect of carbon dioxide, methane and other waste emissions threatens rising sea levels and meteorological disturbances that will render many areas uninhabitable.[1] Faced with supply restrictions, loss of ecosystem services, public health crises and the looming threat of climate change, society has been forced to begin the transition towards sustainable energy sources.[2]

The alternative to fossil fuel reliance is the adoption of renewable and nuclear energy. Photovoltaic and concentrated solar, wind and fission energy technologies are already viable, and are being adopted by commercial and government projects worldwide. However, energy production alone is not sufficient: storage for intermittent power sources and for vehicles, and the conversion of industries with high energy demands such as steel manufacture, remain challenges[4].

The current leading energy storage technology is the lithium-ion battery, which is used particularly in mobile devices and electric vehicles. However, this technology is faced by several limitations, including the high cost and accessibility of lithium and the requirement for toxic and expensive non-aqueous electrolytes, as well as the same supply chain vulnerabilities that face fossil fuels.[5,6] These factors do not discredit the technology, but do slow adoption and limit grid-scale storage applications of lithium-ion batteries. Some researchers also believe that the technology is approaching a ceiling in terms of energy density.[6,7] A potentially cheaper, safer, more environmentally friendly and energy dense solution may be found in metal-air batteries, shown schematically in figure 1.[8]

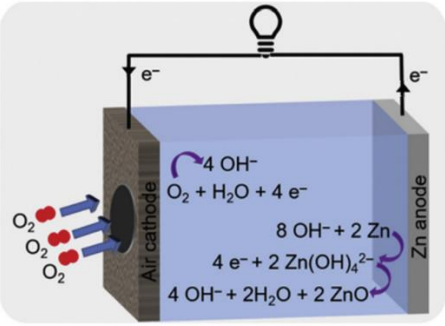


Figure 1: Diagram of a RZAB discharging, with permission from Haruna & Ozoemena, 2020[9]

These devices store energy in the potential between atmospheric oxygen and an elemental metal, such as aluminium, lithium, or, of specific interest in this study, zinc. A rechargeable zinc-air battery (RZAB) makes use of cheap and plentiful zinc metal, and has a safe, aqueous electrolyte. Since the oxygen is supplied by the atmosphere, there is no need for a bulky cathode compartment, giving a more compact battery.

During discharge, oxygen from the atmosphere is reduced (oxygen reduction reaction, ORR) at the air cathode to produce aqueous hydroxide ions, while zinc is oxidized at the anode to produce Zn^{2+} ions, forming first aqueous zinc hydroxide and then solid zincate. These half reactions are coupled through an external circuit, where the electrons may do useful work. During charging, a voltage is applied to reduce zinc ions back to zinc metal, while hydroxide is oxidized to produce water and release gaseous oxygen back into the atmosphere (oxygen evolution reaction, OER).[6,8,10] The appeal of zinc-air batteries is obvious: zinc is relatively plentiful, the aqueous alkaline electrolytes are benign, and the theoretical energy density of zinc-air batteries is up to five times greater than the lithium ion batteries, with costs per kWh of storage up to 40 times lower.[6,10] The overall process is shown in reactions 10-13.

There are two main barriers to the commercial use of zinc-air batteries: deterioration of the zinc anode, and sluggish ORR and OER kinetics at the cathode, requiring high overpotentials and noble metal catalysts to produce acceptable currents.[6,8,10] Cathode catalyst design is

challenging, as they must be bifunctional: highly active toward both ORR and OER, processes that generally have different catalyst requirements.[6,11]

The sluggish, four electron transfer of the oxygen evolution reaction (OER),[12–14] is shown in equations 1 through 4[15]. ORR proceeds through one of two possible pathways: A four electron transfer involving a single catalytic active site shown in equations 5 through 9[16], or more sluggish two two-electron transfers with production of peroxide as an intermediate. Currently, precious metal catalyst combinations such as ruthenium or iridium oxide and platinum-on-carbon are used to improve the rate of OER and ORR, but these catalysts are unstable and extremely expensive, hindering their use at scale. Development of economic, effective, and environmentally friendly catalysts is potentially the breakthrough needed in this area[17,18].

$* + OH^- \rightarrow *OH + e^-$ (1)

$*OH + OH^- \rightarrow *O + H_2O + e^-$ (2)

$*O + OH^- \rightarrow *OOH + e^-$ (3)

$*OOH + OH^- \rightarrow * + O_2 + H_2O + e^-$ (4)

$* + O_2 \rightarrow *O_2$ (5)

$*O_2 + H_2O + e^- \rightarrow *OOH + OH^-$ (6)

$*OOH + e^- \rightarrow *O + OH^-$ (7)

$*O + H_2O + e^- \rightarrow *OH + OH^-$ (8)

$*OH + e^- \rightarrow OH^- + *$ (9)

$Zn_{(s)} + 4\ OH^-_{(aq)} \leftrightarrow Zn(OH)_4^{2-}{}_{(aq)} + 2e^-$ -1.25 V (10)

$Zn(OH)_4^{2-}{}_{(aq)} \leftrightarrow ZnO_{(s)} + 2\ OH^-_{(aq)} + H_2O_{(l)}$ (11)

$O_{2(g)} + 2\ H_2O_{(l)} + 4\ e^- \leftrightarrow 4\ OH^-_{(aq)}$ 0.40 V (12)

Overall:

$2\ Zn + O_2 \leftrightarrow 2\ ZnO$ 1.65 V (13)

ORR/OER bifunctional catalysts for the air cathode should avoid expensive noble metals, be stable in oxygen and the alkaline electrolyte throughout the voltage range used and withstand at least hundreds of charge-discharge cycles. Most importantly, their catalytic activity should be comparable to or exceed the performance of the platinum group metal combination catalysts. These requirements are a challenge for traditional methods and materials.[6,7,9,11]

A class of materials that have only recently been investigated as electrocatalysts, but that may have the complex properties required for OER/ORR bifunctionality, are high entropy oxides (HEOs). An example of a HEO crystal can be seen in figure 2. The concept of high entropy materials was first introduced by Cantor et. al. and Ye et. al., as materials with five or more metals in equimolar proportions, giving them a configurational entropy greater than 1.5R[19,20]. Though the original work was on alloys, the concept has been expanded to include MOFs, sulphides, and oxides, among others. Four properties distinguish HEOs from conventional oxides of fewer metals.

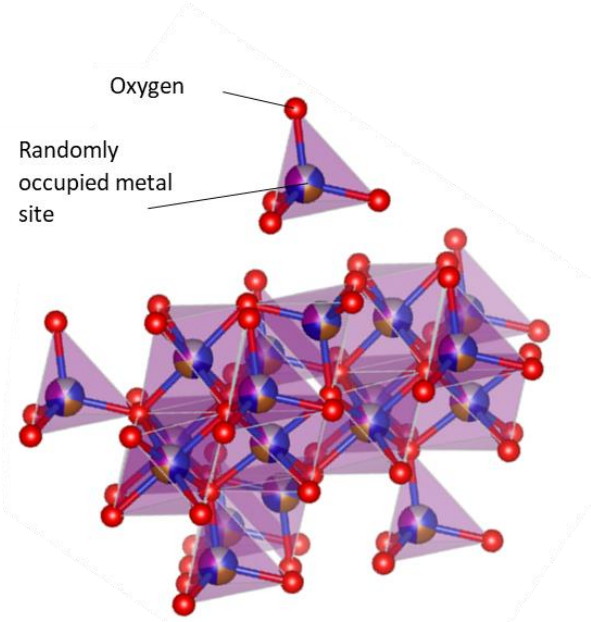


Figure 2: Representation of the high entropy spinel oxide $(CuCoFeMnNi)_3O_4$

The "high entropy effect" refers to the spontaneous formation of single-phase solid solutions at sufficiently high temperatures, due to the increased entropy in a solid solution. In these solid solutions, the cation positions of a crystal lattice, such as the spinel structure seen in this study, are randomly occupied by the metals. The "sluggish diffusion" effect is the extremely slow movement the ions in the HESO structure, as the randomly positioned metal ions create deep potential wells and steep energy barriers, effectively fixing the solid solution in a metastable state even at low temperatures and through a variety of conditions. The structure is maintained

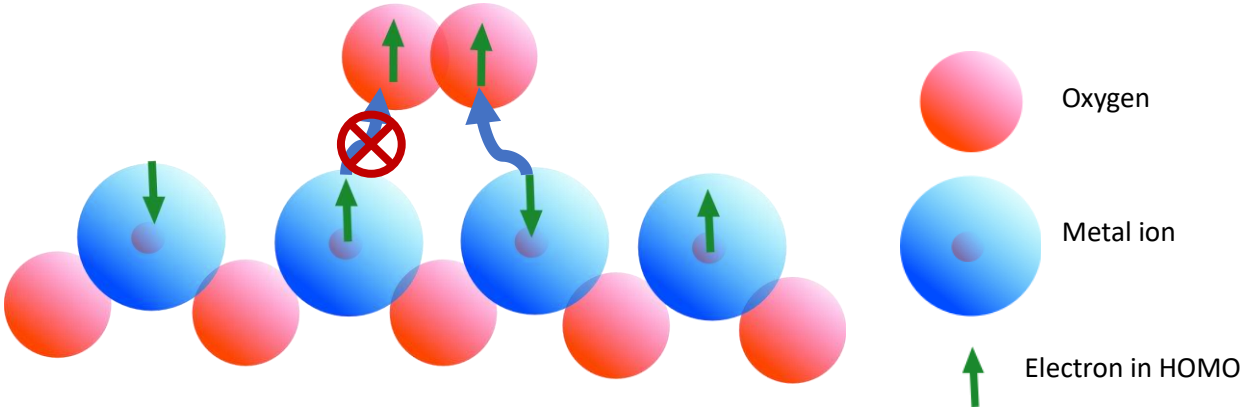
by this kinetic barrier even when degradation, such as segregation of the metal ions into different regions, is thermodynamically favoured. In a RZAB, the bifunctional catalyst must retain its structure over a range of voltages and thousands of charge/discharge cycles, and so the stability granted by the slow diffusion effect is desirable. The "Lattice Distortion" effect arises from differences in sizes and metal-oxygen bond lengths between the ions, causing a great deal of strain, distortion and defects in the crystal structure. Strain and distortion modifies the electronic band structure of the HESO compared to similar, lower strain analogues, while defects such as oxygen vacancies provide additional active sites for electrocatalysis. Finally, the "Cocktail" effect is the synergistic effects of many metals in close proximity to one another, giving rise to unique active sites.[13,21–24] For example, copper binds ORR reactants strongly, increasing the rate of reactant adsorption, while iron binds the products weakly, increasing the rate of product desorption. Cobalt and nickel, with intermediate binding energies, could provide pathways across the surface for adsorbed intermediates to move from strong to weak binding regions. This cocktail effect can be seen in other classes of materials, such as multiple metal single atom catalysts.[25]

Another exotic area of research that has been seeing attention in electrocatalysis in recent years is the application of external magnetic fields to enhance the activity of a catalyst. Magnetic fields have several interesting effects on electrochemical systems. The simplest are the mass transport effects of the Lorentz and Kelvin forces. The Lorentz force arises from the interaction between a moving charge and an external magnetic field, with the force acting perpendicular to the direction of motion and applied field.[26] This deflection leads to convection currents especially in areas where charged species typically have a preferred direction, such as near an electrode surface.[27] Such convection currents improve mass transport and also ensure even dissolution and deposition, preventing dendrite formation on metal electrodes.[26,28] The Kelvin force drives paramagnetic particles towards areas of higher magnetic field gradient, and

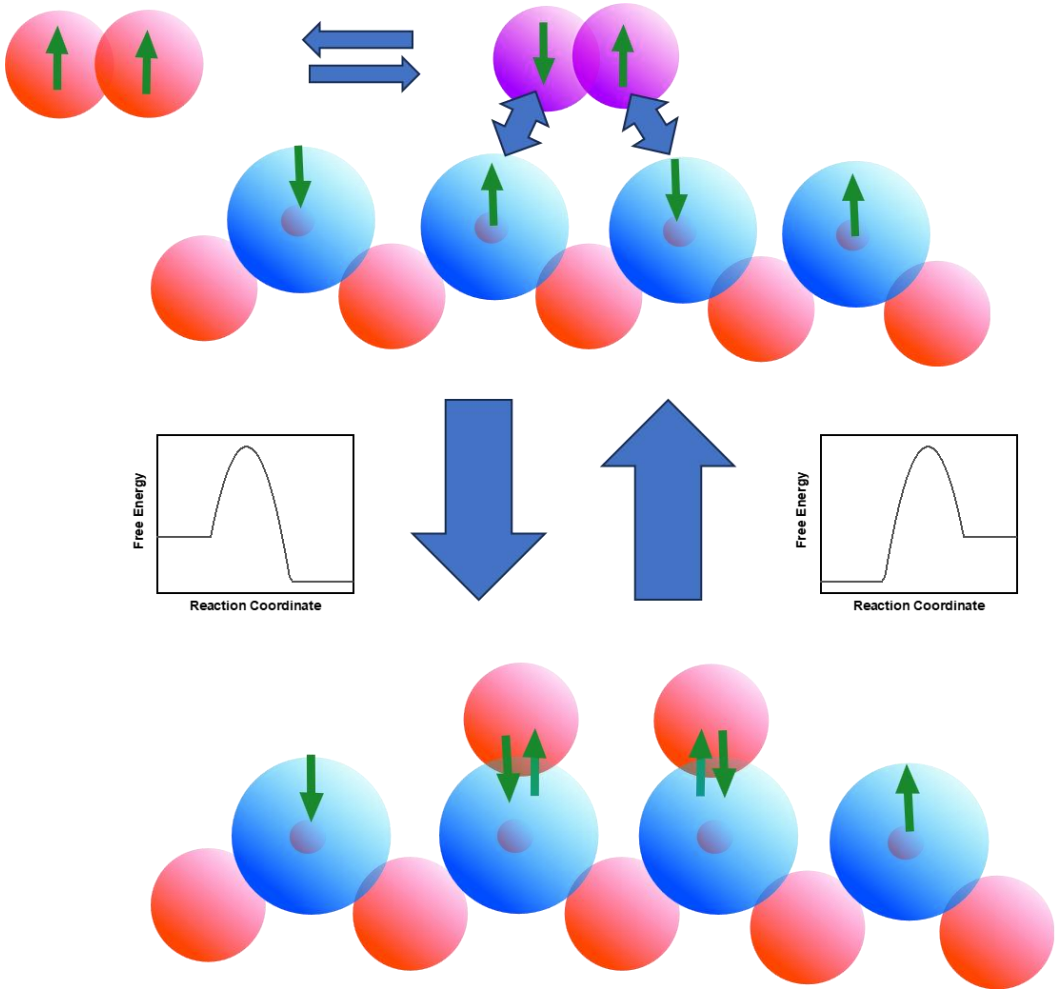
diamagnetic particles towards areas of lower gradient.[26] This force finds application in preventing the accumulation of oxygen bubbles on the electrode surface during OER.[28]

Magnetic fields also interact with electron spins of the catalyst. A principal factor in the sluggish kinetics of OER and ORR is that these reactions involve spin state changes: oxygen is triplet in its ground state, while hydroxide and water are both singlets, with no unpaired electrons. Changes from triplet to singlet or vice-versa are quantum mechanically forbidden, while singlet oxygen is significantly higher in energy than the triplet state. A catalyst is vital in facilitating a reaction pathway leading directly to and from triplet oxygen.[29] It has been proposed that the alignment of electron spins in the catalyst in the presence of a magnetic field, as well as stabilisation of high spin electron states in comparison to low spin states,[30] facilitates initial electron transfer processes between catalyst and reactant,[29] and selects spins such that high energy intermediates or activated complexes of unfavourable spin state are avoided as is illustrated in figure 3.[31] In contrast, Roy et. al. propose that the magnetic field enhances intersystem crossing of intermediate radical pairs from singlet to triplet state, preventing recombination and smoothing the way to complete the reaction to form triplet oxygen[28]. It is interesting that the facilitation of spin change through spin-orbit coupling is one of the reasons why heavy, precious metal catalysts like iridium, ruthenium or platinum are so active for the oxygen reaction: spin-orbit coupling allows nonradiative excitation and relaxation and hence spin changes while conserving angular momentum. Spin-orbit coupling becomes more significant as Z^4, making it far more significant for the precious metals than for the 1st row transition elements that are the preferred catalysis candidates. The external magnetic field could therefore be seen as an artificial strengthening for spin orbit coupling, allowing the needed spin changes to occur in the lighter element catalysts.

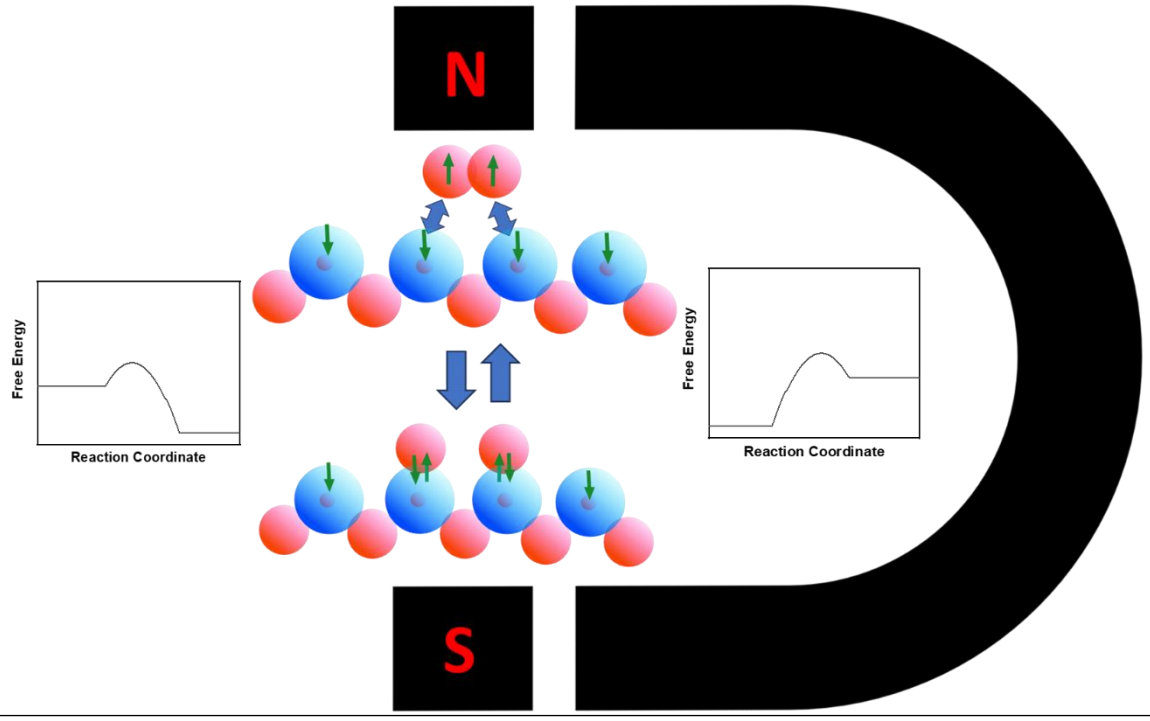
Figure 3: Visual summary of the electron spin effect of magnetic enhancement



Pauli exclusion principle does not allow parallel electrons to occupy the same orbital. In the randomly aligned spins of the catalyst, an antiparallel arrangement of spins on neighbouring metal centres will not allow reaction with triplet oxygen.



The reaction may proceed in two ways. Triplet oxygen must adsorb to a site where adjacent metal centres happen to have HOMO electrons with parallel spin, which effectively reduces the number of active sites. Alternatively, oxygen that has been excited to the singlet state as shown above may react at the antiparallel site. Both options reduce the rate of the reaction, leading to slow kinetics and high overpotentials.



The magnetic field provides the mechanism for spin changes in the catalyst, tending to align more electrons to form large magnetic domains where all metal centres have electrons of parallel spin. Reactions with triplet oxygen may then proceed rapidly and without the need for high energy intermediates like singlet oxygen.

Though the exact mechanisms involved are debated, it is clear that through some combination of the Lorentz and Kelvin forces, spin polarisation, and intersystem crossing effects, the application of an external magnetic field can enhance electrocatalysis.

In this work, we sought to combine the unique properties of high entropy material catalysts with the promise of magnetic enhancement to design an effective RZAB.

Chapter 2: Literature Review

2.1 History

Since the dawn of civilisation, deterioration has been part of the human experience. Our food rots, our buildings crumble, and our tools corrode. Maybe the ancients saw this simply as the will of malicious gods, or some human failing keeping us short of perfection. As enlightenment slowly crept across different parts of the world, a deeper understanding became common. Entropy increases with the surety of statistics, and things tend towards their lower energy states. Water tends towards the oceans, buildings tend towards ruin, and the vast reserve of oxygen and moisture in our atmosphere makes metal tools tend towards rust. These are simple facts of nature, iron laws of the universe that cannot be violated. Humans, being human, of course learn how to harness such processes for our benefit. In the same way a waterwheel may be placed in the way of a stream, an electrical circuit may be placed between the atmosphere and a metal. This is the foundation of the zinc-air battery and its successor, the rechargeable zinc air battery (RZAB).

Of course, the marvellous zinc-air battery did not emerge spontaneously. It was preceded by several different zinc-based batteries, starting with that invented by one of the fathers of the electrochemical field in his quest to win a bet. In 1799, Allesandro Volta published his “voltaic pile,” a device which could for the first time in history produce a continuous current. Unbeknownst to Volta himself, his device was driven by the reaction between zinc and water, catalysed by copper:

$$Zn + 2H_2O \rightarrow Zn^{2+} + 2OH^- + H_2 \qquad 0.76\ V \qquad (14)$$

This reaction, which produced 0.76 Volts (named after the man himself), would quickly lead to a revolution in the natural sciences. His invention was immediately followed by the discovery of electrochemical water splitting and the isolation of the elements sodium,

potassium, calcium, strontium, and boron. A reliable source of electricity would find use in research, transport, communication, medicine, and soon every aspect of life. The large-scale scientific and commercial use of electricity had begun, and the world would never be the same.[32]

Reaction 14, being the simple process of zinc corrosion, is not a fantastic source of energy, unless one is interested in capturing the hydrogen. In fact, in the modern RZABs that will be discussed in the following pages, this hydrogen evolving reaction is called a "parasitic reaction," an unwanted redox process that causes loss in energy and irreversible corrosion of the anode.[6,10,33]

Zinc based batteries would go through various iterations in the decades following the voltaic pile, including coupling to aqueous copper, nitric acid, and solid manganese oxide.[32] It was only 90 years later that the role of the atmosphere in a zinc based battery was first investigated,[32] though only as a "depolariser," a source of oxygen to react with the hydrogen from reaction 1 and prevent its build-up in the cell.[34] What seems to have gone largely unnoticed by these early chemists and inventors is the energy that might be supplied by the reduction of atmospheric oxygen. In 1932, the switch from acidic to alkaline electrolyte in the zinc batteries allowed the use of stable platinum on carbon as an oxygen reduction catalyst, and batteries for applications ranging from rail signals to communications to ocean navigation began to run on the familiar chemical reactions 10-13. In the 20th century, these reactions were seen as a one way street, with reuse requiring at least the replacement of the zinc anode. [32]

As the role of oxygen became better understood, the cathodes changed from carbon rods to thin layers of carbon to facilitate oxygen exchange, technology accelerated by advances in gas exchange membranes and fuel cells stemming from the cold war space race.[32] By the 1980's, zinc air batteries were sporting power densities in excess of 200 $W.h.kg^{-1}$, allowing a ZAB

powered electric van to cross the Alps. There were more innovations, changes to the anode and cathode, innovative cell designs and novel electrolytes. The sky was the limit. However, the 1980's marked the beginning of the end for the zinc air battery. The "rocking chair" battery, that would become the omnipresent lithium-intercalation battery, was invented.[35]

Lithium-ion intercalation batteries have obvious advantages. The battery is sealed, so the problems of electrolyte leakage and atmospheric interference, such as the dissolution of carbon dioxide in the electrode, are bypassed. It is relatively power-dense compared to early zinc-air batteries since the oxygen reduction and evolution reactions at the cathode are inherently sluggish. Most importantly, it was rechargeable, which was at best a distant dream for zinc-air batteries of the time. And so zinc, the anode that had helped spark the second industrial revolution, passed into obscurity, occasionally finding use in hearing aids and other low-power medical devices.

2.2 The Current Situation

2.2.1 The Limits of Lithium

Lithium-ion batteries remain dominant in the rechargeable battery market, but several drawbacks have become obvious. Toxic organic electrolytes threatened explosive failure of devices and vehicles, and lithium itself is a rare, expensive and strategically important resource. Some progress was and still is being made in alternative intercalation ions such as sodium, potassium and even zinc, as well as improvements to lithium-ion battery electrolytes, but progress has been painstaking and there is usually no guarantee of commercial success. The writing is on the wall: alternatives to lithium intercalation, which has dominated the markets for 30 years, must be found. The urgency of this need for new energy storage technologies has been exacerbated by environmental and climate fears, and the push towards green energy.

2.2.2 Climate Concerns

Climate change, much like the zinc air battery, is not a new idea. The earth is warm, while other terrestrial planets are cold and lifeless. The reason for this is our greenhouse effect, caused by gasses which absorb and scatter any infra-red radiation emitted from the earth's surface and so cause a general heating up of the atmosphere. Any gas that absorbs the blackbody radiation emitted by the earth as it cools after the absorption of solar energy is called a greenhouse gas. The most important among these gasses include water, methane, and the notorious carbon dioxide. While water is the overwhelmingly most abundant greenhouse gas in our atmosphere, carbon dioxide plays an important role. CO_2 absorbs radiation with wavelengths around 4.3 and 14.9 μm, which are precisely the regions where atmospheric water does *not* absorb radiation[36]. CO_2 therefore plays a far greater role in the greenhouse effect than its relatively low concentration would suggest. The increasing concentration of CO_2 in the atmosphere is slowly choking away the wavelength windows through which radiation can escape the earth. The energy output from the sun is relatively constant, while the energy that can escape the earth is increasingly being captured. The result can be predicted by any student of thermodynamics: a heating of the globe, or global warming. This relatively simple conclusion was not well received, as it meant that many of the technologies that had propelled humanity to its current level of prosperity were becoming problematic with continued and increasing use. The burning of fossil fuels for electricity and transport releases millions of tons of carbon dioxide every day, along with other gasses like the NO_x and SO_x families that independently impact pulmonary health in nearby humans. The direct consequences of the warming phenomenon include rising sea levels, changing weather patterns and disruptions to ocean currents as vast reserves of freshwater flow from shrinking glaciers. Indirect consequences include earlier springtime, warmer weather, and billions of desperate climate refugees as areas of the world become

unsuitable for agriculture or even uninhabitable as temperatures soar.[37,38] Disruption of the Gulf stream may actually cause northern Europe to become far colder in a twist of irony.[39]

Vigorous efforts to suppress the idea of global warming or "climate change" were quite successful in the late 20th and early 21st centuries. However, even fossil fuel companies have begun to admit that our current energy sources must be replaced, if only because fossil fuels will become depleted in the not-too-distant future.[40]

Nuclear fission power has unfortunately been hamstrung by public fear after the nuclear disasters at Chernobyl and the recent Fukushima disaster among others, and nuclear fusion is, as always, decades away. So, it is in renewable energy that we must place our hope.

2.2.3 Renewable Renaissance

Solar and wind energy have seen tremendous growth in research and commercialisation over the past decades, and today are cheaper per MWh than their fossil fuel alternatives even without considering the indirect health and environmental costs.[41] The benefits are obvious: solar panels and wind turbines produce no greenhouse gasses or air pollution while operating, and harvest energy sources that are for our purposes inexhaustible. Solar or wind "farms" can be set up at any scale, and almost anywhere. The cost of entry to the renewable energy market is so low that domestic energy users can set up solar panels on their own roofs.

However, all is not sunshine and blowing winds. As millions of people have said and written over the last 20 years, solar and wind power are intermittent, while power requirements are generally not. Additionally, the transport industries demand that energy be portable, a property conspicuously absent in 20-meter-tall wind turbines.

Renewable energy needs to be stored, and while innovative technologies like flywheels and pumped water may play a part, the renewable energy transition requires battery storage on all scales, from devices to vehicles to electrical grids. Up to the time of writing, lithium

intercalation batteries have been the technology of choice, but the problems already stated as well as the fact that the lithium batteries are consistently the most expensive part of a renewable energy program limit their ability to meet exponentially growing demands.[5,42,43]

2.2.4 Zinc for Net Zero?

Zinc started the electrification of the world in 1799, starting us on the path towards climate disaster. However, perhaps this element may offer a way out of this crisis as well. Interest in Zinc-Air batteries was rekindled in the early 2010's, as decades of investigation into oxygen catalysis for water splitting and fuel cells culminated in the concept of bifunctional oxygen catalysts: single materials that could catalyse not only the oxygen reduction reaction that allows the battery to discharge, but crucially also the hydroxide oxidation, or oxygen evolution reaction. This reaction takes place when an external potential strips electrons from water and hydroxide and forces them onto Zn^{2+} ions at the anode, regenerating the zinc metal that corroded away during discharge. This opened the door to rechargeable zinc-air batteries (RZABs) with a single catalyst and gas diffusion site, dramatically cutting down the bulk and weight of earlier, tentative RZAB designs that required separate catalyst layers for ORR and OER. A growing excitement emerged: here was the potential for a battery consisting of cheap and abundant materials, that forsook the dangerous electrolytes of intercalation batteries for a simple aqueous (or solid-state) electrolyte, and offered an energy density that could theoretically outstrip theorised ceiling for intercalation batteries by 400%.[6,7] The fact that the cathode uses atmospheric oxygen is another obvious draw, as this slashes the bulk and weight of practical cells which do not need a cathode compartment to store ions or chemicals, as is the case in conventional batteries.

All these advantages are well and good, but there is no denying that the road ahead for the RZAB is far from straight and easy. Every part of the RZAB has its associated problems and pitfalls, and despite the momentum in research there is no guarantee that the technology will

truly overtake intercalation batteries or other energy storage technologies. Let us address the factors that hold RZABs back from their destiny as the building blocks of the future.

2.3 Anode

The simplest anode is a metallic zinc plate, and this will be a useful starting point for exploring the challenges in anode design. The zinc anode undergoes a series of chemical and physical changes during the operation of the zinc air battery, summarised in reactions 2 and 3. During discharge, metallic zinc releases two electrons and so is oxidised to Zn^{2+} and enters solution as $Zn(OH)_2$. Being in solution is not a favourite pastime of Zn^{2+}, which parts from H_2O and is deposited as solid ZnO. During charge, aqueous Zn^{2+} is once again reduced to metallic zinc, making room for zinc oxide to enter solution again and then be reduced as well. Theoretically, this process regenerates a pristine anode, ready for action as if nothing had happened. However, the reality at the electrode surface is hostile to such perfect reversibility. ZnO can deposit anywhere during discharge, and often it is deposited on top of active Zn, in several layers. Zn that is not in contact with the alkaline electrolyte cannot be oxidised. In this way, the formation of ZnO layers on top of the anode passivates some areas, reducing the available anode area and increasing internal resistance. A similar problem is that Zn can deposit anywhere on the anode during charging, and it has a tendency not to distribute perfectly evenly. It is possible, especially at high current density, for slight Zn protrusions called dendrites to form. These dendrites have a relatively large surface area compared to a flat plate, and so zinc can deposit on them at a faster than average rate. This allows the dendrites to grow at an increasing rate, sending blades of zinc stabbing away from the anode surface over successive charge-discharge cycles. Apart from the decreased capacity due to internal resistance, the dendrites can pierce battery components to cause physical damage, or even reach the cathode and cause a short circuit.

The interface between zinc and electrolyte is also an area of concern. Recall reaction 14, where zinc reacts with water to produce zinc hydroxide and hydrogen gas. The aqueous electrolyte

has no shortage of water, and the precious metal catalysts like platinum that are commonly used at the cathode catalyse the hydrogen evolution half of the reaction:

$$2H_2O + 2e^- \rightarrow 2OH^- + H_2 \quad (15)$$

This "parasitic" reaction does not provide a great deal of energy, since much of the chemical potential remains caught in the hydrogen gas. The hydrogen may react uselessly with oxygen at the cathode, or build up in the battery where it can increase resistance, damage cell components, or ignite and rob RZABs of their "does not catch fire or explode" marketing angle.

2.4 Electrolyte

The fact that RZABs are necessarily in contact with the atmosphere holds another challenge for the aqueous electrolyte. As was mentioned in the opening paragraphs, our atmosphere contains carbon dioxide with a concentration that is increasing over time and is especially high near the industrial areas and roads where RZABs may be used. Apart from being a greenhouse gas, carbon dioxide has the troubling property of dissolving in water and forming carbonic acid, by equation 16:

$$H_2O_{(l)} + CO_{2(aq)} \rightarrow H_2CO_3 \quad (16)$$

As CO_2 partial pressure in the atmosphere increases, its concentration in water rises as well. In the environment, this causes a drop in pH in the ocean and other major water bodies, with potentially catastrophic consequences for marine ecosystems such as coral reefs.[44] A lowering of pH is also problematic in RZABs, as the CO_2 enters the electrolyte through the batteries gas exchange membranes and forms carbonic acid, which neutralises the alkaline electrolyte:

$$KOH_{(aq)} + H_2CO_{3(aq)} \rightarrow KHCO_{3(aq)} + H_2O_{(l)} \quad (17)$$

The resulting drop in $[OH^-]$ decreases the potential of equation 2, limiting the output voltage of the RZAB. It is a bitter irony that the increased concentration of carbon dioxide in the

atmosphere may handicap the very technology we need for the transition to a carbon neutral society.

2.5 Cathode

2.5.1 The Hidden Spintronics

Blame for limitations in power density and charging power efficiency can be lain at the door of the OER and ORR reactions. Their crimes also include hampering water splitting and fuel cell technologies. The lethargy of these reactions has therefore been studied extensively, and a major culprit has only recently emerged: the spintronics of the reactions.[45–47] The molecular orbital diagrams of the reactants in reaction 4 are shown in figure 4:

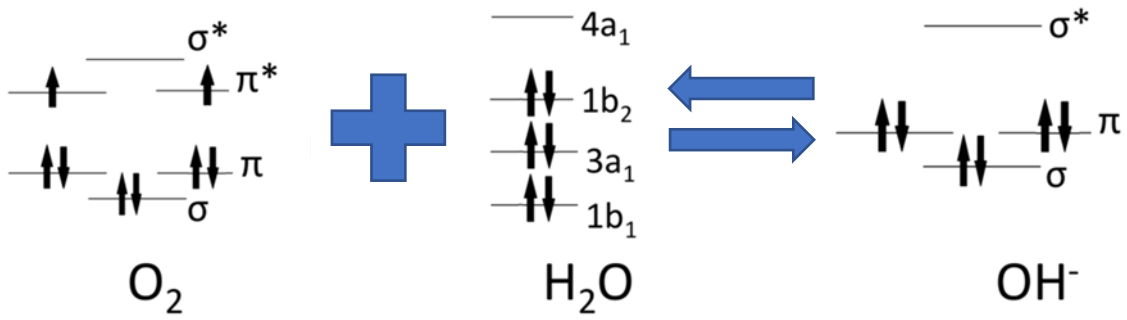


Figure 4: The molecular orbital (MO) diagrams of species involved in the ORR/OER reactions.

It is immediately obvious that ORR/OER involve spin changes between triplet oxygen and singlet hydroxide. Such a spin state change is referred to as a "spin-forbidden" reaction, because in isolation such changes in spin state cannot occur. Large activation energies combined with spin-coupling allow progress to a transition state with a changed spin state. Such events are relatively rare, and even after attaining this transition state, collapse back into the reactant state instead of proceeding toward the product is possible. All these factors combine to make spin-forbidden reactions extremely slow compared to spin-allowed

transitions, which leads to the need for expensive catalysts and high overpotentials.[31,45,48] Heavy, precious metal catalysts like platinum and iridium allow for very strong spin-orbit coupling, enabling the required spin changes. This is because spin-orbit coupling is proportional to Z^4, and so the difference between abundant transition metals and the precious platinum group metals is vast[49]. Combined with the favourable adsorption energies, these metals have become the gold standard of the oxygen reactions: platinum for ORR, and iridium for OER.

An important property of successful bifunctional catalysts is therefore the ability to select spins: that is, ensure that adsorbed reactants have the appropriate spin to react along spin allowed pathways. The oldest OER catalyst, Photosystem II in photosynthetic organisms, has been found to perform this spin selection using the magnetic active centre of the $CaMn_4O_5$ cofactor, which regulates the spins of reactants through exchange interactions, causing electrons to align with the unpaired electrons in the ferromagnetic enzyme active site.[50] As is so often the case in chemistry, artificial systems may be enhanced using strategies fine-tuned by nature: indeed, transition metal oxides that are ferromagnetic or antiferromagnetic outperform those that are paramagnetic.[31] The fields created by large magnetic domains compensate for individual atoms' weak spin-orbit coupling, allowing spin changes. Electrolysers and metal air batteries may use applied voltage instead of light to provide the impetus, but the chemist's reaction cells and a plant's mesophyll cells are performing the same reaction.

Ordered spins in the catalyst provide benefits on several levels. Chief among them are the thermodynamic effects of spin alignment: if reactants never need to go through high energy transition states like singlet oxygen (90 $kJ.mol^{-1}$ higher energy than ground state triplet oxygen), the activation energy is lower and hence the reaction rate higher. Entropy also plays a role: an unpaired electron moving from a disordered paramagnetic material to having a fixed spin in a product causes a decrease in entropy, whereas an aligned electron moving to a product

causes no great entropy change.[31] Finally, a magnetic field may inhibit reverse reactions by promoting intersystem crossing of photo or electrochemically generated radical pairs from singlet to triplet state, preventing their recombination.[28]

The effects of a magnetic catalyst can be further enhanced by including an external magnetic field in the system. (Indeed, a great deal of evidence points towards plant growth being aided by external fields in the 100 mT range.[51]) There has been some controversy on the nature of the enhancement by an external field, with furious debate on whether the magnetic field purely enhances mass transport or whether there are effects on the level of electron transfer processes. The mass transport school of thought argues that the twin contributions of the Lorentz and Kelvin forces are sufficient to explain the enhanced activities.

2.5.2 Lorentz Force Transport

The Lorentz force will be familiar to any first year student of physics: it is simply that perpendicular force experienced by any charged particle moving through a magnetic field, with the magnitude $\vec{F} = q(\vec{v} \times \vec{B})$ where F is the force, q is the particle's charge, v is the particle's velocity and B is the magnitude of the magnetic field. As implied by the cross product, the force acts perpendicularly to both the velocity and magnetic field direction, and is strongest when the velocity and field are perpendicular to each other. In any electrochemical system, we expect ions to be in motion, either towards or away from an electrode. An external magnetic field serves to exert an additional force on these ions, essentially stirring the solution. This is a potentially significant effect since mass transport considerations are of prime importance in catalysis and electrochemistry. By the Koutécky-Levich equation, the measured current obtained from an electrochemical system i depends on both the kinetic current i_k, limited by the reaction kinetics, and by the mass transfer current i_{MT}, according to the equation;

$\frac{1}{i} = \frac{1}{i_k} + \frac{1}{i_{MT}}$. The mass transport current is limited by how quickly reactants approach the

electrode and products depart. The additional acceleration from the Lorentz force is believed to accelerate these processes for cases where the reactant and/or products are ionic, such as hydroxide or hydronium ions in the particular case of OER/ORR, as well as disrupting the Helmholtz plane near the electrode surface and decreasing concentration polarization effects.[52,53] The introduction of additional diffusion currents using a magnetic field is known as magnetohydrodynamics. It should be noted that Lorentz effects on hydroxide and hydronium are unlikely, as these ions do not undergo generic mass transport under the effect of an electric potential. Rather, they propagate through the Grotthuss mechanism of protons "jumping" from oxygen ion to oxygen ion. While this may agitate the solution, the development of significant Lorentz force currents is not enabled. Indeed, studies by Garcés-Pineda et. al[48] showed that OER enhancement under the magnetic field was unchanged under increasing electrolyte agitation, suggesting that mass transport is not a significant contribution.

2.5.3 Magnetophoretic Transport

The second mass transport effect is the Kelvin force or magnetophoretic effect, which is exerted on paramagnetic species such as molecular oxygen to draw them from regions of lesser to regions of greater magnetic field strength: $F = \frac{1}{2}\mu_0\, c\chi\nabla B^2$ where c is concentration of the species, χ is its magnetic susceptibility, and μ_0 is the vacuum permeability. In the OER, the evolution of oxygen bubbles on the electrode surface at high current densities blocks catalyst sites, not allowing the electrolyte to contact the electrode. The Kelvin force serves to dislodge these bubbles of paramagnetic oxygen, freeing the surface.[26,54] Both the Lorentz and Kelvin forces are significantly stronger near ferromagnetic catalyst particles.[52,55] Indeed, mass transport effect are not seen when magnetic fields are applied to non-magnetic catalysts like IrO_2.[48] The forces exerted by the field alone, without the presence of magnetic particles to enhance it, are weak compared to the usual electric field and thermal effects on ions near an electrolyte.[53]

2.5.4 Electron transfer in a Field

The mass transport effects alone are not sufficient to explain the enhancement seen in electrocatalysis in the presence of an external magnetic field. It has been found that kinetic currents may be increased, and charge transfer resistance decreased after the application of the field, which cannot be caused by simple mass transport improvements. Additionally, changing reaction conditions impacts the extent of the magnetic enhancement: Garcés-Pineda et. al[48] found that magnetic enhancement is more significant for oxygen evolution under alkaline conditions than neutral conditions, controlling for electrolyte concentration. They ascribe this pH dependence to a change in the rate limiting step, with a non-spin-dependent step being the limiting step under neutral conditions, while under alkaline conditions the spin-dependent O-O bond formation step is rate-limiting.

A synergistic effect between ordered spins in the catalyst and the external field is likely, though the exact mechanism is unclear. It is possible that the external field simply enhances the effects of the magnetic catalyst, by aligning spins across the catalyst in the same direction so that the spin selection discussed earlier extends across the entire catalyst, rather than solely within small aligned domains. This is supported by temporary maintenance of enhanced activity of ferromagnetic catalysts after the external field is removed, at which point only the aligned spins of separate domains provide a magnetic field. It is also possible that the Zeeman effect, which increases the energy of electrons with their magnetic fields aligned antiparallel to the external field while decreasing the energy of electrons aligned parallel, facilitates electron transport: antiparallel electrons are donated more easily, while electrons can be more easily accepted into energy levels where they will be parallel to the field.

2.5.5 Practical Advances in the Field

Let us follow this discussion of the theoretical considerations with a few practical demonstrations that have hit the journals in recent years.

In those ancient days of 2016, Monzon et. al. examined increased ORR limiting current under an applied field of 360 mT. They found increases of 3%, 8% and 12% for zinc, cobalt and iron nanocrystal catalysts respectively. They ascribed this solely to magnetohydrodynamic effects, and the different responses of the metals to the extent of magnetisation of the nanocrystals.[27]

In 2017, Elias & Hegde[56] used an external magnetic field to enhance the hydrogen evolution reaction on nickel-tungsten alloy. They observed a 200 mV higher onset potential, which they also ascribed solely to magnetohydrodynamic effects and to the removal of hydrogen bubbles by the Kelvin force. They unfortunately did not yet consider the effects of the field on the OER in their full cell assembly.

Closer to modernity, an explosion of investigation into the spintronics of the oxygen reactions started in 2019. Garcez-Pineda et. al.[48] investigated nickel materials as catalysts under an external magnetic field. NiO, Raney Ni, $Ni_2Cr_2FeO_x$, $NiFe_2O_x$, $FeNi_4O_x$, $ZnFe_2O_x$, $NiZnFe_4O_x$, and NiZnFeO were tested, and a significant increase in current density was observed for the more ferromagnetic members of the series, most notably $NiZnFeO_x$. Li et. al.[57] demonstrated 50 mV earlier OER onset potential for a cobalt spinel oxide on carbon nanofibers after application of a 125 mT field perpendicular to the electric field, a result they ascribed to magnetohydrodynamics and changes to “electron energy states,” likely referring to low-spin to high-spin conversion as the magnetic field lowers the energy of the high spin state. Kiciński et. al. also extended the idea of spin selection into ORR applications for fuel cells, demonstrating a 30 mV higher onset potential under a 140 mT magnetic field.[53]

2020 saw a sharp decline in new research. Indeed, the only major research seems to be by Wesstson, Picker & Koper, who found no magnetic enhancement or OER or ORR on platinum nanoparticles.[58] (They did find that the adsorption energy of hydrogen on platinum could be influenced by a magnetic field, which has interesting implications for fuel cell and water splitting applications). This decline was not due to a lack of interest, however. Several reviews were published investigating the state of spintronic and magnetic enhancement.

Wang et. al.[59] brought magnetic enhancement to the zinc-air battery in 2021, using cobalt nanodots electrospun onto carbon nanofibers and a 350 mT magnetic field. They observed a 35 mV decrease in OER/ORR ΔE, with a 20 mV increase in $E_{1/2}$ and 15 mV decrease in $E_{j=10}$. The RZAB they assembled showed a 60 mV reduced ΔE after the field was applied, as well as significantly greater stability than the same system without a magnetic field present. Their analysis acknowledges the role of spin selection in the significant improvement.

Zhang et. al. proposed an interesting alternative to the operando magnetic field in 2022. Instead, they employed an external magnetic field during the annealing process, forming already magnetized $FeCo_2O_4$ nanoparticles.[60] OER/ORR ΔE was reduced by 80 mV compared to the traditionally annealed material, and their RZAB showed an increase in peak power of 18 $mW.cm^{-2}$. In addition to the effects of spin selection, this approach alters nanoparticles' active surfaces, giving an additional benefit as well as simplifying potential applications of magnetic enhancement: instead of manufacturing devices with bulky and expensive magnets attached (which would have to be further shielded to protect adjacent electronics), the cathode material itself may be magnetized prior to device assembly.

In 2023, Zhang et al applied a 1 T magnetic field to their bifunctional $FeCo_2O_4$ spinel catalyst and rechargeable zinc-air battery. They observed a 40 mV earlier OER onset, 10 $mW.cm^{-2}$

improved peak power, and a 10 Ω decrease in charge transfer resistance. As expected, mass transport resistance was unchanged.[61]

Recent research into the use of magnetic fields in OER/ORR catalysis is summarised in table 1:

Table 1: Summary of research in oxygen catalysis with magnetic fields

Catalyst	**Magnetic Field/ mT**	**OER E_{10} /V**	**ORR $E_{1/2}$ /V**	**ΔE/ mV**	**Reference**
Co/CNF	0	1.650	0.800	850	[1][59]
	350	1.635	0.820	820	
$FeCo_2O_4$ nanofibre	0	1.580	N/A	N/A	[2][61]
	1000	1.540	N/A	N/A	
$FeCo_2O_4$	0	1.58	0.78	800	[3][60]
	Residual	1.52	0.80	720	
Ni1.5Co1.5O4/Ni foam	0	1.520	N/A	N/A	[4][62]
	125	1.478	N/A	N/A	
(Fe+N+S)/C	0	N/A	0.88	N/A	[5][53]
	140	N/A	0.91	N/A	

As new research continues to flow and ever more novel approaches to and uses of spin selection and magnetic enhancement are discovered, this aspect of heterogenous catalysis will become increasingly important and useful in coming years.

2.6 Material design

2.6.1 Bifunctionality

The recent investigation into spintronics and magnetic catalysts is a deviation from traditional catalysts, which include nonmagnetic platinum on carbon for ORR, and iridium or ruthenium oxide for OER. They are still commercially favoured in fuel cells and water splitting respectively, despite poor stability and extremely high cost.[63] In RZABs they have an additional drawback in that their activity tends towards only one of the reactions: Pt/C is a poor OER catalyst, while IrO_2 has little activity for ORR. Using them in a RZAB cathode therefore means fabricating a system involving both catalysts, increasing costs and complicating both the manufacture and operation of the cell. For RZABs to be truly viable, catalysts must be bifunctional, with a good activity towards both OER and ORR. This bifunctionality may be quantified by the ΔE, the difference in onset between the ORR and OER reactions. OER and ORR occur at different voltages and being favoured by materials with different structures and with different optimum adsorption energies of intermediates. An OER catalyst must adsorb OH^- and readily desorb O_2, while an ORR catalyst adsorbs O_2 and is inhibited by strongly adsorbed OH^- or H_2O, and these opposing priorities are a clear problem for a catalyst that must do both.[10,11] Despite this, there has been some success in the field of bifunctional catalysis using transition metal oxides.[7,31,33,64] It should come as no surprise that a good fraction of these bifunctional catalysts also display magnetic properties.

Gorlin et. al.[11] used EXAFS studies on MnO_x catalysts to show that the material underwent a structural reorganisation as the voltage was varied between the 0.7 V vs RHE applicable for ORR, and the 1.8 V conditions for OER. At 0.7 V a disordered $Mn_3^{II,III,III}O_4$ structure was

evident. This structure was oxidised to a layered birnessite structure where manganese is mainly in the III and IV oxidation state. While this restructuring is fascinating, such significant structural changes repeated every time the voltage is varied is not ideal for a commercial bifunctional catalyst, which must be stable over an extended period of use. Indeed, such restructuring over the wide operating voltage window limits the use of air cathodes with multiple catalysts: for example, the mixture Pt/C + IrO_2 on the catalyst layer sees the platinum giving a high ORR activity while the iridium handles the OER. However, the platinum surface typically degrades at the OER potentials, while the IrO_2 surface is slowly reduced over consecutive charge-discharge cycles.[6] Significant structural changes between OER and ORR potentials is therefore more a drawback than a viable strategy for promoting bifunctionality.

Other bifunctional catalysts may be synthesized in such a way that distinct active sites are created. For example, Cui et. al. showed that a nickel-iron nitride support with iron-platinum alloy nanoparticles showed good OER/ORR bifunctionality, as the nitride was highly active for OER while the alloy was more active for ORR.[65] Of course such catalysts may require relatively complex syntheses, while not eliminating the use of rare metals. Spinel structured metal oxides such as Co_3O_4 are intrinsically bifunctional, though it is significantly more active towards OER than ORR. Activity towards both reactions have been enhanced by doping and the synthesis of bi- or tri- metallic spinel oxides such as $NiCo_2O_4$ or $CuCo_2O_4$, as the additional metals modify the valence band energetics and have synergistic effects, such as better optimising adsorption energies and preventing structural changes over large potential changes.[6,66]

2.6.2 High Entropy Materials

Careful synthesis, doping and rational design has been successful in reducing ΔE, however an alternative strategy has been gaining momentum in recent years. Instead of slightly altering the composition of a parent material, it is possible to create solid solutions of many metals in

equimolar proportions, creating single phased materials with properties that deviate wildly from the linear relations seen in conservative doping. Catalysis has entered the realm of high entropy materials.

The concept of a high entropy material (HEM) was almost simultaneously described by Cantor et. al. and Yeh et. al. in 2004. They found that alloys containing at least 5 metals in equimolar proportions exhibited exciting features. Their high conformational entropy- greater than 1.5 R- favoured the formation of single phased solid solution as opposed to multiple phases seen when traditional materials are doped with too much enthusiasm. The high conformational entropy, as well as the heavily distorted lattice caused by atoms of different sizes coexisting in a single phase, also stabilised the materials, preventing degradation.[20,67,68] The proximity of so many metal atoms leads to an additional effect, dubbed the "cocktail effect," a rather nondescriptive catchall phrase for the synergies that arise from this situation. These effects could include modified energy levels, unique binding energies, magnetic or even superconducting properties.[69]

Like many discoveries, high entropy alloys (HEAs) were not immediately recognised as the significant breakthrough they are. Part of the delay is perhaps due to the vast space that is opened by the HEAs. Traditional alloys consist of a single principal element with one or two additives or dopants, yet still thousands of traditional alloys find applications in the modern world. HEAs consist of at least 5 metals in near equimolar proportions, allowing for exponentially more combinations than traditional alloys. The first row of the D-block alone gives over 600 equimolar HEA possibilities, each with unpredictable properties or potential applications. In the decades since 2004, researchers have slowly discovered various applications of various compositions of high entropy alloy, including interesting structural, magnetic, electronic and superconducting properties. One of the more recent fields to investigate this potentially limitless space is that of catalysis: the high entropy and distorted

lattice effects enhance the stability of the catalyst under harsh and varied conditions, while the cocktail effect grants HEMs an astounding variety of useful properties, including tuneable adsorption strengths, valence band energies, and unique active site geometries.[70]

One of the first forays into HEMs as catalysts was by Yao et. al. in 2018, when they experimented on the creation of HEA nanoparticles by carbothermal shock synthesis,[71] successfully synthesising a variety of alloys with up to 8 components. They demonstrated a good ammonia oxidation catalyst in PtPdRhRuCe, achieving 100% ammonia conversion with 99% selectivity for NO_x products. While their catalysts were platinum-group metal heavy, they successfully proved the concept of HEM catalysts and opened the door to subsequent investigations.

2.6.3 High Entropy Spinels

The discovery that the factors that give HEAs their unique properties are not unique to alloys has expanded the space for investigation even further. In 2015, Rost et. al. [72] demonstrated the formation of the "entropy stabilised oxide" $(CuCoMgNiZn)O_x$. They used energy dispersive spectroscopy in scanning transmission electron microscopy (STEM-EDS) to show the co-occurrence of all 5 metals, and further confirmed the high entropy nature using extended x-ray absorption fine structures (EXAFS) synchrotron experiments. They found that the four transition metals had very similar cation-cation distances. These results combine to show that the rock-salt oxide was indeed a solid solution, with lattice positions randomly occupied by the metal cations. Furthermore, they found the single solution did not form when any of the precursor metal salts were removed- i.e. 4 component oxides did not form a solid solution, confirming the influence of the high entropy effect in an ionic solid. High entropy oxides, sulphides,[73] phosphates,[73] spinels,[74] perovskites,[75,76] and metal-organic frameworks[77] are just a few of the examples that have been explored since this proof of concept. These more complex HEMs offer even greater tunability than HEAs. In the ionic HEMs, for example, we see

essentially two lattices: the anion lattice following a traditional crystal structure, and the cation lattice where the metals take up their random occupancy. While the cation sites have the same level of variability as the alloys, the anion lattice is also up for modification. An oxide can take a rock salt, spinel, or perovskite structure depending on the exact conditions, and each of these can be further modified by introducing oxygen defects and vacancies, or activating lattice oxygens.[70] Feng et. al.[78] used the same quinary HEO formula as Rost et. al., but synthesized a porous layered structure using a sacrificial graphene oxide template to produce a catalyst that was stable, highly active for benzyl alcohol oxidation, and with a highly controllable selectivity for the oxidation product: the product could be varied by simply altering reaction temperature while maintaining yields of over 90%. The nanosized HEO is rich in oxygen vacancies as analysed using XPS, with their density tuneable by adjusting the calcination temperature during synthesis. The propensity of the HEO to form surface oxygen defects exposes more metal ions as active sites and improves the reactants' binding energies.

Conductivity of HESO catalysts is a challenge, however. Spinels conduct electricity through the nearest-neighbour small polaron hopping mechanism. Electrons must "hop" from ion to ion through the lattice, at each step distorting the surrounding structure. In material science, a travelling distortion is called a phonon, and this moving electron accompanied by a phonon distortion is called a polaron. They found that polaron hopping is favourable only when moving between like atoms, as the energy gained in one site's charge increases and surrounding distortion equals the energy lost from the next as the charge decreases and distortion relaxes. This process is therefore adiabatic. However, when jumping between unlike atoms, energy changes take place, resulting in such events having much higher activation energy. In higher order spinels such as high entropy spinels, paths of adjacent like atoms are rare, and so conductivity is lower.[79,80] HESO electrocatalysts are therefore poorly conductive, a problem overcome by incorporation into an appropriately conductive support.

2.6.4 Bifunctional OER/ORR HEM Catalysts

Characterisation of novel HEMs remained, and will always remain challenging, but the groundwork was laid for their use as technologically relevant catalysts. A new weapon against the endless demands of the OER and ORR was proven viable, and a staggering level of resources has since been thrown into HEM OER/ORR catalysis in general and RZABs in particular. Some of the significant papers on bifunctional HEM RZAB cathode catalysts are shown in table 2:

Table 2: A selection of recent publications on HEM bifunctional OER/ORR catalysts

Year	Catalyst	OER E_{10} /V	ORR $E_{1/2}$ /V	ΔE/ V	Reference
2023	AlNiCoFeCrMoV/Co-N-C	1.504	0.864	0.640	[81][81]
2022	PtPdAuAgCuIrRu/ $(AlNiCoFeCrMoTi)_3O_4$	1.49	0.89	0.600	[82][82]
2023	CrMnFeCoNi	1.51	0.78	0.734	[83][83]
2020	AlNiCoRuMo	1.485	0.875	0.610	[84][84]
2020	AlFeCoNiCr HEA/HEO system	1.47	0.68	0.790	[85][85]
2023	$Fe_{12}Ni_{23}Cr_{10}Co_{30}Mn_{25}$/CNT	1.55	0.85	0.700	[86][86]
2021	$Mn_{70}Ni_{7.5}Cu_{7.5}Co_{4.2}V_{4.2}Fe_2Mo_2Pd_{0.5}Pt_{0.5}Au_{0.5}Ru_{0.5}Ir_{0.5}$	1.44	0.90	0.540	[87][87]
2021	$(AlNiCoFeCr)_3O_4$/Ag	1.51	0.74	0.770	[88][88]

A wider search will reveal hundreds of papers exploring the HEM space for electrocatalysis of OER or ORR alone. While researchers continue to explore novel HEMs, it may also be time to start applying other promising techniques to HEMs. In the same way a HEM's many elements give rise to a cocktail effect of unpredictable synergies, combining HEMs with methods like stress, light, and electric or magnetic field enhancement could reveal breakthroughs in the field of oxygen catalysis.

2.6.5 $(CuCoFeMnNi)_3O_4$

In 2019, Wang et. al. explored $(CuCoFeMnNi)_3O_4$ high entropy spinel nanoparticles as an oxygen evolution electrocatalyst.[89] They were able to synthesize particles with diameters of 5 nm using a solvothermal synthesis, avoiding the need for extreme temperatures to attain the high entropy effect. XPS was used to probe the oxidation states of the metal ions. While copper was found almost exclusively in the Cu^{2+} state, indicating occupation of tetrahedral voids only, the other 4 metals showed a random distribution between the octahedral and tetrahedral sites. The catalyst showed promising activity for OER, but had a low electrical conductivity and required support on multi-walled carbon nanotubes. The 5 metals were chosen for their similar size across oxidation states and ease of mixing in their binary and ternary systems.

The metal combination used is more interesting than Wang et. al. give it credit for. For OER, iron and cobalt oxides show an optimum adsorption energy for reactants and products, while manganese oxides and nickel oxides show slightly stronger or weaker than ideal binding energies, respectively.[90,91] Their combination is therefore promising, as they could form active sites that both strongly adsorb reactants and easily release products. For example, binary oxides of iron, cobalt and nickel have given good OER activity[92]. For ORR, copper binds oxygen most weakly (closest to the optimum binding energy where platinum and palladium are found) with Ni, Co and Fe binding oxygen progressively more strongly.[92] This once again allows active sites where good reactant adsorption and good product desorption can be combined. Altogether, $(CuCoFeMnNi)_3O_4$, called HESO from here on, and the composite with conductive carbon, called HESO/C from here on, should be a single phased spinel exhibiting good reactant and product binding energies, a distorted lattice promoting active electrons for catalysis, richness in reactive oxygen defects, and ferromagnetic properties ready for enhancement by an external magnetic field.

Chapter 3: Materials and Methods

3.1 Reagents

>98% Purity cobalt II nitrate hexahydrate was obtained from ACE chemicals. >98% Purity copper II nitrate trihydrate and iron III nitrate nonahydrate were obtained from Sigma Aldrich

>97% Purity manganese II nitrate tetrahydrate was obtained from Sigma Aldritch

>99% Purity nickel II nitrate hexahydrate was obtained from Fluka Chemika

>99.5% Purity zinc acetate was obtained from UNIVAR.

5% Nafion 117 and 60 Wt. % polytetrafluoroethylene dispersed in water were obtained from Aldrich

Anhydrous ethylene glycol with a 99.8% purity was obtained from Sigma Aldritch

Potassium hydroxide electrolytes were made using >85% KOH pellets from ACE chemicals and water purified using a Purelab Flex device.

Vulcan carbon and OLC were obtained from Sigma Aldrich. All reagents were used as received, without further purification.

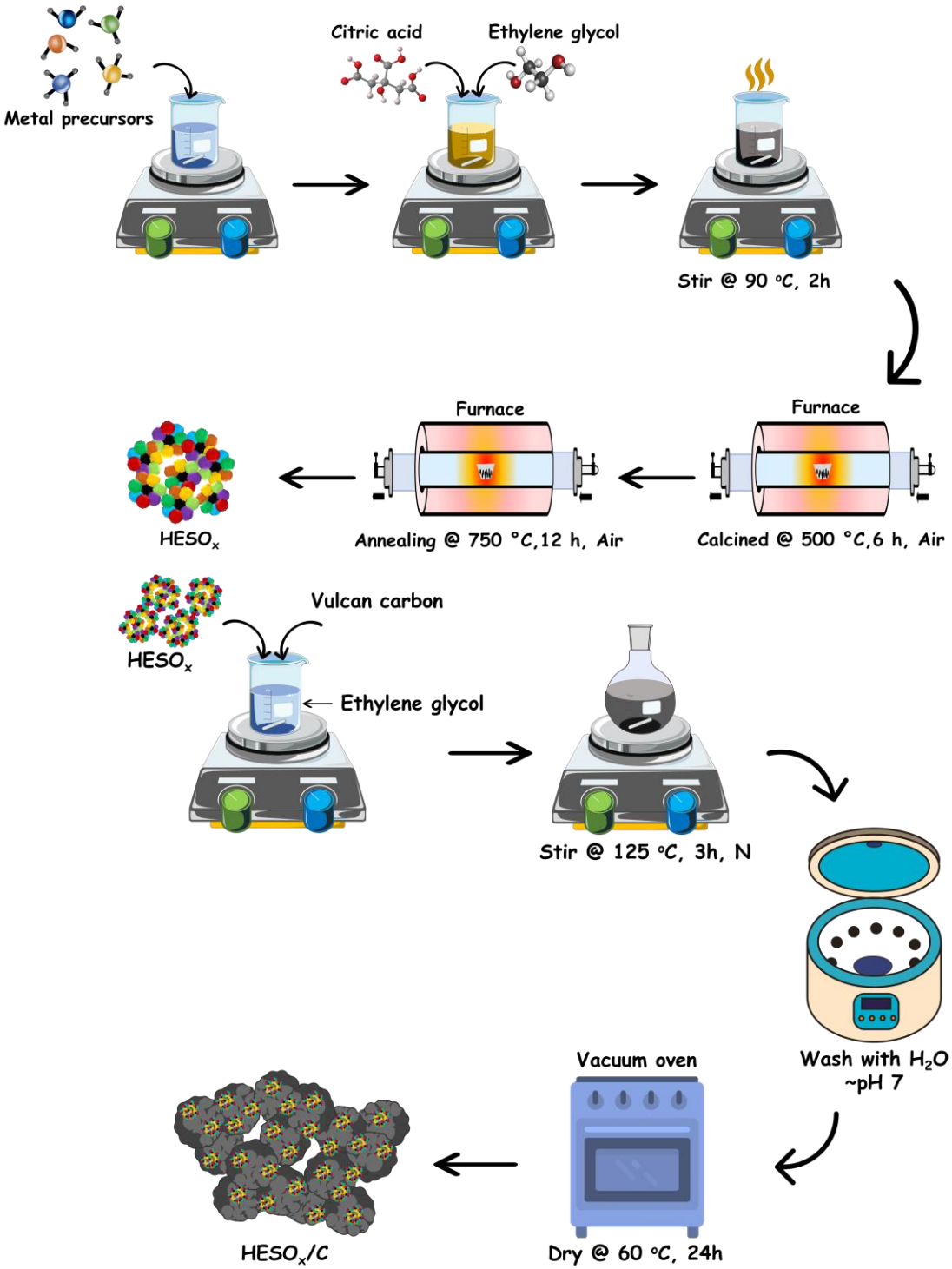
3.2 Syntheses

The HESO was prepared by the Pechini method[93]: equimolar amounts of each nitrate salt were dissolved in water. The solution was heated to evaporate the water, giving a gel that was then pyrolyzed. The product was calcined at 500 °C to obtain $(CuCoFeMnNi)_3O_4$. This was then annealed in air at 750 ˚C for 12 hours. This annealed product will be referred to as HESO, for High Entropy Spinel Oxide.

Dispersal on carbon was done as follows: Appropriate masses of carbon and HEO were dispersed separately in ethylene glycol. The HEO was added dropwise to the carbon and mixed under nitrogen. The mixture was then stirred and heated at 125 ˚C for 3 hours, still under nitrogen. The product was obtained by filtration and washed with distilled water. The synthesis

scheme is shown in figure 5. This supported catalyst will be referred to as HESO/C, for High Entropy Spinel Oxide on Vulcan Carbon

Figure 5: Synthesis schemes of HESO and HESO/C



3.3 Characterisation

3.3.1 Powder X-Ray Diffraction (PXRD)

The powder x-ray diffraction (PXRD) data was collected at the Canadian Light Source Brockhouse lower energy wiggler beamline using a Huber diffractometer and a Mythen1k detector. The samples were placed in 0.54 mm diameter Kapton capillaries and were spun during the measurements to improve statistics. The beamline photon energy was 15.1328 eV // wavelength of 0.819308 Angstroms. Rietveld refinements were done using GSAS II and TOPAS V7 software.

XRD is a characterisation method that takes advantage of the symmetries of solid, particularly crystalline, materials. X-rays of a specific wavelength are radiated onto a sample, where they diffract from the material according to Braggs law: $n\lambda = 2dsin\theta$ where λ is the x-ray wavelength, d is the spacing between the atom layers, and θ is the angle between the incident x-rays and the atomic planes. Θ values where this Bragg condition is satisfied will result in intensity maxima of diffracted x-rays. By recording the angles where Braggs law are satisfied, the interplanar spacing 'd' can be found, and a full spectrum can give sufficient information to elucidate the crystal structure. In powder x-ray diffraction, the sample consists of many randomly oriented crystallites, and so information in a powder x-ray diffraction pattern is less powerful for elucidation. However, using other structural information, even a powder pattern can be used to determine accurate crystal lattice parameters. Crystal databases contain tens of thousands of PXRD patterns, and can be used to find possible matches to the pattern in question. For novel, defective, strained or otherwise modified materials that need their structures investigated, there is Rietveld refinement. This method is named after Hugo Rietveld, who in the 1960's helped pioneer automation of structure elucidation. The idea is elegant: rather than generate a structure from XRD data, we generate theoretical XRD data from approximate structure and experimental parameters. Once a theoretical XRD pattern is

generated, the refinement process begins. Adjustments to parameters are made, and the change in the theoretical pattern tracked, with the goal of minimising the mean squares deviation from the experimental pattern. This is process that repeats until a minimum deviation is reached. There is great flexibility in which parameters that can be "refined" in this way, including but limited to any or all of the lattice parameters, crystallite size, background, microstrain, atomic positions, or occupancies. Of course, this process would be impractically tedious to do by hand, but can be realised using computation. Using punch cards and an Electrologica X1 computer, Rietfeld et. al. was able to compute the simultaneous refinement of 33 parameters of a neutron diffraction pattern, and modern computers can handle even more complex refinements.[94] Of course, such a powerful process comes with great responsibility. The final refinement is sensitive to the accuracy of the initial assumptions, and it is very easy to obtain outrageously incorrect conclusions from an improper refinement.

3.3.2 Total Scattering – Pair Distribution Function (PDF) analysis

Total scattering data was collected at the ID11 beamline at the ESRF and used in conjunction with the XRD data to determine the pair distribution function (PDF) The X-ray wavelength used was 0.819308 nm. This technique gives a weighted distribution of inter-atomic distances. It therefore does not require long-range order as PXRD does, and importantly is not limited by peak broadening in small nanocrystalline materials.[95]

Background subtraction, normalization, and Fourier transformation of the data was done using PDFgetX3 within xPDFsuite. The total scattering structure function S(Q) is obtained from the coherent scattering intensities $I_c(Q)$, after removal of the self-scattering by,

$$S(Q) = \frac{I_c(Q)/N - \langle f(Q)^2 \rangle + \langle f(\mathrm{Q}) \rangle^2}{\langle f(\mathrm{Q}) \rangle^2}$$

Q is the magnitude of the scattering momentum transfer ($Q = 4\pi \sin(\theta)/\lambda$ for elastic scattering, where λ is the wavelength, and 2θ is the scattering angle). $\langle f(\mathrm{Q}) \rangle$ is the average atomic form factor over all atoms in the sample. The experimental PDF is obtained via truncated Fourier transformation,

$$G(r) = \frac{2}{\pi} \int_{Q_{min}}^{Q_{max}} Q[S(Q) - 1] \sin(Qr)\, dQ$$

and is related to the density distribution by;

$$G(r) = 4\pi r\, [\rho(r) - \rho_0 \gamma_0]$$

where ρ_0 is the average atomic number density and $\rho(r)$ is the local atomic pair density, which is the average density of neighboring atoms at a distance r from an atom at the origin. γ_0 is the characteristic function of the diffracting domains which equals 1 for bulk crystals, but has an r-dependence for nanosized domains. The PDFs were determined with $Q_{max} = 25$ Å^{-1}. The instrumental resolution effects were determined by structure refinement to the reference CeO_2 sample resulting in values of $Q_{damp} = 0.02971$ Å^{-1} and $Q_{broad} = 0.03443$ Å^{-1}, which were fixed for subsequent refinements.

PDF refinements were performed using the program PDFgui. As in XRD, PDF refinement is a process of creating a model and calculating its theoretical PDF, and then comparing it to the observed PDF. The model is then altered to improve the correlation with the experimental PDF. The deviation between $G(r)_{experimental}$ and $G(r)_{calculated}$ is minimised to find a model that most closely matches reality, if the assumptions used to initiate refinement were correct. The refined parameters for each phase in the multiphase refinements included the lattice parameters by symmetry, phase specific scale factors, separate isotropic atomic displacement parameters for metal and oxygen atoms, an r-dependent peak sharpening term, $\delta 1$, to account for short-range

correlated motion, and a damping factor associated with finite spherical domain sizes, defined as

$$\gamma(r)_{sphere} = \left[1 - \frac{3r}{2d} + \frac{1}{2}\left(\frac{r}{d}\right)^3\right] H(d - r)$$

where d is the domain diameter. $H(r)$ is a step function with value 1 for $r \leq d$ and 0 beyond. The PDF is simulated from a structure model by calculating the radial distribution function as

$$R(r) = \frac{1}{N} \sum_{i,J \neq i} \frac{f_i^* f_j}{\langle f \rangle^2} \delta(r - r_{ij})$$

where f_j is the X-ray atomic form factor evaluated at $Q = 0$, and the delta functions are broadened by contributions from the atomic displacement parameters, Q_{max}, Q_{broad}, and δ1. The overall equation,

$$G(r) = \left(\frac{R(r)}{r} - 4\pi r \rho_0\right) \gamma(r)_{sphere}$$

then gives the PDF for the model.[95]

3.3.2 Raman

When radiation is scattered by an atom, molecule or structural motif in a crystal, the wavelength may change. Stokes-Raman scattering is the phenomenon where the scattered light has a lower wavelength than the incident radiation: the incident light excites an electron to a higher energy state, after which the electron returns to an intermediate energy state instead of the ground state. The change in energy of the scattered light is highly dependent on the electronic environment, and so can give chemical and structural information. Raman spectroscopy is done by illuminating a sample with a monochromatic laser, and measuring the energy and intensity of the scattered light. This is used to produce a graph of intensity vs Raman shift, or the deviation from the illuminating energy, in inverse centimetres. One common use of Raman spectroscopy,

for example, is to quantify the relative frequency of sp^2 compared to sp^3 hybridised carbon in a sample. This is important in carbon-supported catalysts. Sp^2 hybridised or graphitic carbon forms conductive layers but is unreactive, and does not provide strong electronic metal-carbon interaction (EMSI). However, sp^3 hybridised carbon atoms are associated with defects and dangling carbon bonds, able to interact more strongly with the catalyst.[96]

Raman data was collected suing a 514.5 nm (green) line, Lexel Model 95 SHG argon ion laser, as is recommended for the study of metal-oxides and various inorganic systems. The short wavelength allows higher power than when using less energetic photons, improving Raman signal. The beam can also be more tightly focussed than longer wavelength lasers, increasing intensity at the sample and so increasing the Raman signal as well.[97,98]

3.3.3 Microscopy

Visible light microscopy reaches a limit when one wants to resolve detail finer than the wavelength of the light used. By accelerating electrons through a powerful potential, a beam of electrons with very short wavelengths may be produced. A beam of high energy electrons may be focussed in a narrower beam than is possible with visible light, giving electron microscopes far greater resolution. There are two general methods to electron microscopy: surface bombardment in scanning electron microscopy (SEM), and transmission in transmission electron microscopy (TEM).

In SEM, electrons are focussed into a beam and scanned over the surface of the sample in a raster pattern. Data is collected at each point of the pattern, and includes scattered electrons, secondary electrons, and emitted x-rays. This data can be interpreted as simply pixels of varying brightness to give a greyscale image of the surface, or can be used to generate elemental maps using the characteristic x-rays emitted (known as energy dispersive spectroscopy or EDS)

In TEM, the electron beam passes through the sample and impacts a detector on the other side. The electrons interact with the atoms of the sample on their way through, altering their phase and intensity, and so an image of the sample is created on the detector. There are many different modes in which TEM can be used and many ways to generate the contrast in the image. In this research the focus was on identifying crystal grains and d spacing.

SEM was done using a Zeiss Auriga Field Emissions SEM after mounting the samples on carbon tape and coating using an Epitech Carbon Coater. The software used was SmartSEM.

EDS was done using a Zeiss Crossbeam 540 operated at 2 kV for imaging and 20 kV for EDS. Data was acquired using an Oxford Xmax detector with Aztec software optimised using copper reference.

TEM was performed using a JEOL JEM 2100 at 200 kV. Samples were sonicated in ethanol before being dispersed on a carbon-coated copper grid

3.3.4 X-ray Photoelectron Spectroscopy (XPS)

X-ray photoelectron spectroscopy is based on the photoelectric effect. The photons bombard the sample, and have a chance of being absorbed by electrons therein. If the photon energy is sufficient to allow the electron to escape the atom, a free “photoelectron” is produced with a kinetic energy equal to the difference between the energy of the incident photon and the work function. By measuring the kinetic energy of the photoelectrons and subtracting the photon energy, a spectrum of work functions is made. This allows one to identify both the elements present in the sample as well as their oxidation states and chemical environments, as these modify the work function. The element, environment and oxidation state will determine the energy, and the relative abundance of the species will determine the area under the XPS peak.

XPS was performed using an ESCAlab 250Xi instrument from Thermo. Monochromatic Al kα radiation (1486.7 eV) was used. X-ray power was 300 W and spot size was 900μm. Pass energy

was 100 eV for survey scans and 20 eV for high-resolution scans. Pressure in the system was less than 10^{-8} mBar. Spectra were analysed using CASA-XPS and Origin software. Shirley background analysis was used.

3.3.5 Electron Paramagnetic Resonance (EPR)

Electron Paramagnetic resonance is used to probe the chemical environments and relative amounts of unpaired electrons in a sample. In oxides such as the spinel under investigation, the EPR intensity is closely correlated to the concentration O^-, where the oxygen ion has an unpaired reactive electron. O^- is of particular interest as an indicator of the surface defect concentration, which in turn indicates the abundance of active sites for electrocatalysis.[99,100] EPR is based on the Zeeman effect: a magnetic field applied to a sample causes the unpaired electrons to align either parallel or antiparallel to the field, which lowers or raises their energy, respectively. A radio-frequency photon can be absorbed by a low energy electron, temporarily flipping it to anti-parallel alignment. An EPR device works by applying a constant radio frequency to a sample and slowly varying the magnetic field while monitoring the absorption of radio photons, taking care that the sample not become saturated. When the magnetic field induces a Zeeman effect splitting equal to the photon energy, absorption will take place. The signal is always broad due to time-energy uncertainty, and so the derivative of the signal is used. The photon energy and magnetic field strength can trivially be used to find the electron g factor, using the equation $h\nu = g_e B_0 \mu_B$ where h is the Planck constant, ν is the radio frequency, B_0 is the magnetic field strength, and μ_B is the Bohr magneton. Any deviation from the free electron g factor of 2.0023 is caused by the chemical environment of the unpaired electron. Interpretation is similar to nuclear magnetic resonance experiments: a lower g value can be due to shielding, and a signal may be split by nearby spins such as other unpaired electrons or nuclei leading to doublets, triplets, and so on. Such splitting is referred to as the fine structure. The g-

factor is in fact a tensor rather than a scalar, with x, y and z components to account for spatial anisotropy, however this was not relevant for the experiments in this work.

3.3.6 Ultraviolet and Visible light Spectroscopy (UV-VIS)

Ultraviolet-visible light spectroscopy measures the wavelengths and intensities of light absorbed by a sample in the UV and visible regions. The absorption is due to electrons being excited to higher energy levels, but unlike in photoelectron spectroscopies the electrons remain bound. This technique is used to gain insight into the electronic structure of samples. In crystalline materials, the band gap, or energy difference between the highest occupied and lowest unoccupied electron energy levels, is of particular interest. The band gap classifies the material as a conductor, semiconductor or insulator, and the exact magnitude of the band gap must be tuned depending on the application. For example, electrocatalysts should generally have lower band gaps as compared to photocatalysts as they must conduct electrons as well as catalysing a reaction. The band gap can be found using the Tauc equation

$$(\alpha h\nu)^{\gamma} = A(h\nu - E_g)$$

Where α is the absorption coefficient, h is the Planck constant, v is the frequency of the light, A is a proportionality constant, and E_g is the band gap. γ is 2 if the band gap transition is direct, or 0.5 if it is indirect. In a direct band gap material, electrons may be promoted directly to the conduction band. In an indirect band gap material, however, the highest energy occupied and lowest energy unoccupied electron orbitals have different momenta, and so a transition would violate conservation of momentum. A phonon that alters the orbital momentum or imparts momentum to the electron is therefore required before the transition may occur.

A Tauc plot is constructed by plotting $(\alpha h\nu)^{\gamma}$ against hv, where $\alpha = \frac{Absorbance \cdot ln10}{length}$. As no prior literature has investigated this HESO by UV-VIS spectroscopy, γ is not known, and so plots of both values are required. The correct value gives a plot with a well defined linear region. The

linear region is extrapolated down to $(\alpha h\nu)^{\gamma} = 0$, and the value of hv is then taken as the band gap.[101]

A UV-vis Specord 50 instrument was used to collect spectra of 0.1 $mg.ml^{-1}$ samples dispersed in ethanol by sonication, in the 200-1000 nm range. Cuvettes of 1 cm width were used.

3.3.7 Ultraviolet Photoelectron Spectroscopy (UPS)

The working principle of UPS is similar to that of XPS, however here the sample is irradiated with ultraviolet light from a helium-I source instead of X-rays. Ultraviolet photons have less energy than X-rays, and so less tightly bound electrons are ejected compared to XPS. The resulting photoelectrons give information about the valence band, in particular about the band structure below the Fermi level. It also allows the determination of the work function, the minimum energy needed to excite an electron to the vacuum energy to become a free electron. The work function is determined by

$$\Phi = h\nu - BE_{max}$$

Where Φ is the work function, hv is the photon energy, and BE_{max} is the secondary electron cutoff, the binding energy of the lowest energy photoelectrons detected. BE_{max} is also equivalent to the difference in kinetic energy between the fastest and slowest detected photoelectrons. Secondary electrons are photoelectrons that have been inelastically scattered between ejection and detection, causing an apparent spike of low kinetic energy photoelectrons on the UPS spectrum. Binding energy of ejected photoelectrons is determined by

$$BE = E_K - h\nu - V_{Bias}$$

Where E_K is the measured kinetic energy and V_{Bias} is the electric potential applied to the sample to prevent secondary electron buildup on the surface.[102]

3.3.8 Thermogravimetry

Samples in a controlled atmosphere are heated, and any change in its mass is recorded. This method is used to investigate the temperature stability of materials, as well as confirm loadings of metals on combustible supports. TGA was done using a NETZSCH Simultaneous Thermal Analysis Facility, under air and nitrogen atmospheres with flow rate of 20 $ml.min^{-1}$ and heating rate of 10 $K.min^{-1}$.

3.3.9 Surface nitrogen adsorption/desorption

Surface area and porosity were investigated using N_2 adsorption and Brunauer-Emmett-Teller (BET) theory on a Micromeritics Tristar 3000 instrument. This method uses the amount of nitrogen gas adsorbed to the surface and pores of a sample to determine the surface area, pore volume and pore size distribution. BET adsorption theory is an extension of Langmuir adsorption theory, and makes the following assumptions: adsorption is random, adsorption may occur in infinitely many layers, enthalpy of adsorption is greatest on the first layer, and enthalpy of adsorption on subsequent layers is equal to enthalpy of condensation.

3.4 Electrochemistry

3.4.1 Cathode testing

3-electrode tests were done in 1 M KOH for OER, and 0.1 M KOH for ORR to facilitate comparison with literature, as these are the conditions for benchmarking in alkaline electrolyte. Graphitic carbon counter and working electrodes were used. The working electrode was polished before use using a BASi PK-4 polishing kit velvet pad and <0.05 μm nano powder alumina from Aldrich. The pad and powder were wet with ~1 ml distilled water before polishing. An Ag/AgCl (3.0 M internal KCl electrolyte) reference electrode was used with an SP 300 Bio-Logic potentiostat and EC-lab software. Reference electrode calibration was done by measuring the open circuit potential between the reference and a platinum wire electrode in

0.5 M H_2SO_4 while 10% H_2 was bubbled through. Linear sweep voltammetry was done at a scan rate of 10 mV/s and rotation rate of 1600 rpm, unless indicated otherwise. Cyclic voltammetry was done at a scan rate of 50 mV/s for 10 cycles. Catalyst loading was 1.5 $mg.cm^{-2}$ onto a working electrode area of 0.196 cm^2. Catalyst ink preparation had a significant impact on catalyst performance, with the optimum method being identified as a 100% ethanol solvent and overnight stirring, followed by 20 minutes low power sonication at 15 °C. Deviation from this method leads to inhomogeneous ink and rough surface coverage, as well as flaking and peeling of the catalyst layer. Casting onto the working electrode was done dropwise and very slowly, allowing each additional drop to dry completely before adding another. Other methods resulted in cracking of the catalyst layer and could not give reproducible results. The working electrode was polished using alumina-water slurry on a cloth pad, washed with water and dried prior to casting. Potentials were converted to reversible hydrogen (RHE) electrode values using;

$$E_{RHE} = E_{Ag/AgCl} + E^0_{Ag/AgCl} + 0.059 \cdot pH$$

Where E_{RHE} is the potential vs the RHE, $E_{Ag/AgCl}$ is the measured potential, $E^0_{Ag/AgCl}$ is the potential of the Ag/AgCl vs RHE, and the pH is of the KOH electrolyte. $E^0_{Ag/AgCl}$ was found to be 0.21 V.

3-electrode tests are useful for benchmarking an electrocatalyst for a variety of processes without needing to build a prototype, and to investigate processes with more control than in a device.

Cyclic voltammetry (CV) is performed by slowly cycling potential between a minimum and maximum, and measuring current at set time intervals. This gives information of redox processes happening on the surface, as well as whether these are reversable processes. The

results are presented here according to IUPAC convention, with potential increasing from left to right. Traditional CV studies are poorly suited to the irreversible, multi-phased OER/ORR reaction. The useful information is limited to the magnitude of the ORR peak for different catalyst compositions and loadings, and to some qualitative investigation of changes in the catalyst's metal oxidation states.[103] Narrower CV voltage ranges in a voltage region with no redox activity can be used to investigate the double layer capacitance, which can be calculated as

$$C_{dl} = \frac{j_a - j_c}{2v}$$

Where j_a and j_c are the anodic and cathodic current densities respectively, and v is the scan rate in $V.s^{-1}$. Using an approximate specific areal surface area C_s, it is then possible to estimate the electrochemically active surface area as ECSA= C_{dl}/C_s. The approximate surface are in alkaline solution is taken as 0.022 $mF.cm^{-2}$, though significant variation is possible.[104,105]

Linear sweep voltammetry is done by slowly ramping potential higher or lower and measuring current at set time intervals. This technique is useful for benchmarking different materials and reaction conditions by comparing onset potentials and maximum currents achieved. The main analytical use of the technique is the examination of the kinetics and mechanisms of reactions using the tools like the Koutecký-Levich equation or Tafel equation.

The Koutecký-Levich equation allows one to investigate the contributions of the kinetic and mass transport currents. In its simplest form it is expressed as

$$i_m = \frac{I_K + I_{MT}}{I_K I_{MT}}$$

Where i_m is the measured current, I_K is the kinetic current, and I_{MT} is the mass transport current. The kinetic current is modelled by the Butler-Volmer equation and is potential dependent, while the mass transport current is modelled by the Levich equation:

$$I_{MT} = 0.62nFAD^{2/3}v^{-1/6}C\omega^{1/2}$$

Here, the Levich current is determined by the number of electrons transferred in the half reaction n, the Faraday constant F (96485 $C.mol^{-1}$), electrode area A (0.196 cm^2), diffusion coefficient D ($1.9 * 10^{-5}$ $cm^2.s^{-1}$), kinematic viscosity v ($1.0 * 10^{-2}$ $cm^2.s^{-1}$), angular rotation rate of the electrode ω, and the concentration of the analyte C ($1.2 * 10^{-6}$ $mol.cm^{-3}$ O_2). D and v must be experimentally determined for the electrolyte and temperature of interest, which is why standard electrolytes at room temperature are useful. $0.62nFAD^{2/3}v^{-1/6}C$ is often abbreviated as B_L, the Levich constant.

What is generally of interest in an electrocatalytic investigation is n, as this will help inform the mechanism and rate limiting step of the reaction. In OER and ORR investigations, knowing whether n=2 or n=4 is important, as the n=2 pathway is inefficient and produces peroxide by product which can damage device components.

By writing the Koutecký-Levich equation in the form $\frac{1}{i_m} = \frac{1}{I_K} + \frac{1}{B_L\omega^{1/2}} = \frac{1}{I_K} + \frac{\omega^{-1/2}}{B_L}$ a strategy for determining n becomes obvious: A graph of current against the inverse root of the rotation rate (in radians) will have a slope of $1/B_L$, and n can then be determined by rearranging the Levich equation:

$$n = \frac{B_L}{0.62FAD^{2/3}v^{-1/6}C}$$

The Tafel equation applies in situations where the mass transport is faster than the kinetic current and absolute overpotential is large, allowing for simplification of the Butler-Volmer equation.

Butler-Volmer equation: $j = j_0 \left(e^{\frac{\alpha_a nF\eta}{RT}} - e^{-\frac{\alpha_c nF\eta}{RT}} \right)$

Tafel Equation: $\eta = A \cdot log \frac{j}{j_0}$

The current density j depends on the exchange current density j_0, the overpotential η, the anodic and cathodic charge transfer coefficients α_a and α_c respectively, and the number of electrons transferred n. When absolute overpotential is very large, one term of the Butler-Volmer equation tends to 0 and we simplify to the Tafel equation. Practically, overpotential is plotted against log of the current density to produce a Tafel plot. In the linear region of the Tafel plot the slope is equal to A, the Tafel slope, which is reported in volts per decade ($V.dec^{-1}$). This is essentially a measure of the sensitivity of the current to changes in overpotential, with a lower Tafel slope indicating a greater sensitivity, and hence more energy sensitivity: A catalyst system with a higher Tafel slope will require greater potential difference to increase current response, and therefore will be less energy efficient. In this study Tafel slope data is obtained from LSV experiments with a rotation rate of 1600 rpm, as the linear Tafel slope region of both static and dynamic conditions give identical values.[106]

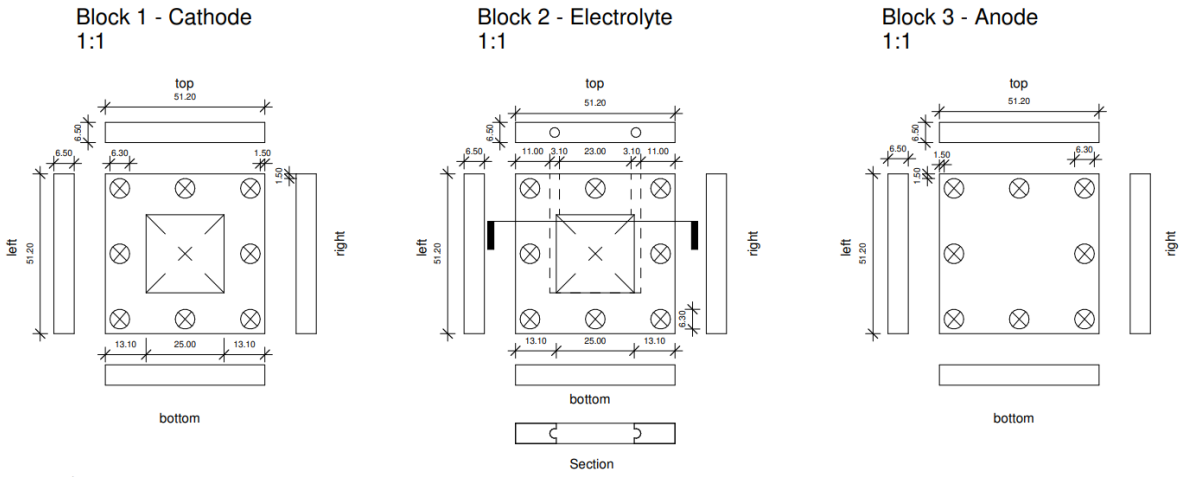
Electronic impedance spectroscopy (EIS) measures resistance, capacitance and inductance elements in a system. The method requires tracking real and complex impedance over a range of alternating current frequencies, where impedance is analogous to electrical resistance as the property of opposing the flow of current. Resistive elements will impede current no matter the frequency, capacitive elements will increase real impedance at low frequencies, and inductive elements will increase impedance at high frequencies. An equivalent circuit must then be chosen to model the EIS data, and the parameters of the circuit are then refined until the circuit's

theoretical EIS spectrum matches the experimental data. 3-electrode catalyst systems will typically fit a relatively simple circuit, with a resistor to model mass transport resistance, and then a parallel resistor and capacitor to model the charge transfer resistance and capacitance respectively.

The potential and magnitude of the alternating current must be chosen to approximate a linear current response to potential in the range of the experiment. The frequency range is from 10^{-1} to 10^{5} Hz.

3.4.2 RZAB testing

2-electrode tests were done using a custom test cell composed of 3d printed blocks, as detailed in the diagram below. A solution of 6 M KOH and 0.02 M zinc acetate was used as the electrolyte, zinc plate as the anode, and carbon paper as the cathode. Both electrodes were encased in Teflon sleeves, with only the appropriate areas detailed exposed. Both electrode exposed surface areas were 2.5 cm^2, while the surface area exposed to the atmosphere was 0.25 cm^2. Cathode catalyst loading was 4 $mg.cm^{-2}$. Current collectors were 1 cm wide copper strips, also connected to a VSP 300 Bio-Logic potentiostat.



Chronopotentiometry was used to simulate the charge-discharge lifecycle of the battery. In these experiments voltage is varied to satisfy set current requirements, which vary over time. Long term tests were done at 0.5 $mA.cm^{-2}$ current density and 30 minutes charge and 30 minutes discharge – this means that the voltage was controlled to sustain a current of + 0.5 $mA.cm^{-2}$ for 30 minutes, and then -0.5 $mA.cm^{-2}$ for the next 30 minutes, and so on . The potential was recorded every 10 seconds, giving information about the voltage the cell can provide during discharge and the overpotential required to charge it. These short cycle tests are mostly for benchmarking against other catalysts in literature, although their value in analysing real systems is dubious. Longer term tests are more useful, being done at more relevant current density of 2 $mA.cm^{-2}$ with 18-hour charge and discharge cycles. Potential was recorded every 30 seconds to reduce the storage and processing requirements of the experiments which can continue for over 200 hours.

Linear sweep voltammetry from 2 V to 0 V (open circuit potential) was done to benchmark the power density profile of the material. As potential approaches the open circuit, the current increases. The product of potential and current is power: IV=P, as $C.s^{-1}.J.C^{-1} = J.s^{-1} = W$. This allows the construction of a power profile graph, from which the voltage and current that give peak power can be determined.

Electronic impedance spectroscopy serves a similar purpose as in the 3-electrode system: the resistance and capacitance of the system is investigated as well as how these parameters are changed after many hours of chronopotentiometry operation. The open circuit potential is used to maximise the linear range.

Chapter 4: Results and Discussion

4.1 Powder X-Ray Diffraction (PXRD)

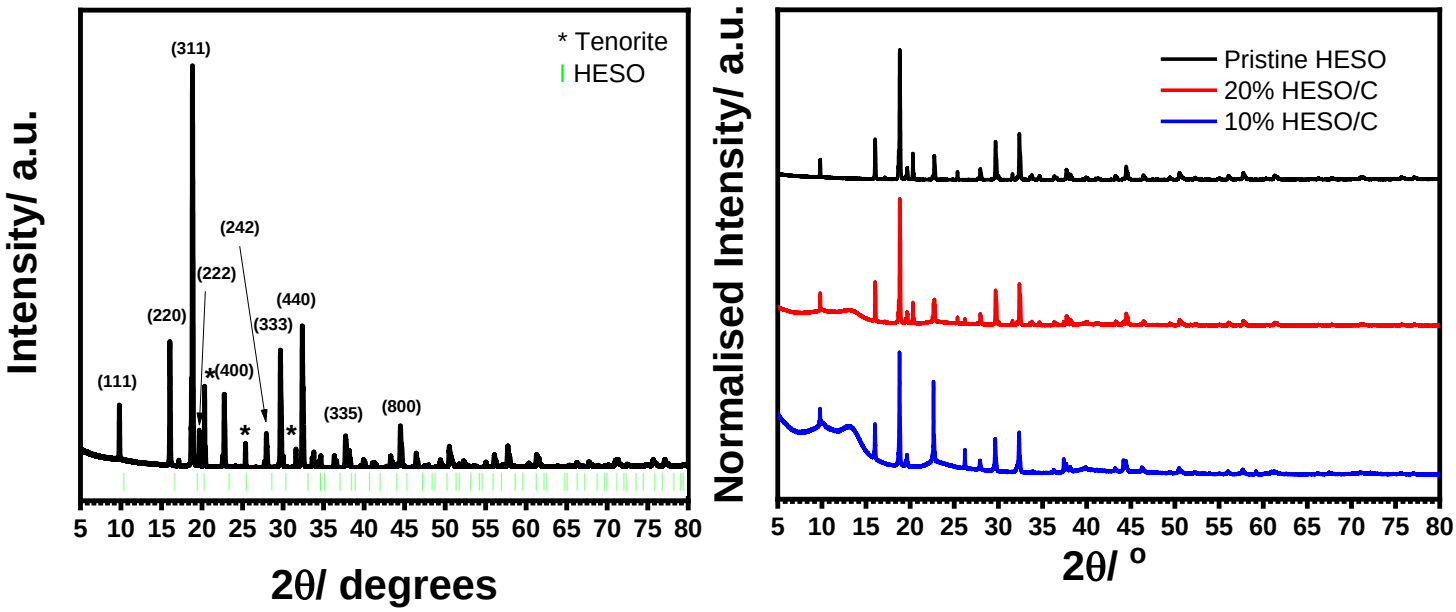


Figure 6: High resolution PXRD of the HESO and composites

The powder X-ray diffraction pattern shows the structure is very similar to simple metal oxide inverse spinel. Several additional peaks may be attributed to NiO, CuO or a combined NiCuO phase forming at grain boundaries,[107] however Rietveld refinement and PDF fittings indicate that only tenorite CuO (13%) and bunsenite NiO (2%) are present as impurities. These species are not expected to have any significant ORR activity, and so their presence is likely to inhibit ORR activity by blocking active HESO sites. CuO has been found to be a moderately effective OER catalyst, with $E_{10} > 1.6$ V vs RHE[108], significantly higher than what will be demonstrated for the HESO. CuO therefore also reduces the effectiveness of OER. NiO is a poor OER catalyst unless doped with iron[109], a situation that is likely in the presence of the HESO particles. The NiO may therefore have a synergistic effect with the HESO. Figure 6 (a) shows the measured PXRD pattern of the HESO above the peaks (green) expected for iron oxide inverse spinel (COD ID 9006189)[110]. The slight misfit of the peaks is caused by the lattice

distortions due to the inclusions of the other four metals within the structure, which all have different sizes with respect to iron[111].

Figure 6 (b) shows the PXRD patterns of the 10 and 20% HESO/C. The PXRD measurements indicated no structural change to the HESO after supporting it on Vulcan carbon. However, it was noticed that the tenorite peaks are supressed relative to the HESO peaks in the composite. It is possible that CuO captured in grain boundaries, as suggested by Wang et. al.[107], was freed when the agglomerated HESO particles were separated. CuO nanoparticles form stable suspensions in the ethylene glycol/water mixture used in the synthesis, and so become separated from the HESO[112]. The removal of this impurity should improve the ORR and OER activity as HESO active sites are no longer blocked.

A custom CIF was made to initiate Rietveld Refinement. Magnetite was used as a template. The lattice positions were randomly occupied by the five metals. Rietveld refinement using TOPAS software V7 was performed using the PXRD data from figure 6 (a). The best fit was found after the symmetry was lowered to P 1 (triclinic) to allow the distortion to be modelled (figure 7). Unit cell parameters were optimised as a = 8.314 Å, b = 8.291 Å, c = 8.322Å, α = 89.784°, β = 90.058°, and γ = 89.801°. The refinement parameters can be found in full in the

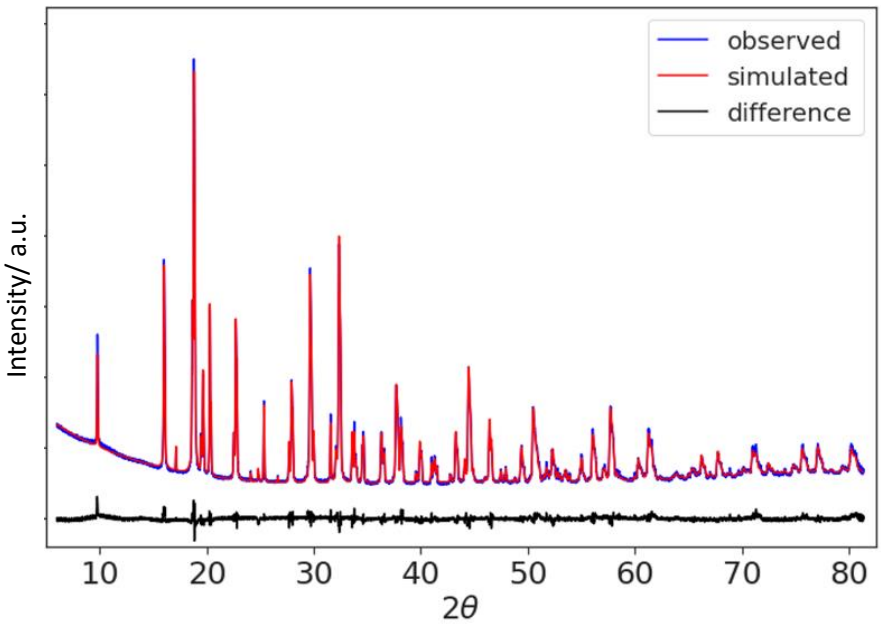


Figure 7: Rietveld Refinement of HESO

supplementary information A1 and A2. As the five metals comprising the HESO are randomly positioned throughout the structure, sublattices can be formed within the structure. Therefore, the overall crystal structure is a convolution of low entropy spinels with differing orientations within the overall structure. This is further investigated via Raman spectroscopy.

4.2 Pair Diffraction Function (PDF)

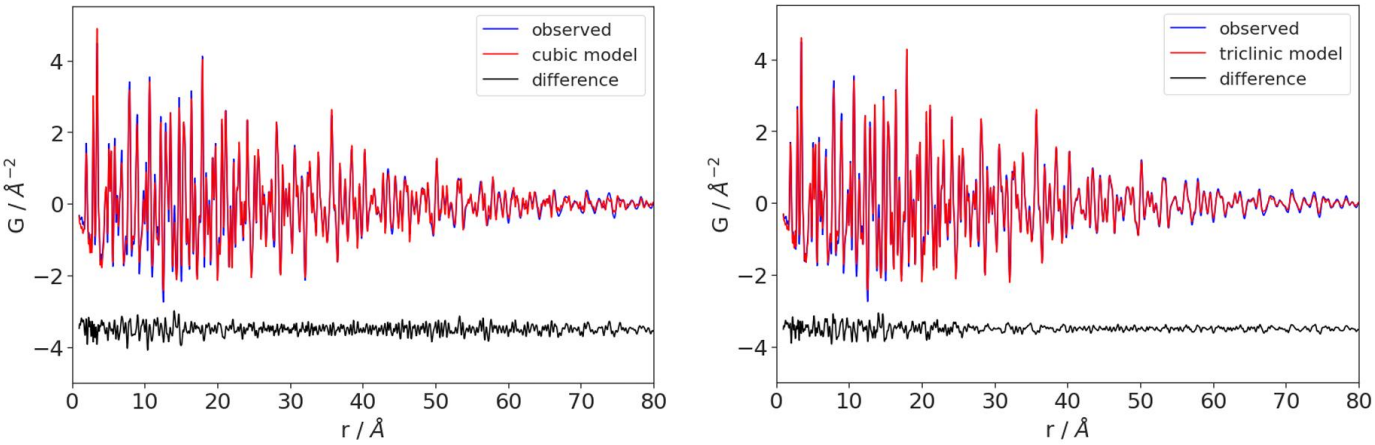
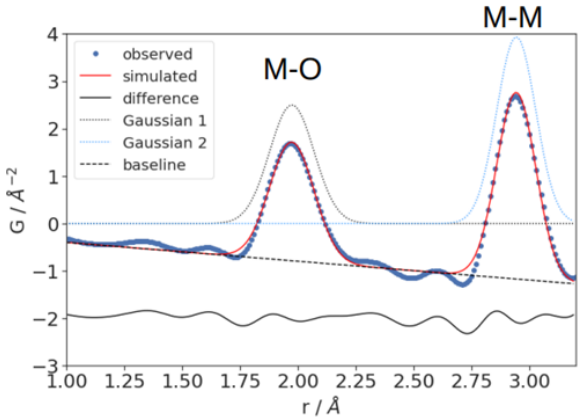


Figure 8: HESO PDF data with cubic and triclinic refinements.

The PDF is shown in figure 8, with the refinements for cubic and triclinic symmetry superimposed. To account for the random distribution of the five metals within the structure, all metal atoms were modelled as cobalt, which has the median atomic number among the five metals. The first two coordination spheres of the PDF are shown in figure 9. They have been assigned to the metal-oxygen bond distance as the shortest distance, and metal-metal distances as the next shortest. It is interesting to note that the metal-oxygen bonds show a wider peak,



M-O:
Mean 1.9787(14) Å
FWHM 0.226(3) Å

M-M:
Mean 2.9451(8) Å
FWHM 0.198(2) Å

Figure 9: PDF of the metal-oxygen and metal-metal bond

indicating greater variation in these bond lengths than in the metal-metal distances. This shows that despite the chemical variation causing a high distribution of M-O bond lengths, the positions of the metal centres do not deviate from the parent spinel structure. Figure 10 shows a series of PDF refinements attempting to fit the data (with lower R_w values indicating better fit). While all six models gave an acceptable fit, it is clear that a simple cubic model is less accurate, and the reality is a lower symmetry system as expected from a high entropy material. Interestingly, the orthorhombic model (in which unit cells have all angles at 90 degrees but all three side lengths different) fits the PDF data most closely. Both the large metal-oxygen bond length distribution and the high accuracy of the orthorhombic system refinement point to the possibility of Jahn-Teller distortions which lengthen or contract metal-oxygen bonds due to orbital degeneracy. The lower variation in metal-metal distances despite this distortion is unusual, as distortion in the M-O bond lengths should similarly distort the M-M bond lengths. There are two immediate possibilities: the Jahn-Teller distortions could be a mix of elongations and contractions, as proposed by Rak et. al. [113] which would partially negate the average effect on metal-metal distances while maintaining a significant metal-oxygen bond length variation. It is also possible that metal-oxygen-metal bond angles are distorted to accommodate the various metal-oxygen bond lengths, causing increased lattice strain in the oxygen lattice.[114] Such strain modifies the electronic band structure, which is one of the primary draws of HEM catalysts. Of particular interest, density of states near the Fermi level may increase, providing more active electrons to participate in the OER/ORR reactions[115]. The reality of the HESO includes the spinel parent structure, the distorted lattice, and the existence of sub lattices, which is why several models produce good fits for the data.

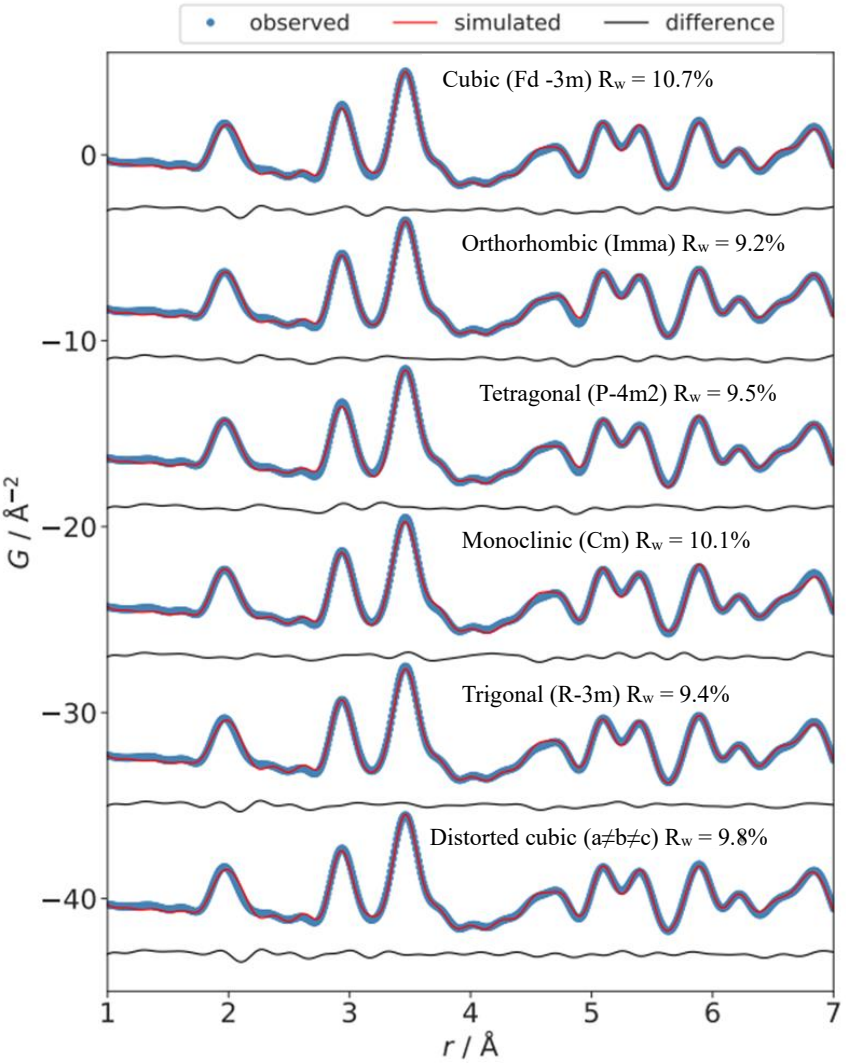


Figure 10: Comparison of PDF refinements of HESO using various crystal systems

4.3 Raman Spectroscopy

A significant increase from 0.9 to 1.2 in the I_d/I_g ratio shown in figure 12 b) on increasing the HESO loading indicates a increasing proportion of sp^3 hybridized carbon. The increasing ratio with increasing HESO loading indicates that the HESO induces defects where it interacts with the carbon during synthesis, leading to strong catalyst-carbon interaction.[96] This would facilitate conduction of electrons between the insulating HESO and conductive carbon, reducing resistance and so improving electrochemical performance. A closer look at the lattice vibrations in figure 12 a) reveals three expected peaks: symmetric A_{1g}, $3F_{2g}$ and E_g peaks are

expected from any spinel.[116] However, in the HESO and HESO/C an interesting split in the A_{1g} peak is observed. In spinels, an A_{1g} peak is associated with the symmetric vibrations of the tetrahedral, MO_4 units as shown in figure 11.

In normal spinels, where the cation has a 2+ charge, it is found around 610 cm^{-1}.[117] In inverse spinels, where the tetrahedral voids in the O^{2-} lattice are occupied by metal III ions, the A_{1g} peak is found around 700 cm^{-1}, because the more highly charged metal attracts the oxygen anions more tightly, and their vibrations are therefore faster than in tetrahedra with a metal II ion.[117] In the HESO, both peaks are present in figure 12 (a), indicating that the structure has mixed oxidation states in the tetrahedral sites. That high entropy spinels can have this "partial inversion" has been observed in chromium-containing analogues of the HESO under investigation here. Comparison between $(CuCoFeMnNi)_3O_4$ and its zinc and chromium containing analogues as shown in table A2.

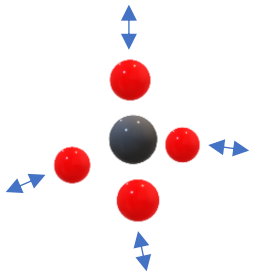


Figure 11: A1g vibration of an MO4 unit

The two A_{1g} peaks are well resolved in this case, since the five metals have similar atomic weights and so the main factor in the Raman shift is the oxidation state of the metals. A direct comparison of the peak areas, the approximation suggested by Modi et. al.[117], reveals an increase in the degree of inversion from 15% to 34% between the HESO and 20% HESO/C. This suggests an increase in oxidation state of the tetrahedral sites, a direct contradiction to the findings in the following XPS and EPR analysis. This change in apparent degree of inversion is likely rather to be due to the separation of the tenorite phase during composite synthesis, as tenorite as an A_g vibration at 630 cm^{-1} that cannot be distinguished from the A_{1g} vibration. The true degree of inversion is therefore >34%, calculated after the removal of tenorite. A higher ratio of more highly oxidised 3+ metal ions in low coordination sites enhances the adsorption

of the electron rich reactants of both the OER and ORR, but limits the desorption of the products. As long as adsorption remains the limiting step, as suggested by the later electrochemistry, a higher degree of inversion is preferred and inversion tuning may be a promising strategy for the design of future HESO catalysts.

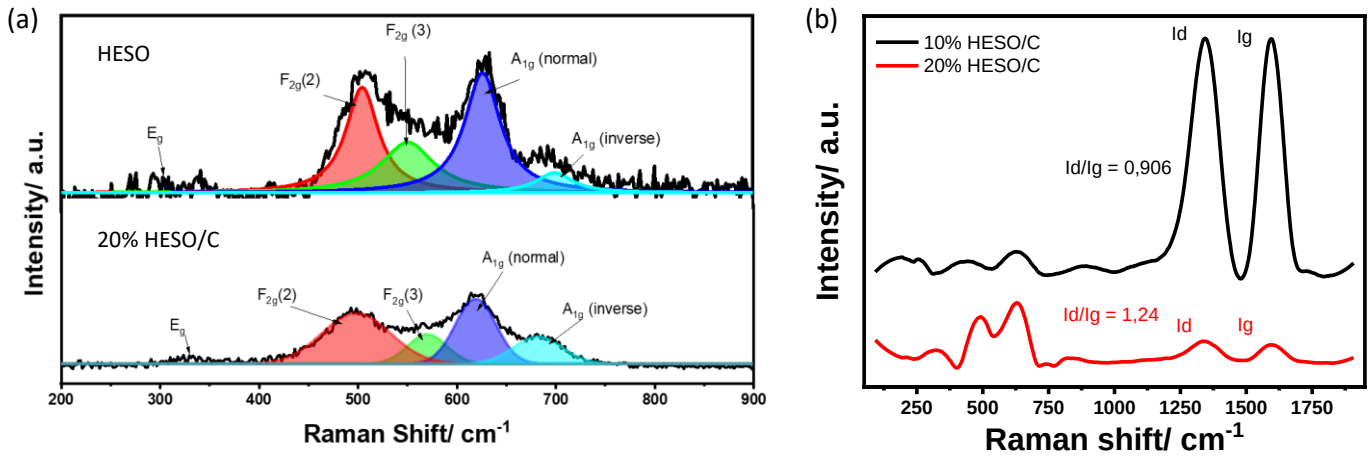


Figure 12: a) Raman Spectra of lattice vibrations. b) Full Raman spectra of 10 and 20 % HESO/C

4.4 Microscopy

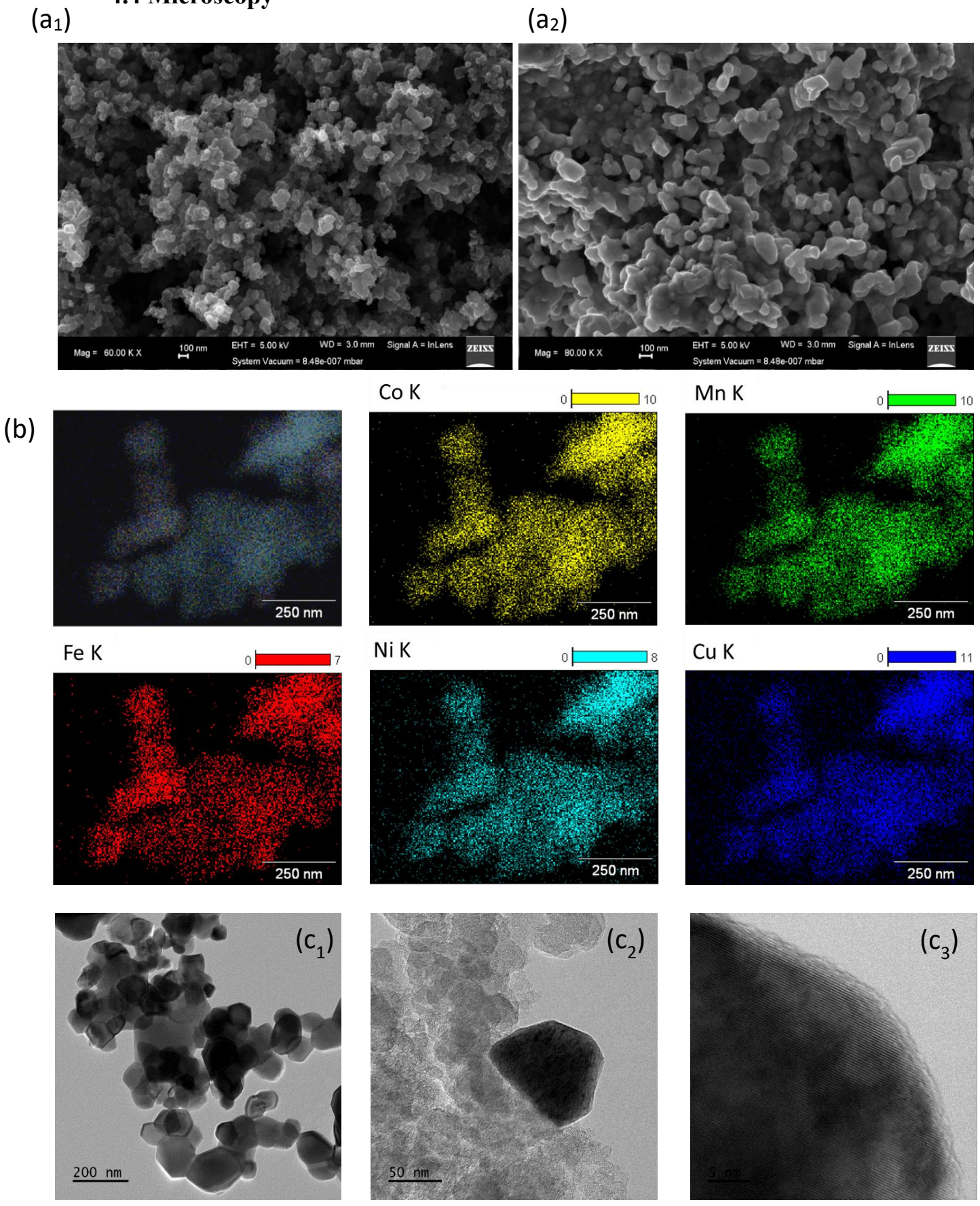


Figure 13: SEM micrographs of (a1) 20% HESO/C and (a2) Pristine HESO. (b) EDS elemental maps of each of the five metals. TEM micrographs of (c1) pristine HESO and (c2, c3) 20% HESO/C

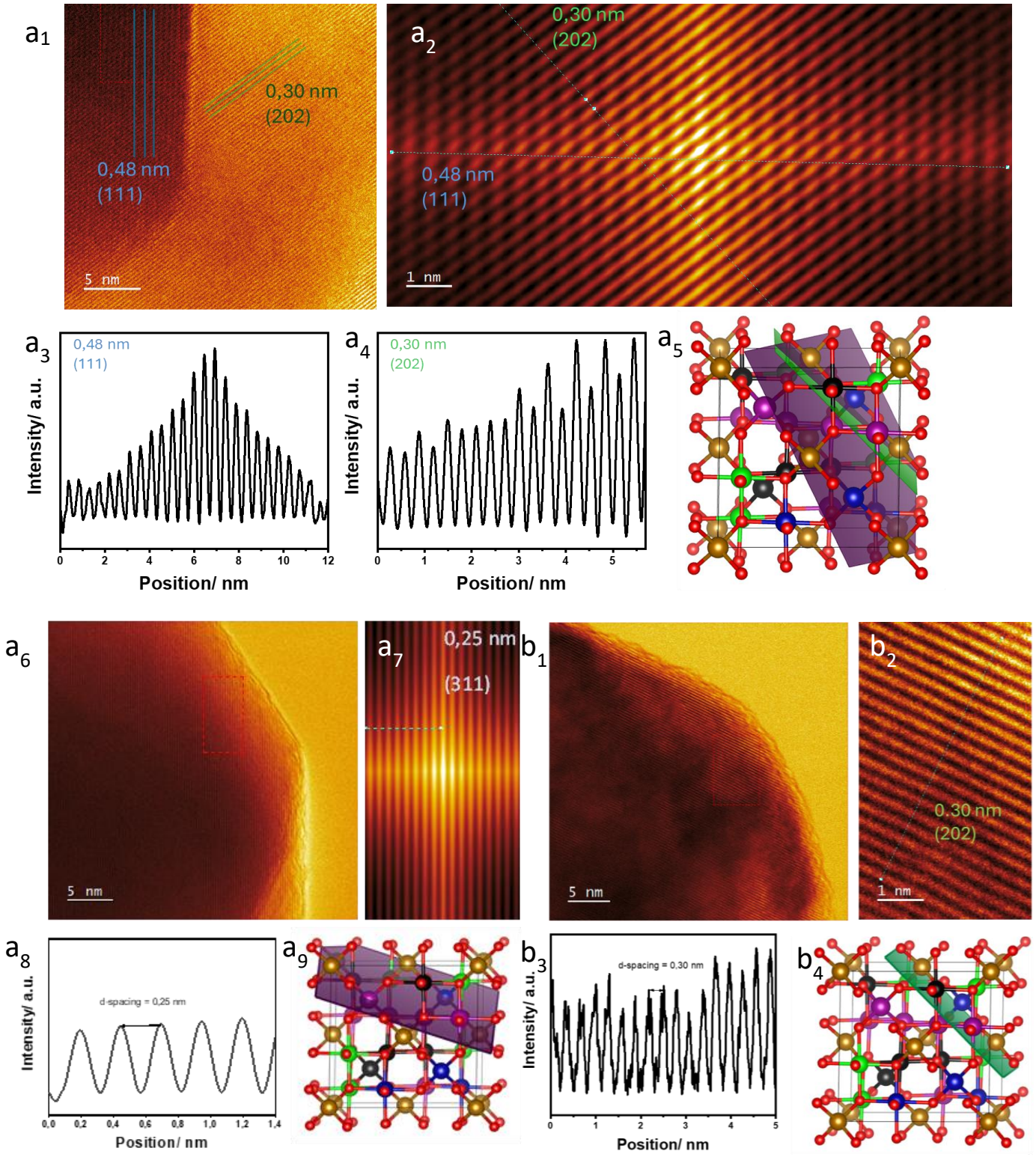


Figure 14: TEM micrographs (a1) Pristine $(CuCoFeMnNi)_3O_4$ (a2) lattice fringes of the pristine HESO (a3) d spacings determined for the (111) plane (a4) d spacings determined for 202 plane (a5) Visualisation of the visible lattice planes. (a6) Micrograph of a particle at a different angle. (a7) FFT and (a8) d-spacing determined. (a9) 311 lattice plane (b1) 20% HESO/C (b2) lattice fringes of composite (b3) d spacings determined for 202 plane in composite (b4) visualistion of the HESO (202) plane

Figure 13 (a) shows that the 20% HESO/C is a porous network distorted hexagonal particles, though distinction between HESO and carbon is difficult. In figure 13 (b) these particles in the pristine HESO are clearly agglomerated. This is evidence that composite synthesis broke up the agglomerates of HESO particles and stabilised them in the carbon, exposing more surface area for electrocatalysis.

Elemental mapping shown in figure 13 (b) shows that the concentrations of metals are strongly associated with one another, which supports the formation of a single high entropy phase.[89]

Transmission electron microscopy shown in figure 13 (c) reveals that the HESO nanoparticles are indeed distorted hexagons. Figure 13 (c_1) shows agglomerated hexagonal nanoparticles ranging in size from 50 to over 100 nm. Figure 13 (c_2) shows the HESO nanoparticle (black) in the carbon network (grey), making intimate contact as suspected from Raman spectroscopy. The HESO particles in the carbon network are found alone, showing that the agglomeration seen in the pristine HESO has broken up. In figure 13 (c_3) a regular crystal lattice plane is visible toward the centre of the nanoparticle, while the edges are jagged, demonstrating the high concentration of surface defects and high surface area associated with high entropy particles.[23,68,99]

Figure 14 shows high resolution TEM, and clear evidence of two lattice planes with d spacings of 0.30 nm and 0.48 nm. 0.48 nm corresponds to the spacing of the (111) plane in both the ordinary inverse spinels and the HESO. However, ordinary spinels should not show a spacing of 0.30 nm, and this is only seen in the (202) plane of the refined HESO structure. The calculated D spacings for some significant HESO planes can be found in the Supplementary table A2. This is further evidence that the synthesized particles have a distorted lattice, and supports the findings of the Rietveld refinements.[118]

4.5 X-ray Photoelectron Spectroscopy (XPS)

The deconvoluted XPS spectra are shown in figure 16. Iron, cobalt and nickel appear to be distributed mainly between the II and III oxidation states. This indicates that these metals at least are found in both the A and B spinel sites.[117] Copper mostly as Cu^{2+}. In a partially inverse spinel, this implies that copper occupies both the octahedral and tetrahedral sites and so should undergo Jahn-teller distortion[107,113]. It has been proposed that this could contribute to the formation of a separate copper oxide phase, as seen from the PXRD.[107] Similarly, Jahn Teller distortion of tetrahedrally coordinated Ni^{2+} could explain the formation of the minority Bunsenite phase. However, high entropy materials are already characterised by a distorted lattice. Rák, Maria & Brenner found that in high entropy systems, Cu^{2+} octahedra undergo both Jahn-Teller elongation and the less common Jahn-Teller compression, thereby accommodating the preferred bond lengths of the other metal octahedra.[113] Additionally, high spin Mn^{3+} in an octahedral arrangement also undergoes significant Jahn-Teller distortion,[119] due to degeneracy in the bonding orbitals, but shows no evidence of forming separate phases. Jahn-Teller distortion alone is therefore not a comprehensive explanation for the partial copper and nickel oxide segregation. Nickel and copper ions are the smallest of the metals used, and so it is possible that they may continue to migrate during annealing despite the slow diffusion effect. Reducing the percentage of copper in particular, or excluding copper entirely in favour of other metals, may be needed to avoid the formation of additional phases.[107]

Manganese is found in the II and III oxidation states, indicating a split between octahedral and tetrahedral sites as with iron, cobalt and nickel, but also to a significant extent in oxidation state IV. In the spinel structure, this is accompanied by the conversion of some Cu II to Cu I, as is the case in I-IV spinels. As XPS is a surface technique, it is expected that Mn IV and Cu I form due to the distortion and defects at the surface of the HESO. Gorlan et. al. found that bifunctional manganese oxides undergo structure conversions as operating voltage varies

between ORR and OER operating ranges, with a disordered spinel-like structure of Mn (II) and (III) under ORR conditions and a Birnessite structure of Mn (III) and (IV) under OER conditions.[11]

The slow diffusion effect should prohibit any such reorganisation in the HESO, however the presence of all three manganese oxidation states on the HESO surface lends weight to the hypothesis that the highly disordered and defect rich HESO nanoparticles provide a variety of active sites, with some being more suited for either OER or for ORR. The tenfold increase in the relative area of the Mn (IV) peak in the composite is caused by the breaking apart of the agglomerated particles, exposing more surface area and removing interfering CuO and NiO impurities.

Similarly, NiOOH formation on HESO surfaces as indicated on the XPS is a species often associated with OER catalysis.[120,121]

Due to the disorder intrinsic to the HESO, oxygen defects are expected. XPS was further used to examine the oxygen O1s peak, shown in figure 16. The formation of the composite is associated with a significant increase in the O^- and covalent oxygen C-O peak, as expected due to the inclusion of Vulcan carbon.[122] The increased M-OH peak may also be due to the exposure of additional surface area. While the O^- peak is often use as an indicator of oxygen defect concentration,[123] the confounding factor of the Vulcan carbon means that it would be reckless to conclude on oxygen defects using XPS alone. EPR was used to confirm that the composites have a greater oxygen defect concentration.

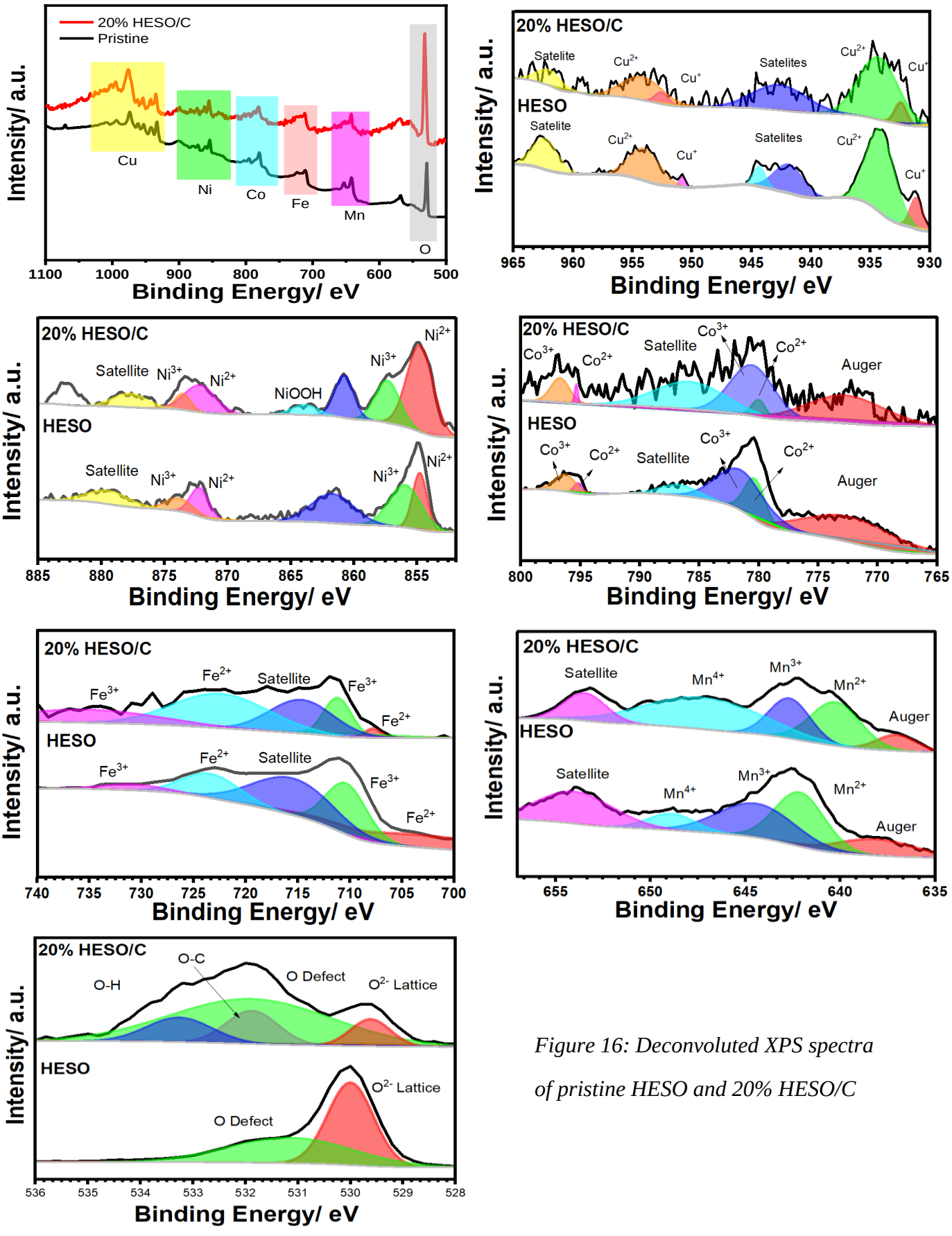


Figure 16: Deconvoluted XPS spectra of pristine HESO and 20% HESO/C

4.6 Electron paramagnetic resonance (EPR)

Figure 17 shows the EPR spectra of the HESO and composites, normalised by HESO content as the Vulcan carbon signal, expected at lower g and with significant anisotropy, was too faint and was not detected.[124,125] The data as collected is shown in figure 17, and it is clear that the signal intensity is dominated by HESO concentration and any information on the actual structure is overwhelmed until normalisation is performed as shown in figure 18. Figure 18 shows a dramatic increase in signal intensity upon composite formation, but no difference in normalised intensity between the 10 and 20% composites. This is evidence that the composite synthesis stabilises smaller particles as observed in the TEM in figure 13 (c_2), exposing greater surface area than the pristine HESO and so more surface defects. Of further interest in the EPR spectra is the downfield shift with increasing carbon content, indicating that the HESO has a

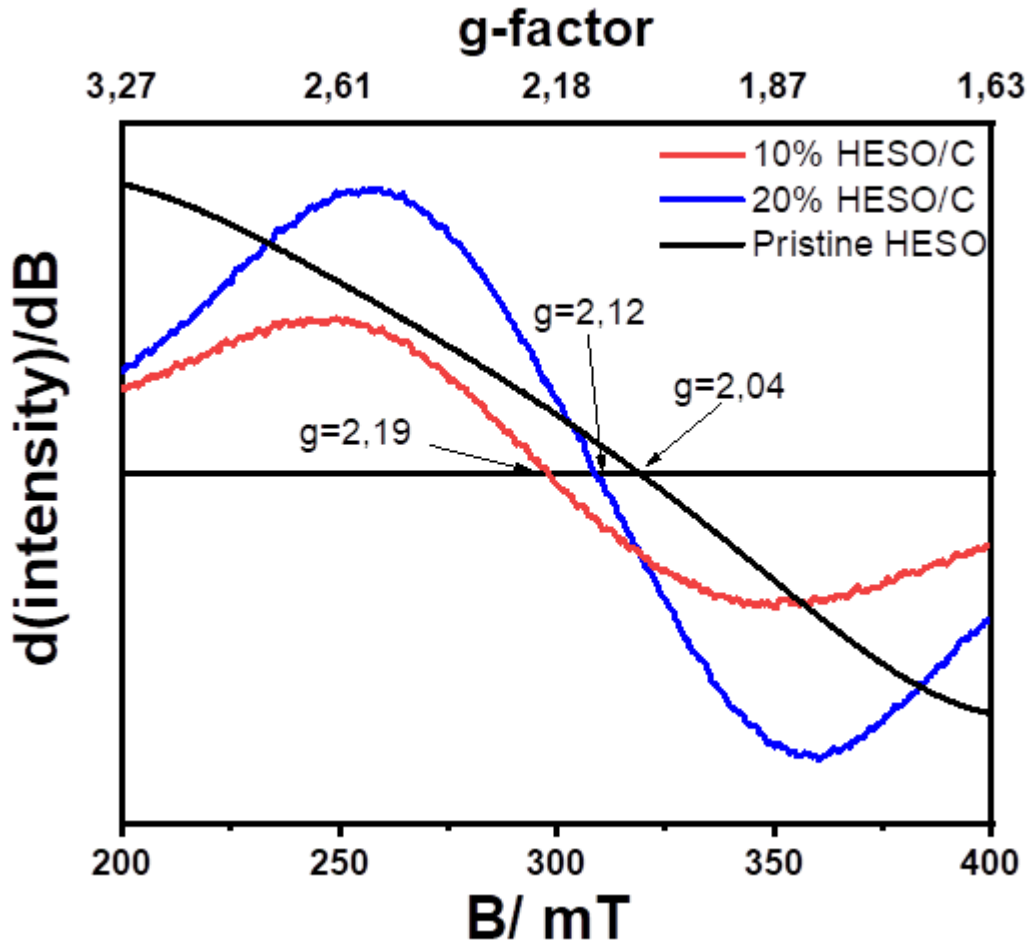


Figure 17: EPR spectra of the HESO and composites

magnetic shielding on paramagnetic species. This effect together with the broadness of the peaks is evidence for ferromagnetic behaviour in the HESO[126], in line with the properties of the spinel oxides. The lack of significant asymmetry in the EPR spectra indicates a lack of magnetic anisotropy due to a cubic crystal phase, supporting the structure refinement results.[127] The total lack of fine structure in the spectra may be due to the many chemical environments causing broad, overlapping lines,[128] combined with an exchange narrowing effect as spin relaxation in the highly disordered HESO is fast relative to hyperfine coupling effects.[129,130] It is also likely that unpaired spins are delocalised throughout the structure, resulting in an EPR signal that is the average of the environments in the structure. This is seen in materials where polaron hopping is the dominant conduction model, as will be elaborated on in the following UV-VIS analysis.[130,131]

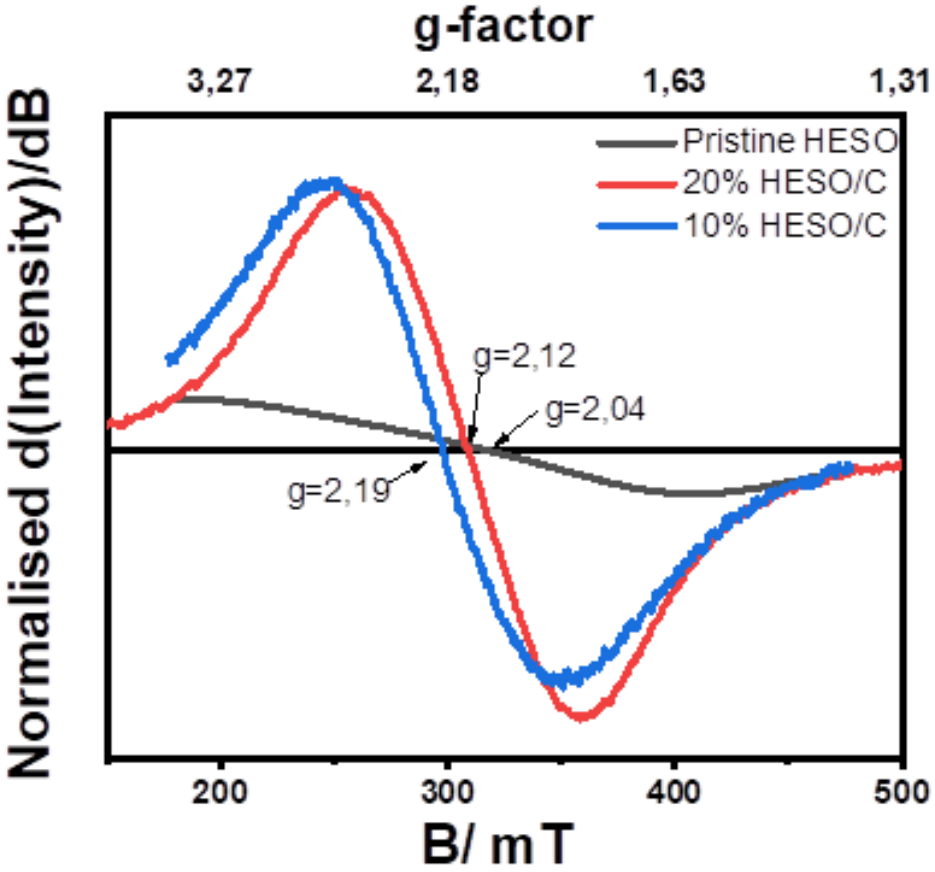


Figure 18: Normalised EPR Spectra of the HESO and composites

4.7 Ultraviolet Photoelectron Spectroscopy (UPS) and UV-VIS Spectroscopy

Ultraviolet photoelectron spectroscopy (UPS) measurements are shown in figure 19. Both the 10 and 20% composites show a flattening near the Fermi level. This is expected, as carbon increases electron conductivity and so more states in the valence band must be available. A small decrease in work function as the carbon content is increased simply shows the improvement in conductivity associated with the carbon support.

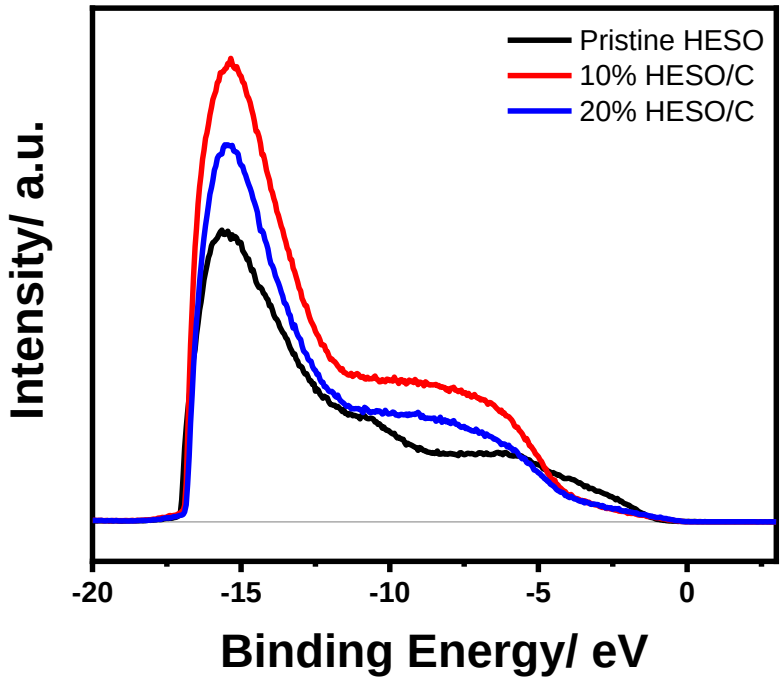


Figure 19: UPS spectra of HESO and composites

Table 3: UPS parameters for HESO and composites

	BE min/ eV	BE max/ eV	W/ eV
Pristine HESO	-0,7	-17,1	4,8
10% HESO/C	-0,2	-17,0	4,4
20% HESO/C	-0,2	-16,9	4,5

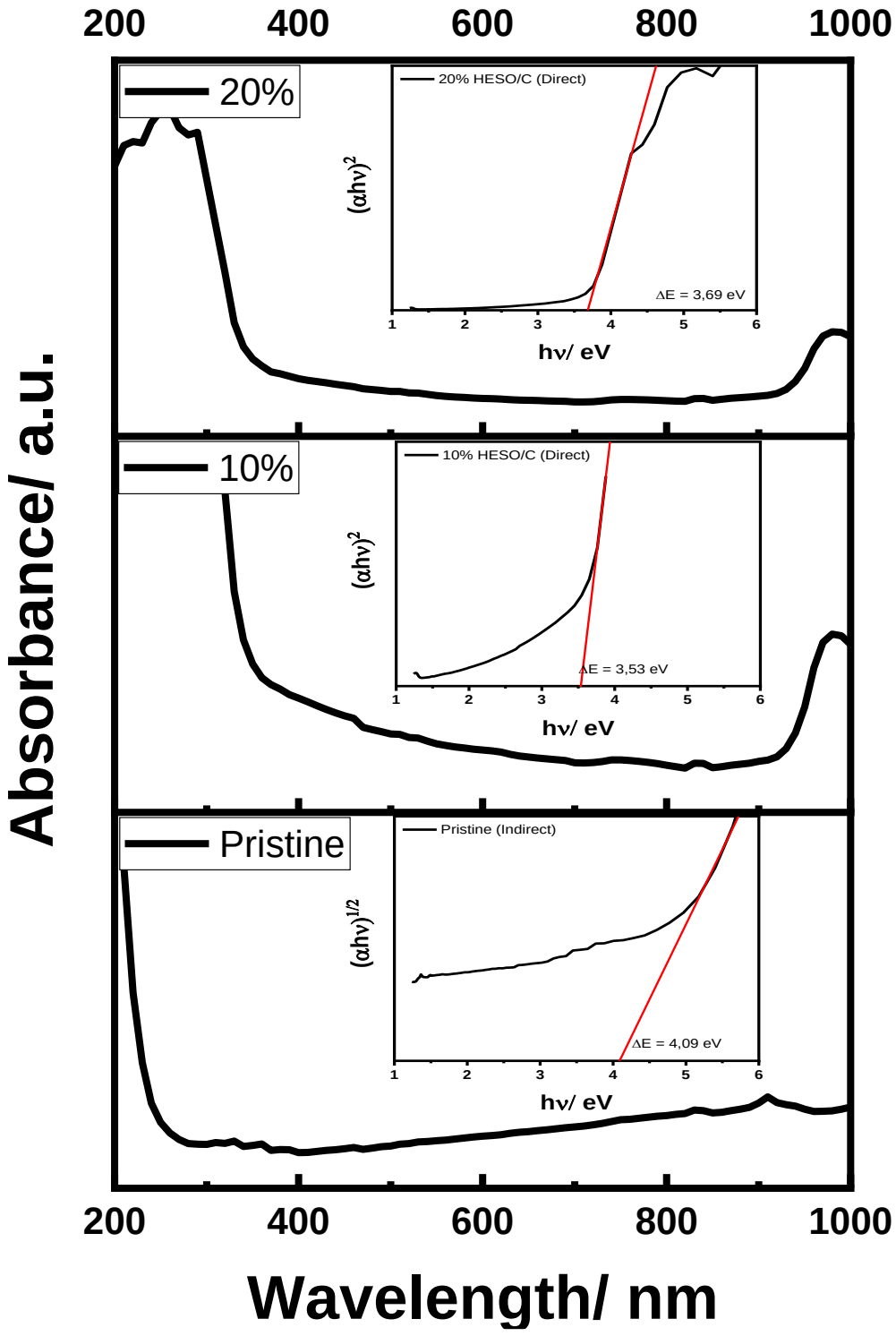


Figure 20: UV-VIS and Tauc plots of the HESO and composites

The Tauc plot in figure 20 shows that the pristine HESO acts as a semiconductor with a moderate band gap of 4.1 eV. The band gap of the pristine material is higher than that of mono- and bimetallic spinels, which have optical bandgaps between 1 and 3 eV although optical

bandgap determination of spinel oxides is somewhat controversial.[132] The diversity in the electronic environments of a high entropy material can provide a wider range of energy levels, both lower conduction band energies and higher energy valence band energies, but this is not seen in this material.[132,133] It is therefore further evidence that conduction proceeds via a polaron-hopping mechanism, where electrons must "hop" from cation to cation, creating a propagating polaron- an electron with an associated phonon as the lattice is distorted by the slow-moving charge. This process is impeded when the donating and receiving cations are of different elements[79,80,134], but due to the high disorder in the HESO it is unlikely that electrons can find uninterrupted chains of like-cations. This situation is imperfectly modelled currently, and so it is difficult to propose strategies to enhance electron conductivity within the HESO.[79] The use of conductive supports is therefore essential to improve electrical conductivity.

4.8 Thermogravimetric Analysis

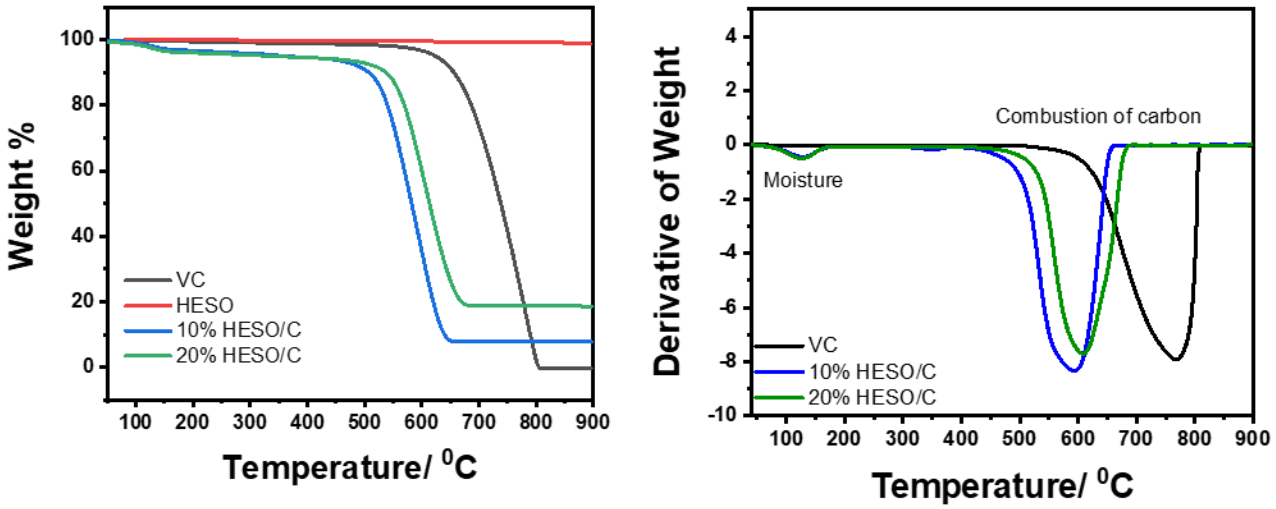


Figure 21: TGA of 10 and 20% HESO/C under a) nitrogen and b) air

Figure 21 shows the TGA of Vulcan carbon, pristine HESO, 10%, and 20% HESO/C under an air atmosphere. The HESO shows no mass changes, while the 10 and 20% HESO/C lose 90 and 80% of their mass, respectively, as expected. This serves simply to confirm the mass loadings of the HESO/C. The combustion of carbon occurs at a lower temperature in the HESO/C than in pure Vulcan carbon, as the HESO catalyses the reaction.

4.9 Surface Area and Pore Analysis

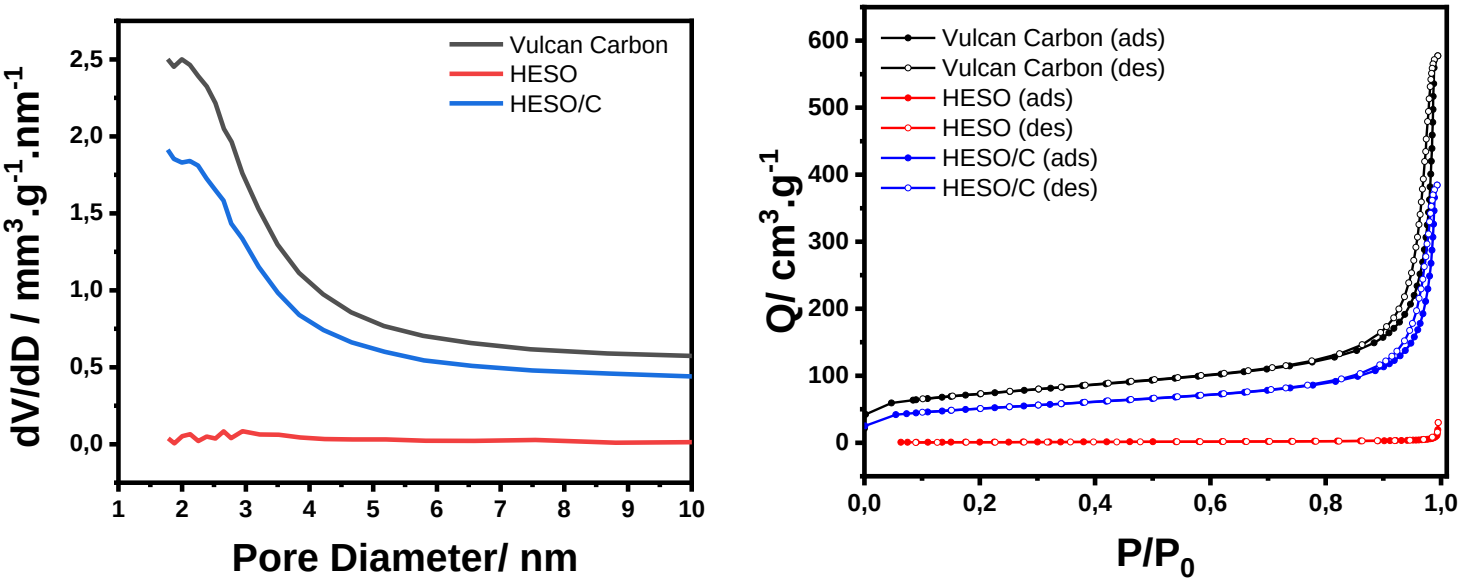


Figure 22: Pore size distribution (a) and BET adsorption-desorption curves (b) for Vulcan carbon, pristine HESO and 20% HESO/C composite

N_2 physisorption after degassing at 300 °C is shown in figure 22, with the BET calculated parameters shown in table 5. The HESO has very low pore volume and surface area, while the Vulcan carbon has a relatively high specific surface area and pore volume. The composite's surface area and pore volume are a linear combination of the carbon's and pristine HESO's, and so it seems that the interaction between HESO and carbon has not had any effect on the porosity of the components.

Table 4: BET derived values.

	Surface area/ $m^2.g^{-1}$	**Pore volume/ $cm^3.g^{-1}$**	**Isotherm/ IUPAC convention**
Vulcan Carbon	269,07	0,35	Type IV
Pristine HESO	3,39	0,0058	Type III
20% HESO/C	181,96	0,25	Type IV

4.10 Three Electrode Electrochemistry

Figure 23 (a-c) shows the cyclic voltammograms taken at 50 $mV.s^{-1}$ under oxygen and nitrogen atmospheres. The current response of the pristine oxide is poor due to its low conductivity. Supporting 10% HESO on Vulcan carbon improved current response and increasing loading to 20% increased it further. The high entropy nature of the metal oxide, as well as the fact that pH may vary close to the electrode surface as hydroxide is consumed or produced,[135] makes assigning these peaks somewhat challenging, as there are several redox processes that could occur within this voltage range. Three oxidation peaks are of interest: a small peak at 0.55 V, a strong peak at 0.77 V, and a shoulder to this peak at 0.69 V that is difficult to distinguish: it is visible in figure 23 b) but not figure 23 c) or a). Manganese redox reactions could be responsible: in Mn II/III spinels, Mn_3O_4 is converted to Mn_2O_3 around 0.55V, and then further to MnO_2 around 0.80 V[136]. In the HESO, this corresponds to increasing Mn oxidation state from II to III to IV without lattice rearrangement, due to the slow diffusion effect. As seen from XPS, Mn is found in all three oxidation states at the HESO surface. The relative amounts of these three Mn oxidation states may depend on the applied potential, and so oxygen lattice strain would depend on the potential as well. Operando PDF and EXAFS experiments would be required to investigate this, and may give valuable insight into the roles of lattice strain under the different operating potentials of an OER/ORR catalyst.

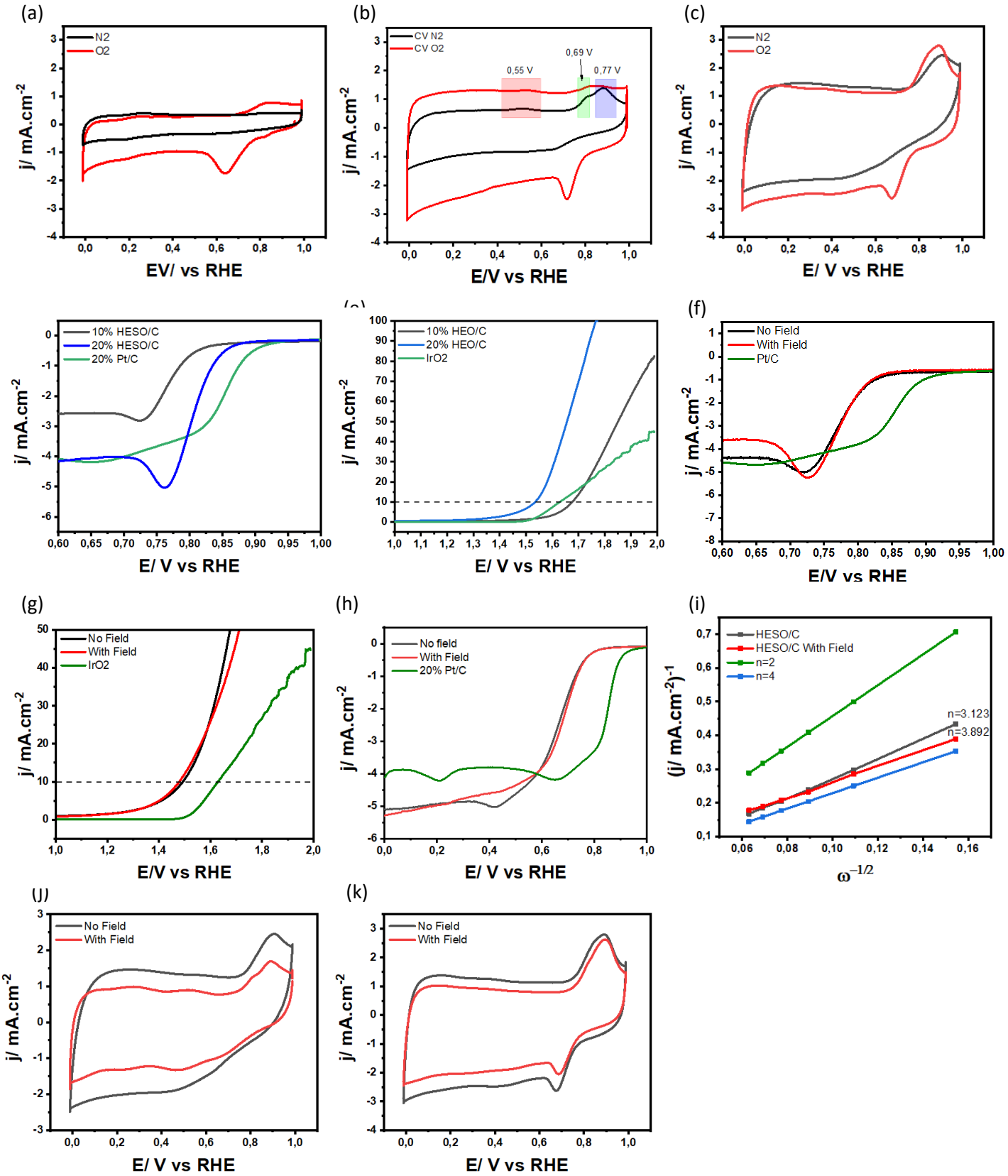


Figure 23: Cyclic voltammetry of (a) pristine HESO, (b) 10% HESO/C, and (c) 20% HESO/C. Only the 5th cycles are shown. (d) ORR and (e) OER polarisation curve for the intrinsic catalyst at various loadings, at 1600 RPM in 1 M KOH. (f) ORR and (g) OER polarisation curves for the 20% HESO/C in 1 M KOH at 1600 RPM, with and without an applied field. (h) ORR polarisation curves for the 20% HESO/C in 0.1 M KOH at 1600 RPM, with and without an external field applied. (i) Koutêcky-Levich plots for the 20% HESO/C compared to theoretical electron numbers. CV of 20% HESO/C with and without the field, under nitrogen (j) and oxygen (k) atmospheres.

Figure 23 (d-e) shows the polarization curves for the ORR and OER processes. The onset potential for the OER decreases with HESO loading, down to a loading of 20%. At this optimal loading, it is seen that the potential at 10 $mA.cm^{-2}$ is 1.534 V, 94 mV earlier than the 1.630 V of commercial IrO_2 under the same experimental conditions. It is quite extraordinary that the HESO, even supported on the primitive carbon material, can outperform the commercial catalyst. It must be noted that this HESO outperforms analogous spinel iron and cobalt oxides[29]. Unlike tests done on such spinel oxides reported by Ren et. al. the application of a magnetic field did not obviously improve the OER performance. This may well be due to the testing using a rotating disk electrode: the constantly changing magnetic field as the electrode surface rotates may not allow the spin alignment necessary for the enhancement of charge transfer.

However, results reported by Yan et. al indicate that their cobalt nanodots on electro spun carbon nanofibers do show magnetic OER enhancement under identical experimental conditions. It is possible that the amorphous Vulcan carbon support is to blame for the lack of magnetic enhancement. To examine this possibility, the HESO was supported on onion-like carbon (OLC) by the same method listed above, only with OLC instead of Vulcan carbon. Onion-like carbon is more crystalline as compared to the amorphous Vulcan carbon, and is more conductive and less prone to agglomeration.[137] The results are shown in figure 23 (g), and indeed it can be seen that the application of the magnetic field reduced the OER onset potential by 15 mV. An explanation is that the more ordered carbon allows the circulation of electrons setting up magnetic field to oppose the changing external field by Lenz's law. This opposing magnetic field causes the spin alignment and facilitates charge transport. If this is indeed the reason, then such expensive nanostructured carbons are not necessary in full-cell zinc-air batteries, where the magnetic field would be static as opposed to the dynamic conditions of the rotating disk electrode.

The curve for the ORR shown in figure 23 (d) is less impressive, with the catalyst achieving $E_{1/2}$ only at 0.760 V as compared to 0.852 V for commercial 20% Pt/C. This result is moderate among the current research on ORR catalysts, which typically achieve a half wave potential between 0.7 and 0.9 V.

The magnetic field produced mild change in the ORR profile in figure 23 (f). The polarisation curves for ORR at 0.1 M KOH, a more optimal electrolyte for ORR[138], are shown in figure 23 (h). The application of the magnetic field under these conditions led to a slight increase in the half wave potential of 15 mV, consistent with the enhancement reported by Yan et. al.[30] The better ORR conditions may simply allow greater sensitivity to the small changes observed when a magnetic field is applied.

Further investigation into the small magnetic enhancement can be seen in figure 23 (i), showing the calculated number of electrons transferred under ORR conditions for experiments performed with and without a field. The HESO/C intrinsically shows n=3.123, indicating that both the 2 and 4 electron ORR pathways are present. After the field is applied, the calculated electron number increases to 3.892, indicating that the 4-electron pathway is more favoured under the magnetic field. The 4-electron pathway is preferred as it is more energy efficient and does not produce H_2O_2 as an intermediate, which can damage cell components.

Cyclic voltammetry under a magnetic field was also performed, as shown in figure 23 (j-k). The non-faradaic current under a magnetic field is significantly suppressed. This may be due to Lorentz force currents at the electrode surface preventing the build-up of ions and disrupting the formation of a Helmholtz plane.[54] This would imply that magnetic enhancement may not be a viable strategy for supercapacitor applications.

The Tafel plots in figure 24 (a) show that the applied field decreased the Tafel slope by 10 mV/dec in ORR conditions, a modest but definite improvement in energy efficiency. In terms of kinetics this suggests an increase in the rate of the first electron transfer step, though it remains the rate limiting step. Under OER conditions the change is only 2 $mV.dec^{-1}$, as shown in figure 24 (b). The slope above 250 $mV.dec^{-1}$ indicates that the first electron transfer step is the rate limiting step.[139] This step in OER does not involve a spin change, and so the lack of magnetic enhancement is consistent.

Electronic impedance spectroscopy in figure 24 (c) also only showed the influence of the magnetic field in 0.1 M KOH ORR conditions in the kinetic controlled region. The magnetic field reduced mass transport resistance slightly from 43.48 **Ω** to 42.64 **Ω**, while the sum of charge transfer resistances decreased from 33.3 **Ω** to 29.46 **Ω**. The equivalent circuit indicates that two distinct surfaces are active for ORR, with one being slightly more susceptible to magnetic enhancement: R2 decreased from 19.33 to 17.94 **Ω**, while R3 showed a more significant decrease from 13.97 to 11.54 **Ω**. Overall, the magnetic field caused slight improvements to both mass transport and charge transfer processes, though charge transfer is the greater effect. According the Tafel slope analysis, the first electron transfer step is the rate limiting step.[139] This step involves a spin state change, and so is susceptible to magnetic enhancement.

By contrast, no change was seen in the OER EIS in figure 24 (d) after application of the field. The mass transport resistance R1 is lower than under ORR conditions at only 6.9 **Ω**, with the charge transfer resistances R2 and R3 being 33.1 and 2.5 **Ω**, respectively. The lower transport resistance is due to the higher concentration of hydroxide as compared to dissolved oxygen: 1 $mol.cm^{-3}$ OH^- being three orders of magnitude greater than the $1.2 * 10^{-3}$ $mol.dm^{-3}$ O_2. The magnetic field would still accelerate mass transport, but the enhancement is too small to be

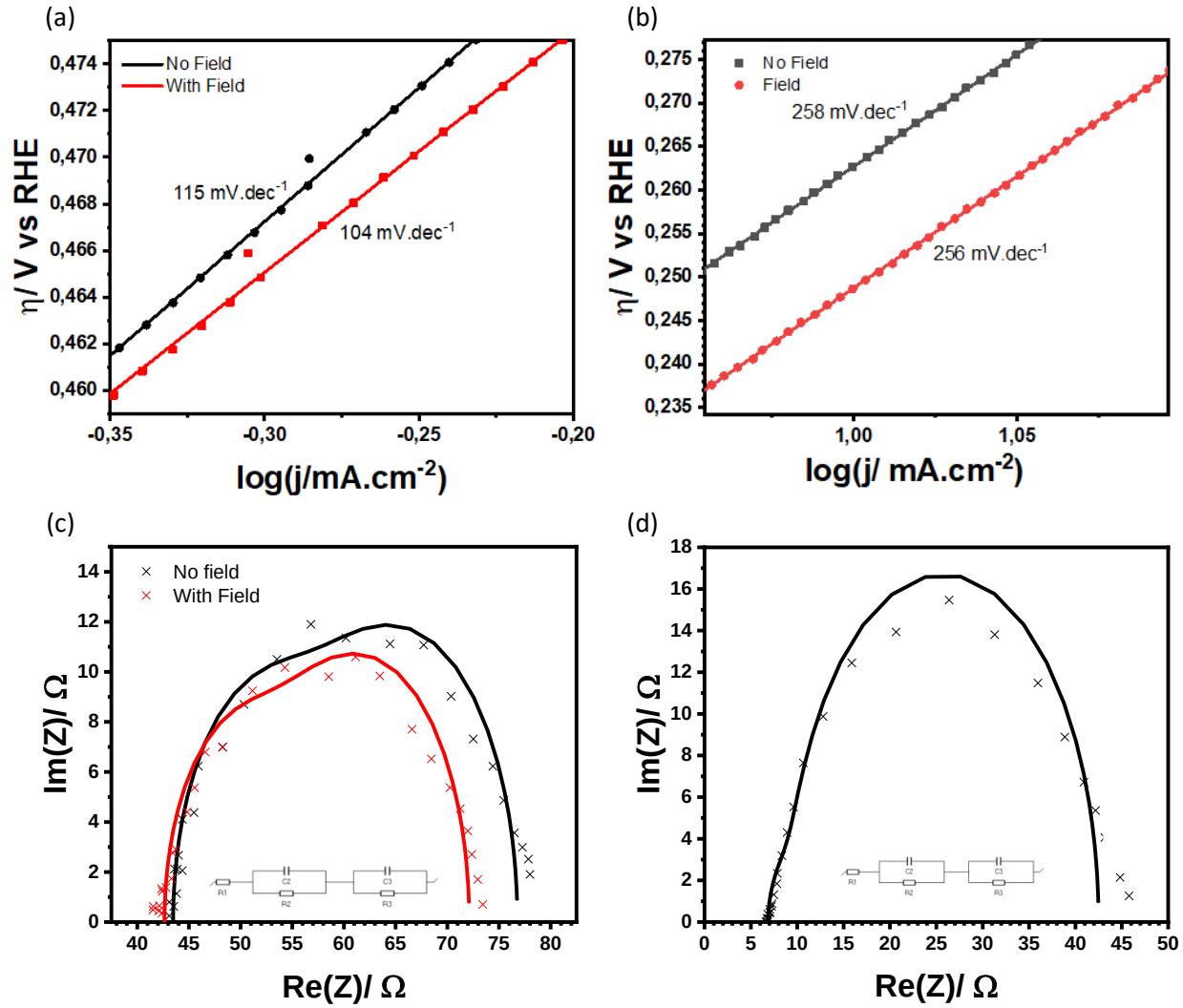


Figure 24: Tafel plots for 20% HESO/C with and without an applied field under a) ORR and b) OER conditions. EIS for 20% HESO/C at c) 0.85 V and d) 1.6 V

reliably detected under the faster mass transport conditions seen in the OER compared to the ORR.

The Kelvin force removal of oxygen bubbles is not manifested in the EIS, but may be responsible for the slightly earlier E_{10} in the OER as fewer sites are blocked by oxygen bubbles. The difference between R2 and R3 once again indicates the presence of 2 active sites, with the one indicated by R3 being an order of magnitude more active to OER than the one indicated by R2. This contrasts with the ORR active sites, where the charge transfer resistance between R2 and R3 was only ~6 Ω. The magnetic field also had no detectable effect on the charge transfer resistances. From the Tafel analysis, the rate limiting step for the OER in this region is

the first electron transfer step, which does not involve a spin-state change. Charge transfer in OER should therefore not be significantly impacted by the magnetic field.

Overall, the applied magnetic field yields slight improvement to onset potentials in the 3-electrode tests. Comparison with previous oxygen catalysis studies shown in table 6. The extent of magnetic enhancement seen in these tests is low compared to other studies. The power of including a magnetic field only becomes truly remarkable in the following two electrode tests.

Table 5: Comparison of ORR and OER magnetic enhancement with previous studies

Catalyst	**Magnetic Field/ mT**	**OER E_{10} /V**	**ORR $E_{1/2}$ /V**	**ΔE/ mV**	**Reference**
20% $(CuCoFeMnNi)_{3/5}O_4$/C	0	1.493	0.772	721	This work
	350	1.479	0.773	700	
Co/CNF	0	1.650	0.800	850	[1][59]
	350	1.635	0.820	820	
$FeCo_2O_4$ nanofibre	0	1.580	N/A	N/A	[2][61]
	1000	1.540	N/A	N/A	
$FeCo_2O_4$	0	1.58	0.78	800	[3][60]
	Residual	1.52	0.80	720	
Ni1.5Co1.5O4/Ni foam	0	1.520	N/A	N/A	[4][62]
	125	1.478	N/A	N/A	
(Fe+N+S)/C	0	N/A	0.88	N/A	[5][53]
	140	N/A	0.91	N/A	

4.11 Two-electrode tests on a zinc-air test cell

Figure 25 shows the assembled zinc-air battery (a), and its power profiles with and without the magnetic field (b). Without the field, the peak power is mediocre, reaching 108.4 mW.cm^{-2} at 199 mA.cm^{-2}. However, once the magnetic field is applied the power increases significantly, reaching a peak of 176.2 mW.cm^{-2} at 311 mA.cm^{-2}. With the magnetic field, the peak power exceeds the 103.5 mW.cm^{-2} of mixed Pt/C and IrO_2 RZAB cathodes.[82,140] For completeness, a RZAB with a standard 20% Pt/C + IrO_2 cathode was tested with and without a magnetic field under the same conditions. Previous studies have excluded their standard cathode from the magnetic field studies,[30,61] perhaps because these materials do not exhibit ferromagnetism or because of findings like Garcés-Pineda (2019),[48] where the magnetic field had no effect on the OER performance of IrO_2 in a three electrode system. In contrast, we report that 20% Pt/C + IrO_2 shows a small but noteworthy enhancement in power under a magnetic field, from 103.5

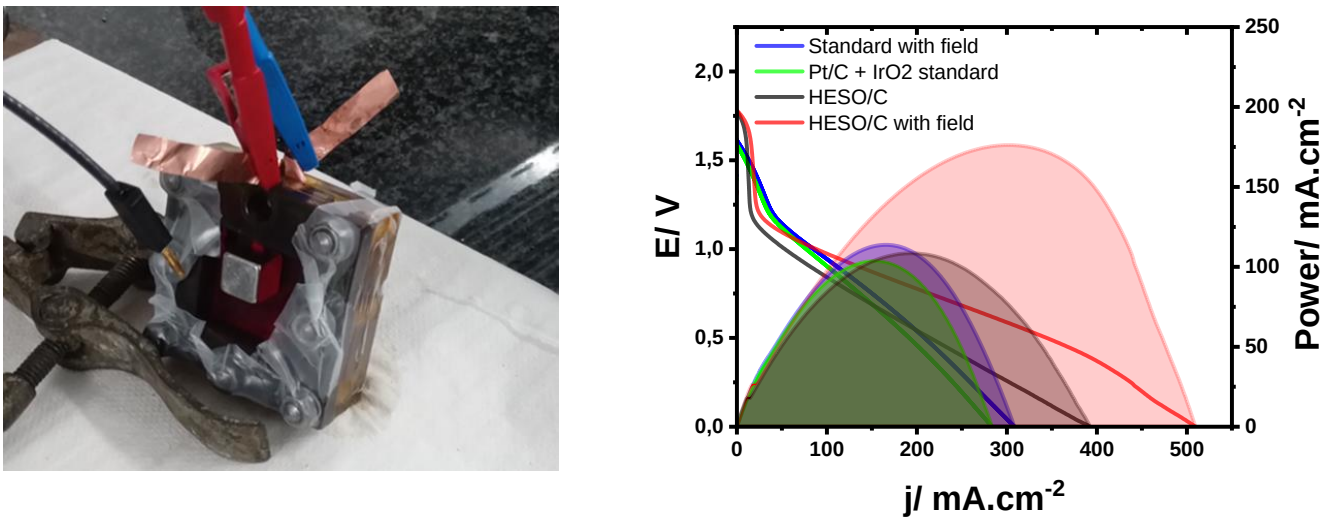


Figure 25: a) The assembled zinc-air battery. b) Power profiles of the standard 20% Pt/C + IrO2 cathode and the 20% HESO/C cathode, with and without an applied field

mW.cm^{-2} to 113.7 mW.cm^{-2} under the field. This is due to the paramagnetic IrO_2 allowing for a small degree of spin alignment as well as the facilitation of mass transport. This result shows that even paramagnetic catalyst may be appropriate candidates for magnetic enhancement.

However, this enhancement pales in comparison to the leap in power seen in the 20% HESO/C, which is the most significant magnetic enhancement of RZAB power yet reported (Table 6)

Table 6: Previous achievements in magnetic enhancement of RZABs

Cathode	Magnetic field /mT	Peak Power /mW.cm^{-2}	ΔE /mV	DoD /%	Energy /mWh.cm^{-2}	Stability /h (cycles)	Reference
20% (CuCoFeMnNi)$_{3/5}$O$_4$/C	0	108	835	25	43.1	80 (3)	This Work
	350	176	818	25	43.2	140 (4)	
Co/CNF	0	N/A	880	2.3	0.175	78 (936)	[1][59]
	350	100	820	2.3*	0.173	155 (1860)	
20% Pt/C + IrO_2	0	114	740	25	48.00	86 (2)	This work
	350	104	675	25	47.75	37 (1)	
$FeCo_2O_4$ nanofibre	0	97.3	840	0.115	1.00	5 (15)	[2][61]
	1000	108.2	780	0.115	1.02	5 (15)	
$FeCo_2O_4$	0	105	790	0.23	0.41	182.5 (547)	[3][60]
	Residual ***	123	750	0.23	0.42	190 (570)	
AlNiCoFeCrMoV/Co-N-C	0	162	680	8.53	6.00	700(700)	[6][81]

Part of the reason can be seen in the impedance spectroscopy shown in figure 27. The equivalent circuit represents the mass transport resistance in R1, catalysis on the HESO in R2. After the field is applied, charge transfer resistance R2 is decreased by 10 Ω, from 20 to

10 Ω. In contrast, mass transport resistance R1 increased slightly, from 4 to 5 Ω. This result is an interesting deviation from the three-electrode system explored in figure 24 (m). Charge transfer resistance, heavily dependent on spintronic effects at the active sites, is reduced to a far greater extent in the 2-electrode system. There are several possible contributing factors. Firstly, the cell configuration shown in figure 25 (a) has the magnetic field perpendicular to the electrode surfaces, whereas in the 3-electrode tests it was at an angle by necessity, as well as being further from the electrode (5 cm as compared to 0.5 cm).

More peculiarly, the mass transport resistance was slightly increased in the two-electrode system, as opposed to the small decrease seen in the three-electrode system. The electrolyte is 60 times more concentrated in the RZAB than the three-electrode test and contains zinc cations in addition to hydroxide anions (anions and cations experience Lorentz forces in opposite directions). It is possible that interfering Lorentz force currents create turbulence, retarding the current through the electrolyte instead of aiding mass transport. The trend towards formation of zinc hydroxide complexes further confounds the magnetohydrodynamic effects, as the zinc and hydroxide ions are electrostatically attracted while the Lorentz force tends to pull them apart.

Despite this increase in mass transport resistance, the overall effect of the field remains positive as the decrease in charge transfer resistance is an order of magnitude more significant.

Table 7: EIS parameters of RZAB with 20% HESO/C cathode

Parameter	Before Field	With Field	After Stability
R1 (Ohm)	3,98 ± 1	4,965 ± 1,15	4,092 ± 0,4
R2 (Ohm)	19,57 ± 2,2	9,747 ± 2,6	23,63 ± 1,7
Q2 ($F.s^{a-1}$)	0,0023 ± 0,0018	0,011 ± 0,023	0,0052 ± 0,004
a2	0,35	0,489	0,713
Q3 ($F.s^{a-1}$)	0,016 ± 0,0007	0,017 ± 0,0018	0,027 ± 0,01
a3	0,827	0,802	0,7131 ± 0,816

The discharge voltages-with 20-minute charge and discharge cycles- at various currents were investigated, with and without a magnetic field. Figure 27 (a) shows the results in the absence of the field. The discharge voltage degrades above 10 $mA.cm^{-2}$, as each cycle shows slightly lower voltage. When the current is returned to 0.5 $mA.cm^{-2}$, the discharge voltage is reduced by about 80 mV.

With an applied field, discharge voltage was less sensitive to increasing current density and the discharge voltage recovered better upon return to 0.5 $mA.cm^{-2}$, with the voltage drop being 40 mV, half of the drop experienced without the magnetic field. However, once again the discharge voltage degraded above 10 $mA.cm^{-2}$, though to slightly lesser extent. This degradation is attributed to build-up of ZnO on the anode and a consequent decrease in available surface area, rather than any changes on the cathode. It follows that the better performance at 15 $mA.cm^{-2}$ under a magnetic field is due to regulation of zinc and zincate ions at the anode, as expected from the Lorentz force diffusion currents.

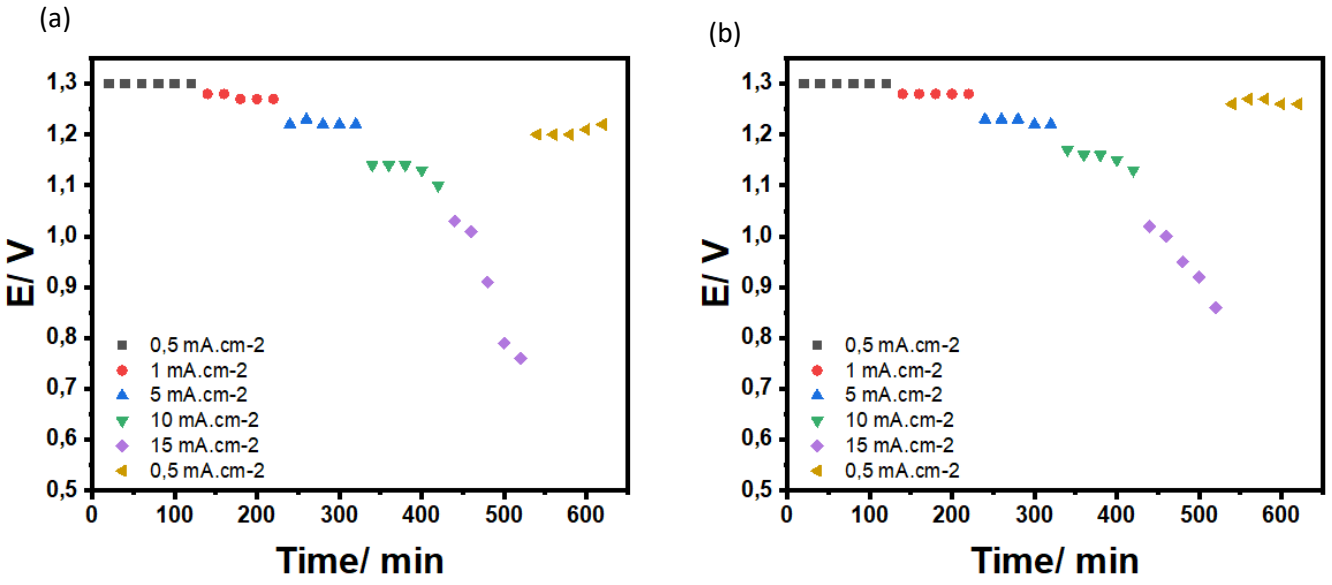


Figure 26: Rate capability tests for RZABs with (a) and without (b) a magnetic field

The results of stability testing are shown in figure 28. The RZAB shows some fluctuation in the first 30 hours, possibly due to incomplete wetting of the catalyst layer. After 30 hours, the magnetic field supresses the voltage drop compared to the unenhanced RZAB. Without the field, the voltage gap increased from 0.57 V at 50 hours to 0.62 V at 200 hours, a change of 50 mV. With the field, the gap increased from 0.26 V to 0.28 V over the same length of time, an increase of only 20 mV.

EIS from before the stability test and from after ΔV exceeded 1.5 V is shown in figure 28 (f). Bulk resistance (R1) decreased by 1 Ω due to incomplete wetting before the cycling stability test. Charge transfer resistance increased by 14 Ω to 24 Ω.

It is interesting that despite the relatively small changes seen in the three-electrode tests, the RZAB responds dramatically to the application of the field. There are several reasons for this discrepancy. Firstly, the magnetic field applied to the RZAB cathode was physically closer to the electrode than that applied at the working electrode in the three electrode tests, due to the constraints of the cell designs. Magnetic fields, being produced by magnetic dipoles, weaken

as a function of r^{-3}, meaning that distance to the electrode of interest is extremely impactful. The stronger magnetic field impacts all aspects of magnetic enhancement, from spin alignment to mass transport. The magnetic field at the catalyst in the 3-electrode experiments was therefore likely weaker than 350 mT. Secondly, the magnetic field direction and magnitude are fixed in the RZAB, as the entire cell is static. However, in the three-electrode system the working electrode is mobile and rotates during testing. This means that the magnetic field at the electrode surface is constantly changing, and so spin alignment especially may not have a chance to manifest. EIS on the stationary three electrode system did detect both a reduced mass transport as well as charge transfer resistance after application of the field, though only under ORR conditions. Finally, in a RZAB the anode also plays a role in the power and overall performance of the cell. In this work the anode is a simple zinc plate, and the magnetic field strength at the anode was the same as on the cathode. Lorentz force currents are therefore expected to influence the mass transport on the anode as well. While the mass transport resistance was overall increased, the turbulence at the anode may have mitigated the problems of passivation and dendrite groth.

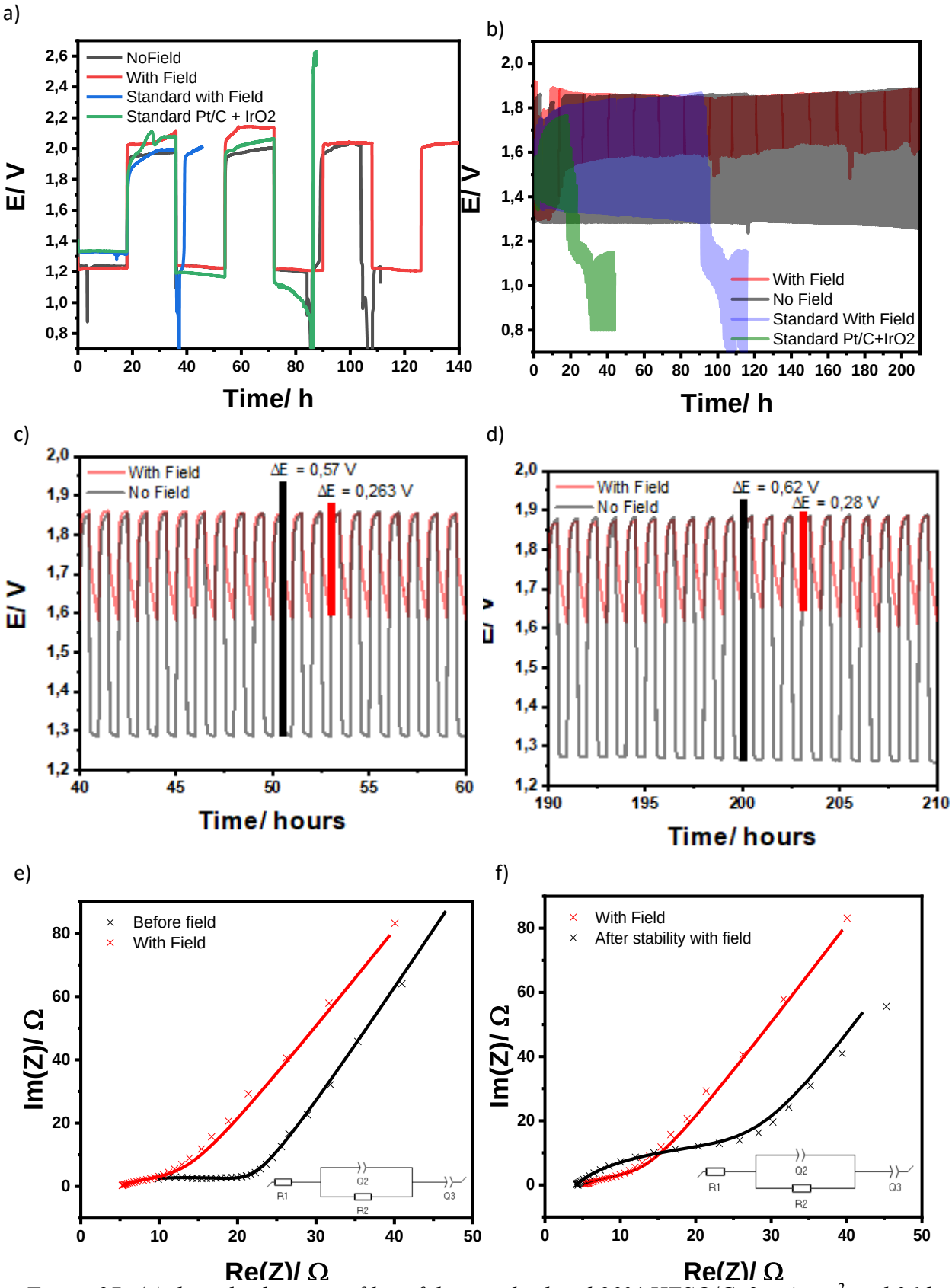


Figure 27: (a) deep discharge profiles of the standard and 20% HESO/C, 2 mA.cm^{-2} and 36 h cycles (b) Shallow discharge profiles of the standards and HESO/C 0.5 mA.cm^{-2} and 1 h cycles(c) ΔE of the 20% HESO/C around 50 hours (d) ΔE of the 20% HESO/C around 200 hours of operation (e) EIS at the OCV of the HESO/C RZAB with and without a magnetic field (f) End of life EIS at the OCV of the HESO/C RZAB before and after deep discharge cycling for 150 hours

Chapter 5: Conclusion

$(CuCoFeMnNi)_3O_4$ high entropy spinel oxide and $(CuCoFeMnNi)_3O_4$/Vulcan Carbon composite were successfully synthesized, though CuO and NiO impurities were present. The HESO structure is a partially inverted cubic spinel containing all 5 metals, with a distorted oxygen lattice. All metals were found in multiple oxidation states, especially II and III, though Cu^{+} and Mn^{4+} were also present. The HESO formed agglomerated particles larger than 100nm with CuO and NiO impurities that were excluded from the solid solution. The composites had more dispersed particles than the pristine HESO, suggesting that the composite synthesis broke the agglomerates apart. The HESO was found to be ferromagnetic by EIS.

The HESO alone showed late onset potential and low currents due to its poor electronic conductivity. This is an effect of polaron hopping in a high entropy material. The composite showed good onset potentials and currents comparable to other bifunctional catalysts in literature, with ΔE = 0.65 V, and outperformed commercial IrO_2 as an oxygen evolution catalyst, with E_{10} = 1.534 V. Tafel slopes of 120 and 250 $mV.dec^{-1}$ were found for ORR and OER, respectively, indicating that the first electron transfer step was the rate limiting step both reactions. For ORR, this involves a forbidden spin-state change, while for OER it does not. ORR is therefore expected to be more prone to magnetic enhancement on HESO/C.

The small change of 1 Ω in mass transport resistance was seen in the RDE tests suggests that the mass transport mechanism for magnetic enhancement has a positive effect in a real OER/ORR system, despite hydroxide ions propagating through the Grotthuss mechanism. The effect was inverted in the 2-electrode system, an oddity that is ascribed to the high hydroxide concentration and presence of zinc cations causing confounding currents. Mass transport enhancement may be a viable approach in lower concentration systems, such as water electrolysis.

The RZAB tests showed that the composite is a functional air cathode catalyst in a real system, but the application of the magnetic field produced an enhancement in power, rate capability and stability. In particular, application of the field improved the peak power from 108.4 $mW.cm^{-2}$ to 176.2 $mW.cm^{-2}$

This study reinforces the appeal of high entropy materials in electrochemistry and clearly shows that a static magnetic field is a viable approach to enhancing OER/ORR catalysis. It was demonstrated that combined approaches may be used for the development of functional electrochemistry, for a sustainable, high technology future.

5.2 Recommendations

1. All electrocatalysis projects must begin with a thorough optimisation of the synthesis to ensure controlled nanoparticle size and morphology. The use of surfactants or templates could give more reproducible, uniform catalysts.
2. The exclusion of some copper and nickel suggests that further steps must be taken to control HESO composition, such as using high entropy metal-organic frameworks as a precursor.
3. External magnetic fields should be produced by an electromagnet with variable strength.
4. $(CuCoFeMnNi)_3O_4$ HESO and its analogues with varying metal stoichiometries should be screened, following recommendations 1 and 2, to identify trends. For example, how does magnetic enhancement change as the proportion of manganese is varied from 0% to 50%.

5. Extended X-ray Absorption Fine Structures (EXAFS) analysis should be used to elucidate the local environments of each metal separately.
6. In-situ and Operando XPS, PDF and EXAFS should be used to examine how oxidation states, lattice strain and local environments change at different potentials, during cell operation, and under the influence of a magnetic field.
7. Density Functional Theory modelling should be used to examine how the structural information gained in recommendations 4 and 5 change the electronic band structure and reactant binding energies.
8. Practical RZABS must use solid or gel electrolytes, or use electrolyte additives to prevent parasitic reactions.
9. Advanced cathode materials are starting to outlast and outperform simple zinc plate anodes. Anode failure therefore becomes a confounding factor in cathode testing. There are several possible strategies to rectify this, though each has its own drawbacks:
    a. Replacing the anode regularly prevents anode degradation but interferes with normal cell operation
    b. The use of advanced anodes, such as nanostructured zinc-carbon composites or the use of coatings and solid-electrolyte interface engineering may give better performance, but these approaches are themselves experimental and may give additional confounding factors
10. This HESO has proven very effective at OER catalysis in particular, and so should be tested in a water splitting application.
11. Magnetic enhancement is clearly a promising strategy, and further research in experimental and practical applications is warranted for susceptible oxygen catalysts.

References

(1) Capellán-Pérez, I.; Mediavilla, M.; de Castro, C.; Carpintero, Ó.; Miguel, L. J. Fossil Fuel Depletion and Socio-Economic Scenarios: An Integrated Approach. *Energy* **2014**, *77*, 641–666. https://doi.org/10.1016/j.energy.2014.09.063.

(2) Healy, N.; Stephens, J. C.; Malin, S. A. Embodied Energy Injustices: Unveiling and Politicizing the Transboundary Harms of Fossil Fuel Extractivism and Fossil Fuel Supply Chains. *Energy Res. Soc. Sci.* **2019**, *48*, 219–234. https://doi.org/10.1016/j.erss.2018.09.016.

(3) Kopel, J.; Brower, G. L. Impact of Fossil Fuel Emissions and Particulate Matter on Pulmonary Health. *Proc. Bayl. Univ. Med. Cent.* **2019**, *32* (4), 636–638. https://doi.org/10.1080/08998280.2019.1641367.

(4) Luidold, S.; Antrekowitsch, H. Hydrogen as a Reducing Agent: State-of-the-Art Science and Technology. *JOM* **2007**, *59* (6), 20–26. https://doi.org/10.1007/s11837-007-0072-x.

(5) Chao, D.; Zhou, W.; Xie, F.; Ye, C.; Li, H.; Jaroniec, M.; Qiao, S.-Z. Roadmap for Advanced Aqueous Batteries: From Design of Materials to Applications. *Sci. Adv.* **2020**, *6* (21), eaba4098. https://doi.org/10.1126/sciadv.aba4098.

(6) Liu, Q.; Pan, Z.; Wang, E.; An, L.; Sun, G. Aqueous Metal-Air Batteries: Fundamentals and Applications. *Energy Storage Mater.* **2020**, *27*, 478–505. https://doi.org/10.1016/j.ensm.2019.12.011.

(7) Li, Y.; Lu, J. Metal–Air Batteries: Will They Be the Future Electrochemical Energy Storage Device of Choice? *ACS Energy Lett.* **2017**, *2* (6), 1370–1377. https://doi.org/10.1021/acsenergylett.7b00119.

(8) Zhang, Y.-L.; Goh, K.; Zhao, L.; Sui, X.-L.; Gong, X.-F.; Cai, J.-J.; Zhou, Q.-Y.; Zhang, H.-D.; Li, L.; Kong, F.-R.; Gu, D.-M.; Wang, Z.-B. Advanced Non-Noble Materials in Bifunctional Catalysts for ORR and OER toward Aqueous Metal–Air Batteries. *Nanoscale* **2020**, *12* (42), 21534–21559. https://doi.org/10.1039/D0NR05511E.

(9) Haruna, A. B.; Ozoemena, K. I. Manganese-Based Bifunctional Electrocatalysts for Zinc-Air Batteries. *Curr. Opin. Electrochem.* **2020**, *21*, 219–224. https://doi.org/10.1016/j.coelec.2020.02.021.

(10) Wang, H.-F.; Xu, Q. Materials Design for Rechargeable Metal-Air Batteries. *Matter* **2019**, *1* (3), 565–595. https://doi.org/10.1016/j.matt.2019.05.008.

(11) Gorlin, Y.; Lassalle-Kaiser, B.; Benck, J. D.; Gul, S.; Webb, S. M.; Yachandra, V. K.; Yano, J.; Jaramillo, T. F. In Situ X-Ray Absorption Spectroscopy Investigation of a Bifunctional Manganese Oxide Catalyst with High Activity for Electrochemical Water Oxidation and Oxygen Reduction. *J. Am. Chem. Soc.* **2013**, *135* (23), 8525–8534. https://doi.org/10.1021/ja3104632.

(12) Li, S.; Guo, H.; He, S.; Yang, H.; Liu, K.; Duan, G.; Jiang, S. Advanced Electrospun Nanofibers as Bifunctional Electrocatalysts for Flexible Metal-Air (O2) Batteries: Opportunities and Challenges. *Mater. Des.* **2022**, *214*, 110406. https://doi.org/10.1016/j.matdes.2022.110406.

(13) Nguyen, T. X.; Liao, Y.-C.; Lin, C.-C.; Su, Y.-H.; Ting, J.-M. Advanced High Entropy Perovskite Oxide Electrocatalyst for Oxygen Evolution Reaction. *Adv. Funct. Mater.* **2021**, *31* (27), 2101632. https://doi.org/10.1002/adfm.202101632.

(14) Niether, C.; Faure, S.; Bordet, A.; Deseure, J.; Chatenet, M.; Carrey, J.; Chaudret, B.; Rouet, A. Improved Water Electrolysis Using Magnetic Heating of FeC–Ni Core–Shell Nanoparticles. *Nat. Energy* **2018**, *3* (6), 476–483. https://doi.org/10.1038/s41560-018-0132-1.

(15) Liang, Q.; Brocks, G.; Bieberle-Hütter, A. Oxygen Evolution Reaction (OER) Mechanism under Alkaline and Acidic Conditions. *J. Phys. Energy* **2021**, *3* (2), 026001. https://doi.org/10.1088/2515-7655/abdc85.

(16) Ma, R.; Lin, G.; Zhou, Y.; Liu, Q.; Zhang, T.; Shan, G.; Yang, M.; Wang, J. A Review of Oxygen Reduction Mechanisms for Metal-Free Carbon-Based Electrocatalysts. *Npj Comput. Mater.* **2019**, *5* (1), 1–15. https://doi.org/10.1038/s41524-019-0210-3.

(17) Sharma, L.; Katiyar, N. K.; Parui, A.; Das, R.; Kumar, R.; Tiwary, C. S.; Singh, A. K.; Halder, A.; Biswas, K. Low-Cost High Entropy Alloy (HEA) for High-Efficiency Oxygen Evolution Reaction (OER). *Nano Res.* **2021**. https://doi.org/10.1007/s12274-021-3802-4.
(18) Ali, Z.; Mehmood, M.; Ahmed, J.; Majeed, A.; Thebo, K. H. CVD Grown Defect Rich-MWCNTs with Anchored CoFe Alloy Nanoparticles for OER Activity. *Mater. Lett.* **2020**, *259*, 126831. https://doi.org/10.1016/j.matlet.2019.126831.
(19) Ye, Y. F.; Wang, Q.; Lu, J.; Liu, C. T.; Yang, Y. High-Entropy Alloy: Challenges and Prospects. *Mater. Today* **2016**, *19* (6), 349–362. https://doi.org/10.1016/j.mattod.2015.11.026.
(20) Cantor, B.; Chang, I. T. H.; Knight, P.; Vincent, A. J. B. Microstructural Development in Equiatomic Multicomponent Alloys. *Mater. Sci. Eng. A* **2004**, *375–377*, 213–218. https://doi.org/10.1016/j.msea.2003.10.257.
(21) Fu, M.; Ma, X.; Zhao, K.; Li, X.; Su, D. High-Entropy Materials for Energy-Related Applications. *iScience* **2021**, *24* (3), 102177. https://doi.org/10.1016/j.isci.2021.102177.
(22) Amiri, A.; Shahbazian-Yassar, R. Recent Progress of High-Entropy Materials for Energy Storage and Conversion. *J. Mater. Chem. A* **2021**, *9* (2), 782–823. https://doi.org/10.1039/D0TA09578H.
(23) Sun, Y.; Dai, S. High-Entropy Materials for Catalysis: A New Frontier. *Sci. Adv. 7* (20), eabg1600. https://doi.org/10.1126/sciadv.abg1600.
(24) Wang, B.; Yao, Y.; Yu, X.; Wang, C.; Wu, C.; Zou, Z. Understanding the Enhanced Catalytic Activity of High Entropy Alloys: From Theory to Experiment. *J. Mater. Chem. A* **2021**, *9* (35), 19410–19438. https://doi.org/10.1039/D1TA02718B.
(25) Tsai, J.-E.; Hong, W.-X.; Pourzolfaghar, H.; Wang, W.-H.; Li, Y.-Y. A Fe-Ni-Zn Triple Single-Atom Catalyst for Efficient Oxygen Reduction and Oxygen Evolution Reaction in Rechargeable Zn-Air Batteries. *Chem. Eng. J.* **2023**, *460*, 141868. https://doi.org/10.1016/j.cej.2023.141868.
(26) Gatard, V.; Deseure, J.; Chatenet, M. Use of Magnetic Fields in Electrochemistry: A Selected Review. *Curr. Opin. Electrochem.* **2020**, *23*, 96. https://doi.org/10.1016/j.coelec.2020.04.012.
(27) Monzon, L. M. A.; Rode, K.; Venkatesan, M.; Coey, J. M. D. Electrosynthesis of Iron, Cobalt, and Zinc Microcrystals and Magnetic Enhancement of the Oxygen Reduction Reaction. *Chem. Mater.* **2012**, *24* (20), 3878–3885. https://doi.org/10.1021/cm301766s.
(28) Roy, K.; Devi, P.; Kumar, P. Magnetic-Field Induced Sustainable Electrochemical Energy Harvesting and Storage Devices: Recent Progress, Opportunities, and Future Perspectives. *Nano Energy* **2021**, *87*, 106119. https://doi.org/10.1016/j.nanoen.2021.106119.
(29) Ren, X.; Wu, T.; Sun, Y.; Li, Y.; Xian, G.; Liu, X.; Shen, C.; Gracia, J.; Gao, H.-J.; Yang, H.; Xu, Z. J. Spin-Polarized Oxygen Evolution Reaction under Magnetic Field. *Nat. Commun.* **2021**, *12* (1), 2608. https://doi.org/10.1038/s41467-021-22865-y.
(30) Wang, Y.; Zhang, Y.; Xia, S.; Yu, J.; Ding, B. Direct Magnetic Reinforcement of Electrocatalytic ORR/OER with Electromagnetic Induction of Magnetic Catalysts. *Adv. Mater.* **2021**, *33*, 2007525. https://doi.org/10.1002/adma.202007525.
(31) Li, J.; Ma, J.; Ma, Z.; Zhao, E.; Du, K.; Guo, J.; Ling, T. Spin Effect on Oxygen Electrocatalysis. *Adv. Energy Sustain. Res.* **2021**, *2* (8), 2100034. https://doi.org/10.1002/aesr.202100034.
(32) Liu, J.-N.; Zhao, C.-X.; Wang, J.; Ren, D.; Li, B.-Q.; Zhang, Q. A Brief History of Zinc–Air Batteries: 140 Years of Epic Adventures. *Energy Environ. Sci.* **2022**, *15* (11), 4542–4553. https://doi.org/10.1039/D2EE02440C.
(33) Haruna, A. B.; Ozoemena, K. I. Manganese-Based Bifunctional Electrocatalysts for Zinc-Air Batteries. *Curr. Opin. Electrochem.* **2020**, *21*, 219–224. https://doi.org/10.1016/j.coelec.2020.02.021.
(34) William Walker. US530867A, December 11, 1894. https://patents.google.com/patent/US530867/en (accessed 2023-03-21).
(35) Scrosati, B. Lithium Rocking Chair Batteries: An Old Concept? *J. Electrochem. Soc.* **1992**, *139* (10), 2776. https://doi.org/10.1149/1.2068978.

(36) Wei, P.-S.; Hsieh, Y.-C.; Chiu, H.-H.; Yen, D.-L.; Lee, C.; Tsai, Y.-C.; Ting, T.-C. Absorption Coefficient of Carbon Dioxide across Atmospheric Troposphere Layer. *Heliyon* **2018**, *4* (10). https://doi.org/10.1016/j.heliyon.2018.e00785.
(37) Berchin, I. I.; Valduga, I. B.; Garcia, J.; de Andrade Guerra, J. B. S. O. Climate Change and Forced Migrations: An Effort towards Recognizing Climate Refugees. *Geoforum* **2017**, *84*, 147–150. https://doi.org/10.1016/j.geoforum.2017.06.022.
(38) Duvat, V. K. E.; Magnan, A. K.; Perry, C. T.; Spencer, T.; Bell, J. D.; Wabnitz, C. C. C.; Webb, A. P.; White, I.; McInnes, K. L.; Gattuso, J.-P.; Graham, N. A. J.; Nunn, P. D.; Le Cozannet, G. Risks to Future Atoll Habitability from Climate-Driven Environmental Changes. *WIREs Clim. Change* **2021**, *12* (3), e700. https://doi.org/10.1002/wcc.700.
(39) Pietrafesa, L. J.; Bao, S.; Gayes, P. T.; Carpenter, D. D.; Kowal, J. C. Variability and Trends of the Florida Current and Implications for the Future of the Gulf Stream. *J. Coast. Res.* **2022**, *38* (6), 1096–1103. https://doi.org/10.2112/JCOASTRES-D-22A-00006.1.
(40) Capellán-Pérez, I.; Mediavilla, M.; de Castro, C.; Carpintero, Ó.; Miguel, L. J. Fossil Fuel Depletion and Socio-Economic Scenarios: An Integrated Approach. *Energy* **2014**, *77*, 641–666. https://doi.org/10.1016/j.energy.2014.09.063.
(41) Ram, M.; Child, M.; Aghahosseini, A.; Bogdanov, D.; Lohrmann, A.; Breyer, C. A Comparative Analysis of Electricity Generation Costs from Renewable, Fossil Fuel and Nuclear Sources in G20 Countries for the Period 2015-2030. *J. Clean. Prod.* **2018**, *199*, 687–704. https://doi.org/10.1016/j.jclepro.2018.07.159.
(42) Li, S.; Guo, H.; He, S.; Yang, H.; Liu, K.; Duan, G.; Jiang, S. Advanced Electrospun Nanofibers as Bifunctional Electrocatalysts for Flexible Metal-Air (O2) Batteries: Opportunities and Challenges. *Mater. Des.* **2022**, *214*, 110406. https://doi.org/10.1016/j.matdes.2022.110406.
(43) Fu, J.; Liang, R.; Liu, G.; Yu, A.; Bai, Z.; Yang, L.; Chen, Z. Recent Progress in Electrically Rechargeable Zinc–Air Batteries. *Adv. Mater.* **2019**, *31* (31), 1805230. https://doi.org/10.1002/adma.201805230.
(44) *Understanding Ocean Acidification | NOAA Fisheries*. https://www.fisheries.noaa.gov/insight/understanding-ocean-acidification (accessed 2023-03-26).
(45) Li, X.; Cheng, Z.; Wang, X. Understanding the Mechanism of Oxygen Evolution Reaction (OER) with the Consideration of Spin. arXiv April 11, 2020. https://doi.org/10.48550/arXiv.2004.05326.
(46) Zhang, W.; Gao, W.; Zhang, X.; Li, Z.; Lu, G. Surface Spintronics Enhanced Photo-Catalytic Hydrogen Evolution: Mechanisms, Strategies, Challenges and Future. *Appl. Surf. Sci.* **2018**, *434*, 643–668. https://doi.org/10.1016/j.apsusc.2017.10.228.
(47) Khotseng, L. *Oxygen Reduction Reaction*; IntechOpen, 2018. https://doi.org/10.5772/intechopen.79098.
(48) Garcés-Pineda, F. A.; Blasco-Ahicart, M.; Nieto-Castro, D.; López, N.; Galán-Mascarós, J. R. Direct Magnetic Enhancement of Electrocatalytic Water Oxidation in Alkaline Media. *Nat. Energy* **2019**, *4* (6), 519–525. https://doi.org/10.1038/s41560-019-0404-4.
(49) Pere, R. Atkins - Physical Chemistry 11th Edition.
(50) Jiao, Y.; Sharpe, R.; Lim, T.; Niemantsverdriet, J. W. H.; Gracia, J. *Photosystem II Acts as a Spin-Controlled Electron Gate during Oxygen Formation and Evolution*. ACS Publications. https://doi.org/10.1021/jacs.7b07634.
(51) Teixeira da Silva, J. A.; Dobránszki, J. Magnetic Fields: How Is Plant Growth and Development Impacted? *Protoplasma* **2016**, *253* (2), 231–248. https://doi.org/10.1007/s00709-015-0820-7.
(52) Jiang, X.; Chen, Y.; Zhang, X.; You, F.; Yao, J.; Yang, H.; Xia, B. Y. Magnetic Field-Assisted Construction and Enhancement of Electrocatalysts. *ChemSusChem* **2022**, *15* (23), e202201551. https://doi.org/10.1002/cssc.202201551.
(53) Kiciński, W.; Sęk, J. P.; Matysiak-Brynda, E.; Miecznikowski, K.; Donten, M.; Budner, B.; Nowicka, A. M. Enhancement of PGM-Free Oxygen Reduction Electrocatalyst Performance for

Conventional and Enzymatic Fuel Cells: The Influence of an External Magnetic Field. *Appl. Catal. B Environ.* **2019**, *258*, 117955. https://doi.org/10.1016/j.apcatb.2019.117955.
(54) Luo, S.; Elouarzaki, K.; Xu, Z. J. Electrochemistry in Magnetic Fields. *Angew. Chem. Int. Ed.* **2022**, *61* (27), e202203564. https://doi.org/10.1002/anie.202203564.
(55) Monzon, L. M. A.; Coey, J. M. D. Magnetic Fields in Electrochemistry: The Kelvin Force. A Mini-Review. *Electrochem. Commun.* **2014**, *42*, 42–45. https://doi.org/10.1016/j.elecom.2014.02.005.
(56) Elias, L.; Chitharanjan Hegde, A. Effect of Magnetic Field on HER of Water Electrolysis on Ni–W Alloy. *Electrocatalysis* **2017**, *8* (4), 375–382. https://doi.org/10.1007/s12678-017-0382-x.
(57) Li, Y.; Zhang, L.; Peng, J.; Zhang, W.; Peng, K. Magnetic Field Enhancing Electrocatalysis of Co3O4/NF for Oxygen Evolution Reaction. *J. Power Sources* **2019**, *433*, 226704. https://doi.org/10.1016/j.jpowsour.2019.226704.
(58) Westsson, E.; Picken, S.; Koper, G. The Effect of Magnetic Field on Catalytic Properties in Core-Shell Type Particles. *Front. Chem.* **2020**, *8*.
(59) Wang, Y.; Zhang, Y.; Xia, S.; Yu, J.; Ding, B. Direct Magnetic Reinforcement of Electrocatalytic ORR/OER with Electromagnetic Induction of Magnetic Catalysts. *Adv. Mater.* **2021**, *33*, 2007525. https://doi.org/10.1002/adma.202007525.
(60) Zhang, Z.; Li, J.; Qian, J.; Li, Z.; Jia, L.; Gao, D.; Xue, D. Significant Change of Metal Cations in Geometric Sites by Magnetic-Field Annealing FeCo2O4 for Enhanced Oxygen Catalytic Activity. *Small* **2022**, *18* (7), 2104248. https://doi.org/10.1002/smll.202104248.
(61) Zhang, Z.; Jia, L.; Li, T.; Qian, J.; Liang, X.; Xue, D.; Gao, D. In-Situ Magnetic Field Enhanced Performances in Ferromagnetic FeCo2O4 Nanofibers-Based Rechargeable Zinc–Air Batteries. *J. Energy Chem.* **2023**, *78*, 447–453. https://doi.org/10.1016/j.jechem.2022.12.038.
(62) Zhang, L.; Peng, J.; Yuan, Y.; Peng, K. Magnetic Enhancement of Oxygen Evolution Reaction Performance of NiCo-Spinel Oxides. *Nanotechnology* **2021**, *32* (50), 505716. https://doi.org/10.1088/1361-6528/ac28d6.
(63) Zhang, Y.-L.; Goh, K.; Zhao, L.; Sui, X.-L.; Gong, X.-F.; Cai, J.-J.; Zhou, Q.-Y.; Zhang, H.-D.; Li, L.; Kong, F.-R.; Gu, D.-M.; Wang, Z.-B. Advanced Non-Noble Materials in Bifunctional Catalysts for ORR and OER toward Aqueous Metal–Air Batteries. *Nanoscale* **2020**, *12* (42), 21534–21559. https://doi.org/10.1039/D0NR05511E.
(64) Fu, J.; Liang, R.; Liu, G.; Yu, A.; Bai, Z.; Yang, L.; Chen, Z. Recent Progress in Electrically Rechargeable Zinc–Air Batteries. *Adv. Mater.* **2019**, *31* (31), 1805230. https://doi.org/10.1002/adma.201805230.
(65) Cui, Z.; Fu, G.; Li, Y.; Goodenough, J. B. Ni3FeN-Supported Fe3Pt Intermetallic Nanoalloy as a High-Performance Bifunctional Catalyst for Metal–Air Batteries. *Angew. Chem. Int. Ed.* **2017**, *56* (33), 9901–9905. https://doi.org/10.1002/anie.201705778.
(66) Wang, X.; Li, Y.; Jin, T.; Meng, J.; Jiao, L.; Zhu, M.; Chen, J. Electrospun Thin-Walled CuCo2O4@C Nanotubes as Bifunctional Oxygen Electrocatalysts for Rechargeable Zn–Air Batteries. *Nano Lett.* **2017**, *17* (12), 7989–7994. https://doi.org/10.1021/acs.nanolett.7b04502.
(67) Yeh, J.-W.; Chen, S.-K.; Lin, S.-J.; Gan, J.-Y.; Chin, T.-S.; Shun, T.-T.; Tsau, C.-H.; Chang, S.-Y. Nanostructured High-Entropy Alloys with Multiple Principal Elements: Novel Alloy Design Concepts and Outcomes. *Adv. Eng. Mater.* **2004**, *6* (5), 299–303. https://doi.org/10.1002/adem.200300567.
(68) Amiri, A.; Shahbazian-Yassar, R. Recent Progress of High-Entropy Materials for Energy Storage and Conversion. *J. Mater. Chem. A* **2021**, *9* (2), 782–823. https://doi.org/10.1039/D0TA09578H.
(69) Sun, L.; Cava, R. J. High-Entropy Alloy Superconductors: Status, Opportunities, and Challenges. *Phys. Rev. Mater.* **2019**, *3* (9), 090301. https://doi.org/10.1103/PhysRevMaterials.3.090301.
(70) Sun, Y.; Dai, S. High-Entropy Materials for Catalysis: A New Frontier. *Sci. Adv.* **2022**, *7* (20), eabg1600. https://doi.org/10.1126/sciadv.abg1600.
(71) Yao, Y.; Huang, Z.; Xie, P.; Lacey, S. D.; Jacob, R. J.; Xie, H.; Chen, F.; Nie, A.; Pu, T.; Rehwoldt, M.; Yu, D.; Zachariah, M. R.; Wang, C.; Shahbazian-Yassar, R.; Li, J.; Hu, L. Carbothermal Shock

Synthesis of High-Entropy-Alloy Nanoparticles. *Science* **2018**, *359* (6383), 1489–1494. https://doi.org/10.1126/science.aan5412.

(72) Rost, C. M.; Sachet, E.; Borman, T.; Moballegh, A.; Dickey, E. C.; Hou, D.; Jones, J. L.; Curtarolo, S.; Maria, J.-P. Entropy-Stabilized Oxides. *Nat. Commun.* **2015**, *6* (1), 8485. https://doi.org/10.1038/ncomms9485.

(73) Mohili, R.; Hemanth, N. R.; Jin, H.; Lee, K.; Chaudhari, N. Emerging High Entropy Metal Sulphides and Phosphides for Electrochemical Water Splitting. *J. Mater. Chem. A* **2023**, *11* (20), 10463–10472. https://doi.org/10.1039/D2TA10081A.

(74) He, S.; Somayaji, V.; Wang, M.; Lee, S.-H.; Geng, Z.; Zhu, S.; Novello, P.; Varanasi, C. V.; Liu, J. High Entropy Spinel Oxide for Efficient Electrochemical Oxidation of Ammonia. *Nano Res.* **2021**. https://doi.org/10.1007/s12274-021-3665-8.

(75) Nguyen, T. X.; Liao, Y.-C.; Lin, C.-C.; Su, Y.-H.; Ting, J.-M. Advanced High Entropy Perovskite Oxide Electrocatalyst for Oxygen Evolution Reaction. *Adv. Funct. Mater.* **2021**, *31* (27), 2101632. https://doi.org/10.1002/adfm.202101632.

(76) Wang, L.; Hossain, M. D.; Du, Y.; Chambers, S. A. Exploring the Potential of High Entropy Perovskite Oxides as Catalysts for Water Oxidation. *Nano Today* **2022**, *47*, 101697. https://doi.org/10.1016/j.nantod.2022.101697.

(77) Hu, J.; Cao, L.; Wang, Z.; Liu, J.; Zhang, J.; Cao, Y.; Lu, Z.; Cheng, H. Hollow High-Entropy Metal Organic Framework Derived Nanocomposite as Efficient Electrocatalyst for Oxygen Reduction Reaction. *Compos. Commun.* **2021**, *27*, 100866. https://doi.org/10.1016/j.coco.2021.100866.

(78) Feng, D.; Dong, Y.; Zhang, L.; Ge, X.; Zhang, W.; Dai, S.; Qiao, Z.-A. Holey Lamellar High-Entropy Oxide as an Ultra-High-Activity Heterogeneous Catalyst for Solvent-Free Aerobic Oxidation of Benzyl Alcohol. *Angew. Chem.* **2020**, *132* (44), 19671–19677. https://doi.org/10.1002/ange.202004892.

(79) Bhargava, A.; Eppstein, R.; Sun, J.; Smeaton, M. A.; Paik, H.; Kourkoutis, L. F.; Schlom, D. G.; Caspary Toroker, M.; Robinson, R. D. Breakdown of the Small-Polaron Hopping Model in Higher-Order Spinels. *Adv. Mater.* **2020**, *32* (49), 2004490. https://doi.org/10.1002/adma.202004490.

(80) Lu, Z.; Zhu, J.; Andrew Payzant, E.; Paranthaman, M. P. Electrical Conductivity of the Manganese Chromite Spinel Solid Solution. *J. Am. Ceram. Soc.* **2005**, *88* (4), 1050–1053. https://doi.org/10.1111/j.1551-2916.2005.00205.x.

(81) Yu, T.; Xu, H.; Jin, Z.; Zhang, Y.; Qiu, H.-J. Noble Metal-Free High-Entropy Oxide/Co-N-C Bifunctional Electrocatalyst Enables Highly Reversible and Durable Zn-Air Batteries. *Appl. Surf. Sci.* **2023**, *610*, 155624. https://doi.org/10.1016/j.apsusc.2022.155624.

(82) Jin, Z.; Zhou, X.; Hu, Y.; Tang, X.; Hu, K.; Reddy, K. M.; Lin, X.; Qiu, H.-J. A Fourteen-Component High-Entropy Alloy@oxide Bifunctional Electrocatalyst with a Record-Low ΔE of 0.61 V for Highly Reversible Zn–Air Batteries. *Chem. Sci.* **2022**. https://doi.org/10.1039/D2SC04461G.

(83) He, R.; Yang, L.; Zhang, Y.; Wang, X.; Lee, S.; Zhang, T.; Li, L.; Liang, Z.; Chen, J.; Li, J.; Ostovari Moghaddam, A.; Llorca, J.; Ibáñez, M.; Arbiol, J.; Xu, Y.; Cabot, A. A CrMnFeCoNi High Entropy Alloy Boosting Oxygen Evolution/Reduction Reactions and Zinc-Air Battery Performance. *Energy Storage Mater.* **2023**, *58*, 287–298. https://doi.org/10.1016/j.ensm.2023.03.022.

(84) Jin, Z.; Lyu, J.; Zhao, Y.-L.; Li, H.; Lin, X.; Xie, G.; Liu, X.; Kai, J.-J.; Qiu, H.-J. Rugged High-Entropy Alloy Nanowires with in Situ Formed Surface Spinel Oxide As Highly Stable Electrocatalyst in Zn–Air Batteries. *ACS Mater. Lett.* **2020**, *2* (12), 1698–1706. https://doi.org/10.1021/acsmaterialslett.0c00434.

(85) Fang, G.; Gao, J.; Lv, J.; Jia, H.; Li, H.; Liu, W.; Xie, G.; Chen, Z.; Huang, Y.; Yuan, Q.; Liu, X.; Lin, X.; Sun, S.; Qiu, H.-J. Multi-Component Nanoporous Alloy/(Oxy)Hydroxide for Bifunctional Oxygen Electrocatalysis and Rechargeable Zn-Air Batteries. *Appl. Catal. B Environ.* **2020**, *268*, 118431. https://doi.org/10.1016/j.apcatb.2019.118431.

(86) Cao, X.; Gao, Y.; Wang, Z.; Zeng, H.; Song, Y.; Tang, S.; Luo, L.; Gong, S. FeNiCrCoMn High-Entropy Alloy Nanoparticles Loaded on Carbon Nanotubes as Bifunctional Oxygen Catalysts for

Rechargeable Zinc-Air Batteries. *ACS Appl. Mater. Interfaces* **2023**, *15* (27), 32365–32375. https://doi.org/10.1021/acsami.3c04120.

(87) Yu, T.; Zhang, Y.; Hu, Y.; Hu, K.; Lin, X.; Xie, G.; Liu, X.; Reddy, K. M.; Ito, Y.; Qiu, H.-J. Twelve-Component Free-Standing Nanoporous High-Entropy Alloys for Multifunctional Electrocatalysis. *ACS Mater. Lett.* **2022**, *4* (1), 181–189. https://doi.org/10.1021/acsmaterialslett.1c00762.

(88) Zhang, Y.; Lyu, J.; Zhao, Y.-L.; Hu, K.; Chen, Z.; Lin, X.; Xie, G.; Liu, X.; Qiu, H.-J. In Situ Coupling of Ag Nanoparticles with High-Entropy Oxides as Highly Stable Bifunctional Catalysts for Wearable Zn–Ag/Zn–Air Hybrid Batteries. *Nanoscale* **2021**, *13* (38), 16164–16171. https://doi.org/10.1039/D1NR03539H.

(89) Wang, D.; Liu, Z.; Du, S.; Zhang, Y.; Li, H.; Xiao, Z.; Chen, W.; Chen, R.; Wang, Y.; Zou, Y.; Wang, S. Low-Temperature Synthesis of Small-Sized High-Entropy Oxides for Water Oxidation. *J. Mater. Chem. A* **2019**, *7* (42), 24211–24216. https://doi.org/10.1039/C9TA08740K.

(90) Song, F.; Busch, M.; Lassalle, B.; Hsu, C.-S.; Petkucheva, E.; Bensimon, M.; Chen, H.; Corminboeuf, C.; Hu, X. An Unconventional Iron Nickel Catalyst for the Oxygen Evolution Reaction. *ACS Cent. Sci.* **2019**, *5*. https://doi.org/10.1021/acscentsci.9b00053.

(91) Xiong, Y.; He, P. A Review on Electrocatalysis for Alkaline Oxygen Evolution Reaction (OER) by Fe-Based Catalysts. *J. Mater. Sci.* **2023**, *58* (5), 2041–2067. https://doi.org/10.1007/s10853-023-08176-1.

(92) Liu, J.; Wang, R.; Chen, Z.; Hu, N.; Chaohe, X.; Shen, Z. Nanocarbon Based Electrocatalysts for Rechargeable Aqueous Li/Zn-Air Batteries. *ChemElectroChem* **2018**, *5*. https://doi.org/10.1002/celc.201800141.

(93) *US3330697A - Method of preparing lead and alkaline earth titanates and niobates and coating method using the same to form a capacitor - Google Patents*. https://patents.google.com/patent/US3330697A/en (accessed 2024-01-18).

(94) Runčevski, T.; Brown, C. M. The Rietveld Refinement Method: Half of a Century Anniversary. *Cryst. Growth Des.* **2021**, *21* (9), 4821–4822. https://doi.org/10.1021/acs.cgd.1c00854.

(95) *Underneath the Bragg Peaks, Volume 16 - 2nd Edition | Elsevier Shop*. https://shop.elsevier.com/books/underneath-the-bragg-peaks/egami/978-0-08-097133-9 (accessed 2024-02-19).

(96) Durante, C. Metal–Carbon Interaction in Metal Nanoparticles and Implication in the Electrocatalysis of Oxygen Reduction. *Curr. Opin. Electrochem.* **2022**, *36*, 101119. https://doi.org/10.1016/j.coelec.2022.101119.

(97) Granite. *How to Choose Your Lasers for Raman Spectroscopy | Quick Guide*. Edinburgh Instruments. https://www.edinst.com/us/blog/lasers-for-raman-spectroscopy/ (accessed 2024-05-04).

(98) Wieboldt, D. Understanding Raman Spectrometer Parameters. **2010**, *0*.

(99) Gu, K.; Wang, D.; Xie, C.; Wang, T.; Huang, G.; Liu, Y.; Zou, Y.; Tao, L.; Wang, S. Defect-Rich High-Entropy Oxide Nanosheets for Efficient 5-Hydroxymethylfurfural Electrooxidation. *Angew. Chem.* **2021**, *133* (37), 20415–20420. https://doi.org/10.1002/ange.202107390.

(100) Zhang, J.; Liu, H.; Gu, Y.; Zhang, J.; Zhang, X.; Qi, X. Oxygen-Vacancy-Related Dielectric Relaxations and Electrical Properties in [Lix(BaSrCaMg)(1−x)/4]TiO3 High-Entropy Perovskite Ceramics. *J. Mater. Sci. Mater. Electron.* **2022**, *33* (13), 9918–9929. https://doi.org/10.1007/s10854-022-07982-8.

(101) Haryński, Ł.; Olejnik, A.; Grochowska, K.; Siuzdak, K. A Facile Method for Tauc Exponent and Corresponding Electronic Transitions Determination in Semiconductors Directly from UV–Vis Spectroscopy Data. *Opt. Mater.* **2022**, *127*, 112205. https://doi.org/10.1016/j.optmat.2022.112205.

(102) Whitten, J. E. Ultraviolet Photoelectron Spectroscopy: Practical Aspects and Best Practices. *Appl. Surf. Sci. Adv.* **2023**, *13*, 100384. https://doi.org/10.1016/j.apsadv.2023.100384.

(103) Elgrishi, N.; Rountree, K. J.; McCarthy, B. D.; Rountree, E. S.; Eisenhart, T. T.; Dempsey, J. L. A Practical Beginner's Guide to Cyclic Voltammetry. *J. Chem. Educ.* **2018**, *95* (2), 197–206. https://doi.org/10.1021/acs.jchemed.7b00361.
(104) Connor, P.; Schuch, J.; Kaiser, B.; Jaegermann, W. The Determination of Electrochemical Active Surface Area and Specific Capacity Revisited for the System MnOx as an Oxygen Evolution Catalyst. *Z. Für Phys. Chem.* **2020**, *234* (5), 979–994. https://doi.org/10.1515/zpch-2019-1514.
(105) Trasatti, S.; Petrii, O. A. Real Surface Area Measurements in Electrochemistry. *Pure Appl. Chem.* **1991**, *63* (5), 711–734. https://doi.org/10.1351/pac199163050711.
(106) van der Heijden, O.; Park, S.; Vos, R. E.; Eggebeen, J. J. J.; Koper, M. T. M. Tafel Slope Plot as a Tool to Analyze Electrocatalytic Reactions. *ACS Energy Lett.* **2024**, *9* (4), 1871–1879. https://doi.org/10.1021/acsenergylett.4c00266.
(107) Wang, Y.; Li, H.; Liu, H.; Yang, L.; Zeng, C. Preparation and Formation Mechanism of Cr-Free Spinel-Structured High Entropy Oxide (MnFeCoNiCu)3O4. *Ceram. Int.* **2023**, *49* (2), 1940–1946. https://doi.org/10.1016/j.ceramint.2022.09.159.
(108) Liu, X.; Cui, S.; Qian, M.; Sun, Z.; Du, P. In Situ Generated Highly Active Copper Oxide Catalysts for the Oxygen Evolution Reaction at Low Overpotential in Alkaline Solutions. *Chem. Commun.* **2016**, *52* (32), 5546–5549. https://doi.org/10.1039/C6CC00526H.
(109) Ali Akbari, M. S.; Bagheri, R.; Song, Z.; Najafpour, M. M. Oxygen-Evolution Reaction by Nickel/Nickel Oxide Interface in the Presence of Ferrate(VI). *Sci. Rep.* **2020**, *10* (1), 8757. https://doi.org/10.1038/s41598-020-65674-x.
(110) C, O. H. S.; Dollase, W. A. *Crystal structures and cation distributions in simple spinels from powder XRD structural refinements: MgCr2O4, ZnCr2O4, Fe3O4 and the temperature dependence of the cation distribution in ZnAl2O4 Sample: Fe3O4, results from data collected at BGI (MoKalpha1) radiation)*. http://www.crystallography.net/cod/9006189.html (accessed 2024-02-22).
(111) Costas Bosque, D. Characterization of High-Entropy Alloys: Study of the Addition of Aluminum to the High Entropy System HfMoTaTi+Al. Bachelor thesis, Universitat Politècnica de Catalunya, 2018. https://upcommons.upc.edu/handle/2117/119662 (accessed 2023-02-21).
(112) Basavaraj, K.; Elangovan, K. Investigation the Stability of the Copper Oxide- Ethylene Glycol Nanofluids. **2023**, *10* (05).
(113) Rák, Zs.; Maria, J.-P.; Brenner, D. W. Evidence for Jahn-Teller Compression in the (Mg, Co, Ni, Cu, Zn)O Entropy-Stabilized Oxide: A DFT Study. *Mater. Lett.* **2018**, *217*, 300–303. https://doi.org/10.1016/j.matlet.2018.01.111.
(114) Rost, C. M.; Rak, Z.; Brenner, D. W.; Maria, J.-P. Local Structure of the MgxNixCoxCuxZnxO(X=0.2) Entropy-Stabilized Oxide: An EXAFS Study. *J. Am. Ceram. Soc.* **2017**, *100* (6), 2732–2738. https://doi.org/10.1111/jace.14756.
(115) Chen, K.; Kim, S.; Rajendiran, R.; Prabakar, K.; Li, G.; Shi, Z.; Jeong, C.; Kang, J.; Li, O. L. Enhancing ORR/OER Active Sites through Lattice Distortion of Fe-Enriched FeNi3 Intermetallic Nanoparticles Doped N-Doped Carbon for High-Performance Rechargeable Zn-Air Battery. *J. Colloid Interface Sci.* **2021**, *582*, 977–990. https://doi.org/10.1016/j.jcis.2020.08.101.
(116) Hosterman, B. D. Raman Spectroscopic Study of Solid Solution Spinel Oxides, University of Nevada, Las Vegas. https://doi.org/10.34917/2476131.
(117) Modi, K. B.; Raval, P. Y.; Shah, S. J.; Kathad, C. R.; Dulera, S. V.; Popat, M. V.; Zankat, K. B.; Saija, K. G.; Pathak, T. K.; Vasoya, N. H.; Lakhani, V. K.; Chandra, U.; Jha, P. K. Raman and Mossbauer Spectroscopy and X-Ray Diffractometry Studies on Quenched Copper–Ferri–Aluminates. *Inorg. Chem.* **2015**, *54* (4), 1543–1555. https://doi.org/10.1021/ic502497a.
(118) Zhang, L.; Shi, W.; Zhang, B. A Review of Electrocatalyst Characterization by Transmission Electron Microscopy. *J. Energy Chem.* **2017**, *26* (6), 1117–1135. https://doi.org/10.1016/j.jechem.2017.10.016.
(119) Haruna, A. B.; Barrett, D. H.; Rodella, C. B.; Erasmus, R. M.; Venter, A. M.; Sentsho, Z. N.; Ozoemena, K. I. Microwave Irradiation Suppresses the Jahn-Teller Distortion in Spinel LiMn2O4

Cathode Material for Lithium-Ion Batteries. *Electrochimica Acta* **2022**, *426*, 140786. https://doi.org/10.1016/j.electacta.2022.140786.
(120) Krivina, R. A.; Ou, Y.; Xu, Q.; Twight, L. P.; Stovall, T. N.; Boettcher, S. W. Oxygen Electrocatalysis on Mixed-Metal Oxides/Oxyhydroxides: From Fundamentals to Membrane Electrolyzer Technology. *Acc. Mater. Res.* **2021**, *2* (7), 548–558. https://doi.org/10.1021/accountsmr.1c00087.
(121) Wang, Z.; Wang, Y.; Zhang, N.; Ma, L.; Sun, J.; Yu, C.; Liu, S.; Jiang, R. Highly Efficient Oxygen Evolution Catalysis Achieved by NiFe Oxyhydroxide Clusters Anchored on Carbon Black. *J. Mater. Chem. A* **2022**, *10* (19), 10342–10349. https://doi.org/10.1039/D2TA01931K.
(122) Moraes, A.; Assumpção, M. H. M. T.; Simões, F. C.; Antonin, V. S.; Lanza, M. R. V.; Hammer, P.; Santos, M. C. Surface and Catalytical Effects on Treated Carbon Materials for Hydrogen Peroxide Electrogeneration. *Electrocatalysis* **2016**, *7* (1), 60–69. https://doi.org/10.1007/s12678-015-0279-5.
(123) Fu, L.; Chen, H.; Wang, K.; Wang, X. Oxygen-Vacancy Generation in MgFe2O4 by High Temperature Calcination and Its Improved Photocatalytic Activity for CO2 Reduction. *J. Alloys Compd.* **2022**, *891*, 161925. https://doi.org/10.1016/j.jallcom.2021.161925.
(124) *ACTIVATED CARBON MATERIALS FROM CALOTROPIS GIGANTEA P. Indra Neel, B. Viswanathan and T. K. Varadarajan 3 rd Annual Day Function, 1 st August 2009, National. - ppt download*. https://slideplayer.com/slide/9198999/ (accessed 2023-12-04).
(125) *Fig. 3.19 EPR spectra of commercial activated carbon materials (a) di...* ResearchGate. https://www.researchgate.net/figure/EPR-spectra-of-commercial-activated-carbon-materials-a-di-phenyl-picryl-hydrazyl_fig24_299354209 (accessed 2023-08-14).
(126) Usharani, N. J.; Bhandarkar, A.; Subramanian, S.; Bhattacharya, S. S. Antiferromagnetism in a Nanocrystalline High Entropy Oxide (Co,Cu,Mg,Ni,Zn)O : Magnetic Constituents and Surface Anisotropy Leading to Lattice Distortion. arXiv April 24, 2020. http://arxiv.org/abs/2004.11684 (accessed 2023-10-14).
(127) Berardan, D.; Meena, A. K.; Franger, S.; Herrero, C.; Dragoe, N. Controlled Jahn-Teller Distortion in (MgCoNiCuZn)O-Based High Entropy Oxides. *J. Alloys Compd.* **2017**, *704*, 693–700. https://doi.org/10.1016/j.jallcom.2017.02.070.
(128) Malhotra, R. K.; Seth, V. P.; Jain, V. K. Spin Quenching and EPR of Mn2+ in K2Ni(SeO4)2·6H2O Single Crystals. *Can. J. Phys.* **1983**, *61* (9), 1359–1361. https://doi.org/10.1139/p83-173.
(129) Anderson, P. W.; Weiss, P. R. Exchange Narrowing in Paramagnetic Resonance. *Rev. Mod. Phys.* **1953**, *25* (1), 269–276. https://doi.org/10.1103/RevModPhys.25.269.
(130) N. Spencer, J.; Folli, A.; Ren, H.; M. Murphy, D. An EPR Investigation of Defect Structure and Electron Transfer Mechanism in Mixed-Conductive LiBO 2 –V 2 O 5 Glasses. *J. Mater. Chem. A* **2021**, *9* (31), 16917–16927. https://doi.org/10.1039/D1TA02352G.
(131) Murawski, L.; Gledel, C.; Sanchez, C.; Livage, J.; Audières, J. P. Electrical Conductivity of V2O5 and LixV2O5 Amorphous Thin Films. *J. Non-Cryst. Solids* **1987**, *89* (1), 98–106. https://doi.org/10.1016/S0022-3093(87)80324-1.
(132) Meinert, M.; Reiss, G. Electronic Structure and Optical Band Gap Determination of NiFe2O4. *J. Phys. Condens. Matter Inst. Phys. J.* **2014**, *26* (11), 115503. https://doi.org/10.1088/0953-8984/26/11/115503.
(133) Stenzel, D.; Zhou, B.; Okafor, C.; Kante, M. V.; Lin, L.; Melinte, G.; Bergfeldt, T.; Botros, M.; Hahn, H.; Breitung, B.; Schweidler, S. High-Entropy Spinel-Structure Oxides as Oxygen Evolution Reaction Electrocatalyst. *Front. Energy Res.* **2022**, *10*.
(134) Chemelewski, K. R.; Lee, E.-S.; Li, W.; Manthiram, A. Factors Influencing the Electrochemical Properties of High-Voltage Spinel Cathodes: Relative Impact of Morphology and Cation Ordering. *Chem. Mater.* **2013**, *25* (14), 2890–2897. https://doi.org/10.1021/cm401496k.
(135) Slesinski, A.; Sroka, S.; Fic, K.; Frackowiak, E.; Menzel, J. Operando Monitoring of Local pH Value Changes at the Carbon Electrode Surface in Neutral Sulfate-Based Aqueous Electrochemical

Capacitors. *ACS Appl. Mater. Interfaces* **2022**, *14* (33), 37782–37792. https://doi.org/10.1021/acsami.2c09920.

(136) Bischoff, C. F.; Fitz, O. S.; Burns, J.; Bauer, M.; Gentischer, H.; Birke, K. P.; Henning, H.-M.; Biro, D. Revealing the Local pH Value Changes of Acidic Aqueous Zinc Ion Batteries with a Manganese Dioxide Electrode during Cycling. *J. Electrochem. Soc.* **2020**, *167* (2), 020545. https://doi.org/10.1149/1945-7111/ab6c57.

(137) McDonough, J. K.; Gogotsi, Y. Carbon Onions: Synthesis and Electrochemical Applications. *Interface Mag.* **2013**, *22* (3), 61–66. https://doi.org/10.1149/2.F05133if.

(138) *Comparison of the Oxygen Reduction Reaction between NaOH and KOH Solutions on a Pt Electrode: The Electrolyte-Dependent Effect | The Journal of Physical Chemistry B*. https://pubs.acs.org/doi/10.1021/jp102367u (accessed 2023-05-13).

(139) Shinagawa, T.; Garcia-Esparza, A. T.; Takanabe, K. Insight on Tafel Slopes from a Microkinetic Analysis of Aqueous Electrocatalysis for Energy Conversion. *Sci. Rep.* **2015**, *5* (1), 13801. https://doi.org/10.1038/srep13801.

(140) Xu, L.; Wu, S.; He, X.; Wang, H.; Deng, D.; Wu, J.; Li, H. Interface Engineering of Anti-Perovskite Ni3FeN/VN Heterostructure for High-Performance Rechargeable Zinc–Air Batteries. *Chem. Eng. J.* **2022**, *437*, 135291. https://doi.org/10.1016/j.cej.2022.135291.

Appendix

A1 Rietveld Refinement parameters

R-Values					
Rexp :	4.17	Rwp :	15.14	Rp : 10.31 GOF :	3.63
Rexp`:	6.32	Rwp`:	22.94	Rp` : 20.11 DW :	0.02
Quantitative Analysis – Rietveld					
Phase 1 : HEMOx 96.958 %					
Phase 2 : Tenorite 3.042 %					
Background					
Chebychev polynomial					
Coefficient 0	365.4314				
Coefficient 1	336.5042				
Coefficient 2	214.0753				
Coefficient 3	110.5699				
Coefficient 4	35.327				
Coefficient 5	12.55036				
Instrument					
Primary radius (mm	1000				
Secondary radius (mm	1128.44				
Capillary diameter (mm	1				
Capillary sample LAC (1/cm	3				
Linear PSD 2Th angular range (°	4				
FDS angle (°	1				
Finger et al s (mm	0.569218				
Finger et al h (mm	0.331847				
Corrections					
Zero error 0.02156635					
LP Factor 0					
Absorption (1/cm) 492.1817					
Sample Thickness (mm) 1					

Miscellaneous	
X Calculation Step 0.02	
Start X 6	
Structure 1	
Phase name HEMOx	
R-Bragg 14.728	
Spacegroup P1	
Scale 1.76918e-004	
Cell Mass 746.705	

Cell Volume (Å^3) 573.64858

Wt% - Rietveld 96.958

Double-Voigt|Approach

Crystal Linear Absorption Coeff. (1/cm) 64.673

Crystal Density (g/cm^3) 2.161

Preferred Orientation Spherical Harmonics

Order 4

Lattice parameters

a	(Å)	8.314362
b	(Å)	8.290544
c	(Å)	8.322233
alpha	(°)	89.7842
beta	(°)	90.05816
gamma	(°)	89.80078

Site	Np	X	y	z	Atom	Occ	Beq
Fe0	1	0.50887	-0.00942	0.53053	Fe	0.25	0.2955
Fe1	1	0.76384	0.75974	0.25329	Mn	0.25	-0.3666
Fe2	1	0.51745	0.49889	0.03	Fe	0.25	0.4969
Fe3	1	0.76657	0.27021	0.74325	Co	0.25	-0.01432
Fe4	1	0.01759	-0.0053	0.00746	Fe	0.25	0.003575
Fe5	1	0.28496	0.77096	0.73441	Co	0.25	-0.4322
Fe6	1	0.01558	0.49218	0.5199	Fe	0.25	0.4299
Fe7	1	0.26904	0.26105	0.24683	Ni	0.25	-0.04715
Fe8	1	0.89112	0.91113	0.5999	Ni	0.25	0.3932
Fe9	1	0.15518	0.66221	0.14879	Cu	0.25	-0.4952
Fe10	1	0.15517	0.93026	0.39121	Co	0.25	-0.1028
Fe11	1	0.38424	0.64988	0.38379	Ni	0.25	0.7944
Fe12	1	0.89204	0.4016	0.11763	Ni	0.25	0.5173
Fe13	1	0.15694	0.15467	0.64781	Mn	0.25	0.3634
Fe14	1	0.12523	0.41528	0.87173	Co	0.25	-0.6877
Fe15	1	0.37304	0.1376	0.8882	Cu	0.25	-0.147
Fe16	1	0.37816	0.90292	0.1019	Cu	0.25	0.821
Fe17	1	0.65239	0.66266	0.65024	Mn	0.25	0.3063
Fe18	1	0.64609	0.92128	0.88256	Mn	0.25	-0.9307
Fe19	1	0.88977	0.66799	0.8965	Cu	0.25	-0.7557
Fe20	1	0.38804	0.40248	0.60916	Ni	0.25	0.5974
Fe21	1	0.65287	0.14644	0.16156	Mn	0.25	-0.2159
Fe22	1	0.63692	0.40658	0.39904	Mn	0.25	-0.5635
Fe23	1	0.88226	0.14761	0.40037	Cu	0.25	-0.3272
O24	1	0.10486	0.88665	0.13514	O	1	-0.7295
O25	1	0.11293	0.02171	0.41965	O	0.9507	1.307
O26	1	0.7846	0.78334	0.23049	O	0.8948	4.872
O27	1	0.16057	0.65087	0.35888	O	1	1.265
O28	1	0.84806	0.08812	0.68261	O	0.8858	1.412
O29	1	0.40959	0.91707	0.41359	O	0.8435	-1.838
O30	1	0.03422	0.82641	0.51795	O	0.6627	2.239
O31	1	0.35226	0.55424	0.096	O	0.4558	-2.497

O32	1	0.10628	0.30656	0.66308	O	0.7714	4.14
O33	1	0.00275	0.46916	0.91013	O	0.8478	0.2507
O34	1	0.76029	0.50757	0.4684	O	0.867	19.8
O35	1	0.13104	0.14741	0.81549	O	0.886	0.8195
O36	1	0.88188	0.64782	0.17001	O	0.7175	0.4718
O37	1	0.39078	0.37896	0.91211	O	0.7815	-3.103
O38	1	0.08799	0.35751	0.00664	O	0.7144	1.967
O39	1	0.38558	0.13833	0.60159	O	0.6649	-1.016
O40	1	0.63138	0.87995	0.63213	O	0.6087	-0.1392
O41	1	0.60944	0.01678	0.93481	O	0.9407	2.159
O42	1	0.26008	0.79236	0.80476	O	0.4702	-4.263
O43	1	0.68795	0.67943	0.86569	O	1	0.03189
O44	1	0.37611	0.14162	0.18169	O	0.8112	-0.258
O45	1	0.92613	0.9269	0.90634	O	0.4891	-3.058
O46	1	0.51677	0.78122	0.04544	O	0.9478	-0.6582
O47	1	0.92712	0.5767	0.65386	O	0.7467	1.135
O48	1	0.63397	0.35006	0.15157	O	0.6224	-2.074
O49	1	0.62171	0.50583	0.49322	O	0.8397	1.582
O50	1	0.31727	0.29768	0.21346	O	0.9897	8.466
O51	1	0.67469	0.14916	0.35649	O	1	-0.02695
O52	1	0.34775	0.57424	0.69232	O	0.7576	-0.6275
O53	1	0.88392	0.33931	0.4056	O	0.1506	-9.994
O54	1	0.51487	0.27734	0.56503	O	0.868	-0.6444
O55	1	0.88847	0.08918	0.15375	O	0.6096	-0.9654

Structure 2
Phase name Tenorite
R-Bragg 7.832
Spacegroup C2/c
Scale 8.92468e-005
Cell Mass 328.048
Cell Volume (Å^3) 81.20568
Wt% - Rietveld 3.042
Crystal Linear Absorption Coeff. (1/cm) 378.051
Crystal Density (g/cm^3) 6.708
Preferred Orientation Spherical Harmonics
Order 4

A2 Simulated Crystal planes and D-spacings for HESO

h	k	l	d(Å)	2θ	I
-1	1	1	4.925675	9.31591	32.30531
1	-1	-1	4.925675	9.31591	31.98705
-1	-1	-1	4.803182	9.55404	30.27559

1	1	1	4.803182	9.55404	29.97386
-2	2	0	3.066832	14.98862	47.21741
2	-2	0	3.066832	14.98862	47.21741
-2	0	-2	3.004827	15.29975	44.43647
2	0	2	3.004827	15.29975	44.43647
0	2	-2	3.003621	15.30592	35.37957
0	-2	2	3.003621	15.30592	35.37957
0	-2	-2	2.978297	15.43686	56.71674
0	2	2	2.978297	15.43686	56.71674
2	0	-2	2.961952	15.52257	45.8819
-2	0	2	2.961952	15.52257	45.8819
-2	-2	0	2.910286	15.79988	43.49674
2	2	0	2.910286	15.79988	43.49674
1	-3	1	2.598142	17.71253	99.46758
-1	3	-1	2.598142	17.71253	99.16863
3	-1	1	2.590941	17.76215	87.05879
-3	1	-1	2.590941	17.76215	86.76414
-1	3	1	2.578829	17.84625	85.96191
1	-3	-1	2.578829	17.84625	85.67067
1	-1	3	2.57667	17.86133	97.72303
-1	1	-3	2.57667	17.86133	97.42996
-3	1	1	2.566122	17.93535	96.21468
3	-1	-1	2.566122	17.93535	95.92483
-1	1	3	2.544424	18.08958	79.73553
1	-1	-3	2.544424	18.08958	79.45531
-1	-1	-3	2.540199	18.11992	82.51078
1	1	3	2.540199	18.11992	82.23033
1	1	-3	2.532023	18.17892	92.81078
-1	-1	3	2.532023	18.17892	92.53047
1	3	-1	2.517707	18.28318	91.81812
-1	-3	1	2.517707	18.28318	91.54153
-3	-1	-1	2.513802	18.31182	91.43367
3	1	1	2.513802	18.31182	91.15816
-1	-3	-1	2.512835	18.31893	77.05974
1	3	1	2.512835	18.31893	76.78816
-2	2	-2	2.502015	18.39883	29.31433
2	-2	2	2.502015	18.39883	29.21199
3	1	-1	2.498464	18.42521	75.85802
-3	-1	1	2.498464	18.42521	75.59033
2	-2	-2	2.462838	18.69412	28.33841
-2	2	2	2.462838	18.69412	28.23917
2	2	2	2.401591	19.1753	26.84302
-2	-2	-2	2.401591	19.1753	26.74854
-2	-2	2	2.392387	19.24978	26.62145
2	2	-2	2.392387	19.24978	26.52767
0	-4	0	2.116529	21.78754	77.53924
0	4	0	2.116529	21.78754	77.53924
0	0	4	2.113217	21.82211	77.14741

0	0	-4	2.113217	21.82211	77.14741
-4	0	0	2.105627	21.90173	76.25368
4	0	0	2.105627	21.90173	76.25368
-1	5	-1	1.64854	28.0847	26.05963
1	-5	1	1.64854	28.0847	25.95963
-5	1	-1	1.642286	28.19386	25.73068
5	-1	1	1.642286	28.19386	25.63176
-3	3	3	1.641892	28.20076	21.96637
3	-3	-3	1.641892	28.20076	21.89011
1	-5	-1	1.641476	28.20805	30.37336
-1	5	1	1.641476	28.20805	30.27369
-1	1	-5	1.636775	28.29075	25.44277
1	-1	5	1.636775	28.29075	25.34482
5	-1	-1	1.632387	28.36839	29.81763
-5	1	1	1.632387	28.36839	29.71955
1	1	5	1.625271	28.49521	29.28891
-1	-1	-5	1.625271	28.49521	29.19206
1	-1	-5	1.622914	28.53747	29.24443
-1	1	5	1.622914	28.53747	29.148
-1	-1	5	1.621697	28.55935	25.5601
1	1	-5	1.621697	28.55935	25.46453
-1	-5	1	1.6149	28.68212	25.20058
1	5	-1	1.6149	28.68212	25.10618
1	5	1	1.611627	28.74162	28.47549
-1	-5	-1	1.611627	28.74162	28.38098
5	1	1	1.609716	28.77648	28.36255
-5	-1	-1	1.609716	28.77648	28.26837
-5	-1	1	1.602334	28.91192	24.54349
5	1	-1	1.602334	28.91192	24.45121
-3	-3	-3	1.601061	28.93542	20.18891
3	3	3	1.601061	28.93542	20.11788
4	-4	0	1.533416	30.24166	100
-4	4	0	1.533416	30.24166	100
-4	0	-4	1.502414	30.88109	92.91096
4	0	4	1.502414	30.88109	92.91096
0	-4	4	1.501811	30.89379	92.77616
0	4	-4	1.501811	30.89379	92.77616
0	-4	-4	1.489149	31.16312	89.97199
0	4	4	1.489149	31.16312	89.97199
-4	0	4	1.480976	31.3395	88.18931
4	0	-4	1.480976	31.3395	88.18931
-4	-4	0	1.455143	31.91057	82.69444
4	4	0	1.455143	31.91057	82.69444

A3 Table of A_{1g} Raman signals in partially inverted spinels

HESO	A_{1g} normal /cm^{-1}	A_{1g} inverse /cm^{-1}	Ref
$(CuCoFeMnNi)_3O_4$	**626**	**698**	*This work*
$(CuCoFeMnNi)_3O_4$/C	**618**	**683**	*This work*
$(CrMnFeCoNi)_3O_4$	**616**	**680**	*36*
$(CrMnFeCoZn)_3O_4$	**629**	**701**	*36*
$(CrMnFeNiZn)_3O_4$	**658***	**-**	*36*

**Inversion of 40% resulted in imperfect resolution of the two peaks*